THE UNIVERSITY OF CHICAGO

SILICON NANOWIRES FOR THE OPTICAL MODULATION OF CELLULAR ACTIVITY

A DISSERTATION SUBMITTED TO

THE FACULTY OF THE DIVISION OF THE BIOLOGICAL SCIENCES

AND THE PRITZKER SCHOOL OF MEDICINE

IN CANDIDACY FOR THE DEGREE OF

DOCTOR OF PHILOSOPHY

INTERDISCIPLINARY SCIENTIST TRAINING PROGRAM: BIOPHYSICAL SCIENCES

BY

RAMYA PARAMESWARAN

CHICAGO, ILLINOIS

AUGUST 2018

Table of Contents

List of Figures

List of Tables

Acknowledgments

Welcome to the most important part of my thesis. The PhD has been a transformative experience for me, both personally and scientifically, and would not have happened without the unconditional support from many people in my life. I want to first thank both of my advisors, Bozhi Tian and Erin Adams, for their mentorship and support. I have been in the Tian lab since its inception and it has been a pleasure to watch the lab grow both scientifically and culturally. I am aware that the first batches of graduate students can create the scientific and cultural foundations for the lab and I am so grateful to Bozhi for taking a leap of faith and letting me into his lab. I also want to thank him for giving me the space and independence to produce and execute my own scientific thoughts and ideas while simultaneously providing incredible mentorship and guidance. This freedom was integral to my growth as a scientist. While I was housed in the Tian lab for most of my PhD, I met with Erin on a weekly basis. She so patiently and brilliantly advised me through years of me presenting electrophysiology data in neurons, a far cry from the bread and butter of her own lab. I think we were both so excited when we finally made some progress on the T cell side of the project in the last year! She has been an incredible mentor and will always be an inspiration to me as a woman in science. She not only advised me scientifically, but also personally on how to overcome some of the challenges of being a minority in the sciences. I am also so grateful for her ability to always remind me of the forest when I would get lost in the trees. I am particularly grateful to both of my advisors for so passionately embarking on this interdisciplinary scientific journey with me. Their openness to wild and risky ideas,

excitement about collaborating with others, and positivity helped me to persevere especially when experiments were not working well.

I would also like to thank my labmates in both the Tian and Adams labs, past and present, for the emotional and scientific support throughout the years. I would specifically like to thank the following people for their scientific contributions to my projects: Michael Burke, Andrew Philips, Dr. John Zimmerman, Kelliann Koehler, Dr. Yuanwen Jiang, Dr. Menahem Rotenberg, Dr. Barbara Hissa, Dr. Jaeseok Yi, Junyoung Jeong, Kiela Moreno, Anthony Bartley, Lillian Nemeth, and Dr. Sobhan Roy. I would like to also give a special thanks to my mentees, Michael Burke, Junyoung Jeong, Kiela Moreno, Anthony Bartley, and Lillian Nemeth, who taught me and contributed so much scientifically. I would not have made it through the PhD without your hard work, patience, and dedication and I have learned so much about mentorship from you all. I would also like to thank the UChicago MRSEC facility, Dr. Christine Labno and the Digital Light Microscopy Facility, Dr. Fengyuan Shi at UIC, Dr. Dieter Ishiem at Northwestern, the Center for Nanoscale Materials at Argonne, the Flow Cytometry Facility at Uchicago, and the Searle Cleanroom.

I would also like to give a special thank you to my thesis committee members, Dr. Franscisco Bezanilla and Dr. Marisa Alegre, for all of their advice and support throughout these past five years. Pancho was a integral part of my PhD experience acting as a third mentor to me. Without his guidance and generosity, many of the electrophysiology components of my projects would have not happened. I want to also specifically thank Dr. Joao Souza from his lab for teaching me how to patch clamp and letting me use his electrophysiology setup throughout my PhD. Marisa played an

incredibly important role on my thesis committee as the resident immunology expert. Her vast knowledge of the literature and insightful thoughts and comments even when we were discussing other cellular systems was critical for my scientific progress.

I am also extremely grateful for the programmatic support I have had from both the MSTP and the Biophysical Sciences program. In the MSTP, the hard work of Dr. Marcus Clark, Dr. Elise Covic, Dr. Alison Anastasio, Dr. Kristin McCann, Shay McAllister, Sarah Laloggia, and Shanetha Thomas has made my PhD experience run as smoothly as possible and I am so thankful. I also want to thank Dr. Michele Wittels, Dr. Julie Feder, Dr. Greg Engel, Dr. Tobin Sosnick, and Dr. Adam Hammond in the Biophysical Sciences program for their support and care. I especially want to thank Michele, who was an integral member of my support system throughout this process.

Lastly, but certainly not least, I would like to thank my friends and family, without whom this journey would not have been possible. I don't think I can really capture in words how important you all are to me, but thank you for all of the runs to Krispy Kreme and Dat Donut at 6 am, late night cooking adventures, trio jam sessions, sub basement lost book club readings, dance parties, and love. To my parents, I really would not be here without your love and support in every sense of the word. I am so grateful to be able to share this with you – this is yours as much as it is mine. I would like to dedicate this thesis to my grandmother, my biggest inspiration and fan, who passed away during my PhD.

Preface

When I started the collaboration between the Tian and Adams lab, my primary goals were to understand the role of membrane voltage in T cell receptor (TCR) signaling and T cell triggering events. I wanted to use the silicon nanowire technology in the Tian lab to uncover fundamental knowledge about T cells in the Adams lab. I also wanted to develop a tool that could allow us to bridge electrical signaling in populations of cells with biochemical signaling pathways and understand how the two types of signaling pathways interact, especially in the context of non-excitable cells. Prior to joining the labs, Bozhi had built a chemical vapor deposition system in the lab that allowed us to synthesize silicon nanowires using a vapor liquid solid growth process. Previous work by Bozhi during his graduate school and postdoctoral phases focused on fabricating silicon nanowire based field effect transistors for detecting electrical signals in cells. After starting his own lab, he had this incredible idea that we could one day possibly use light to generate currents from these nanowires to change the membrane voltage of a target cell, sort of like a non-genetic version of optogenetics, in a minimally invasive manner. I was fascinated by this idea and its potential for both fundamental bioelectric studies and therapeutics down the road. Erin's lab was focused on understanding how unconventional T cell receptors (TCRs) like gamma delta TCRs could recognize their ligands. I was excited by her unique and biochemical/biophysical approach to studying the immune system and thought that combining Bozhi's expertise in making silicon nanowires with her expertise in understanding how T cells function through their TCRs would be fascinating. I am excited by what we have been able to achieve in the past five years: 1) modify and further characterize a coaxial silicon

nanowire tool for biological modulation studies 2) develop a method for measuring photocurrents from single nanowires 3) optically modulate single neuron excitability with coaxial silicon nanowires 4) develop and characterize a new polymer-silicon nanowire hybrid material 5) optically train cardiomyocytes to beat at a target frequency 6) target coaxial silicon nanowires to specific cell types via surface functionalization 7) optically modulate TCR signaling in populations of T cells.

Abstract

One of the fundamental goals guiding research in the biological sciences is to understand how cellular systems process complex physical and environmental cues and communicate with each other across multiple length scales. Importantly, aberrant signal processing in these systems can lead to diseases that can have devastating impacts on human lives. Biophysical studies in the past several decades have demonstrated that cells can respond to not only biochemical cues, but also to mechanical and electrical ones. Thus, the development of new materials that can both sense and modulate all of these pathways is necessary. Semiconducting nanowires are an emerging class of discovery platforms and tools that can push the limits of our ability to modulate and sense biological behaviors for both fundamental research and clinical applications. These materials are of particular interest for interfacing with cellular systems due to their matched dimension with subcellular components (*e.g.*, cytoskeletal filaments), and easily tunable properties in the electrical, optical and mechanical regimes. Rational design via traditional or new approaches, *e.g.*, nano-casting and mesoscale chemical lithography, can allow us to control micron- and nano-scale features in nanowires to achieve new biointerfaces. Both processes endogenous to the target cell and properties of the material surface dictate the character of these interfaces.

In this thesis, I describe my work on the (1) synthesis and characterization of a silicon nanowire material and (2) use of that material in different configurations for the optical modulation of three cellular systems. In the first section, I discuss the synthesis of coaxial p-type/i-type/n-type silicon nanowires (PIN-SiNWs) with enhanced surface

atomic Au, which allows for the efficient production of photoelectrochemical currents upon 532 nm laser illumination. Here, I also describe the adaptation of patch clamp electrophysiology for the measurement of photocurrents from single nanowires in an interconnect-free configuration. In the second section, I first use single free-standing PIN-SiNWs to optically modulate the excitability of single primary dorsal root ganglion neurons. I demonstrate that this neuromodulation is occurring an atomic Au mediated photoelectrochemical process, rather than a photothermal one. Next, I incorporate PIN-SiNWs into a SU-8 polymeric grid structure fabricated via photolithography and use this mesh structure (SU-8-PIN mesh) to optically train neonatal rat ventricular cardiomyocytes as well as adult rat hearts *ex vivo* to beat at a target frequency. In these experiments, the cardiomyocytes are cultured atop the mesh or the mesh is stuck onto the adult hearts in the absence of a suture or adhesive via capillary forces. A moving laser stimulus is used to train the cardiomyocytes in both cases in order to mimic physiological stimuli that interact with cells not just at a single point but spatially all over the cell. In the last case, I label PIN-SiNWs with antibodies that can bind to surface receptors expressed on T cells. I treat primary mouse T cells with these labeled nanowires and generate free-standing T cell-PIN-SiNW complexes and show that the labeled nanowires are highly specific to T cells in a mixed cell population. I develop a method for the optical stimulation of populations of these T cells while they are being activated through their T cell receptors. I show that depolarizing populations of T cells optically via a PIN-SiNW mediated process during T cell activation dampens TCR signaling, as demonstrated via intracellular phospho-flow cytometry.

In this thesis, I demonstrate non-invasive, non-genetic optical modulation of various cellular systems using PIN-SiNWs in a free-standing configuration that can be dispersed in a drug-like fashion, or in a substrate configuration as a high density mesh, or lastly as a free-standing complex with the target cell. This work in neurons and cardiomyocytes has implications for photo-responsive therapeutics in the context of diseases in excitable cell types that are characterized by aberrant electrical activity. The work in T cells, while also having potential for use in autoimmune therapeutics, also helps us to understand a more fundamental question of how membrane voltage affects T cell activation. Moreover, this work is an example of a novel technique that can be used to bridge electrical cellular signaling with other signaling pathways in populations of non-excitable cells.

Chapter 1. Introduction

Semiconductor nanostructures[1] are promising materials for use in both understanding fundamental biological processes and developing novel clinical therapeutics due to their tunable length scales and physical properties. Additionally, nanowire structures are able to operate either in interconnected configurations or as freestanding objects, forming multiple functional biointerfaces.[1-10] With appropriate compositions and structures, they can be both biocompatible and biodegradable.[3,8,11,12] For instance, one can readily control the doping profiles and morphologies in silicon (Si) nanowires via a vapor-liquid-solid (VLS) growth process, and specifically by modulating synthesis parameters such as pressure and temperature.[6,13-20] These synthetic controls can effectively encode micron- and nano-scale features, yielding a large toolbox of Si-based biomaterials.[21,22] Other semiconductor-based nanostructured materials or devices can also serve as both sensors and modulators of cellular behavior, including as probes for detecting cellular fluid dynamics[23] and intracellular pressure,[24] transducers for biofuel production,[25,26] and as delivery vehicles for nucleic acids.[27,28]

1.1 Approaches for the rational design of semiconductor nanostructures

1.1.1 Approaches for synthetic control of micron- or sub-micron scale features and functions

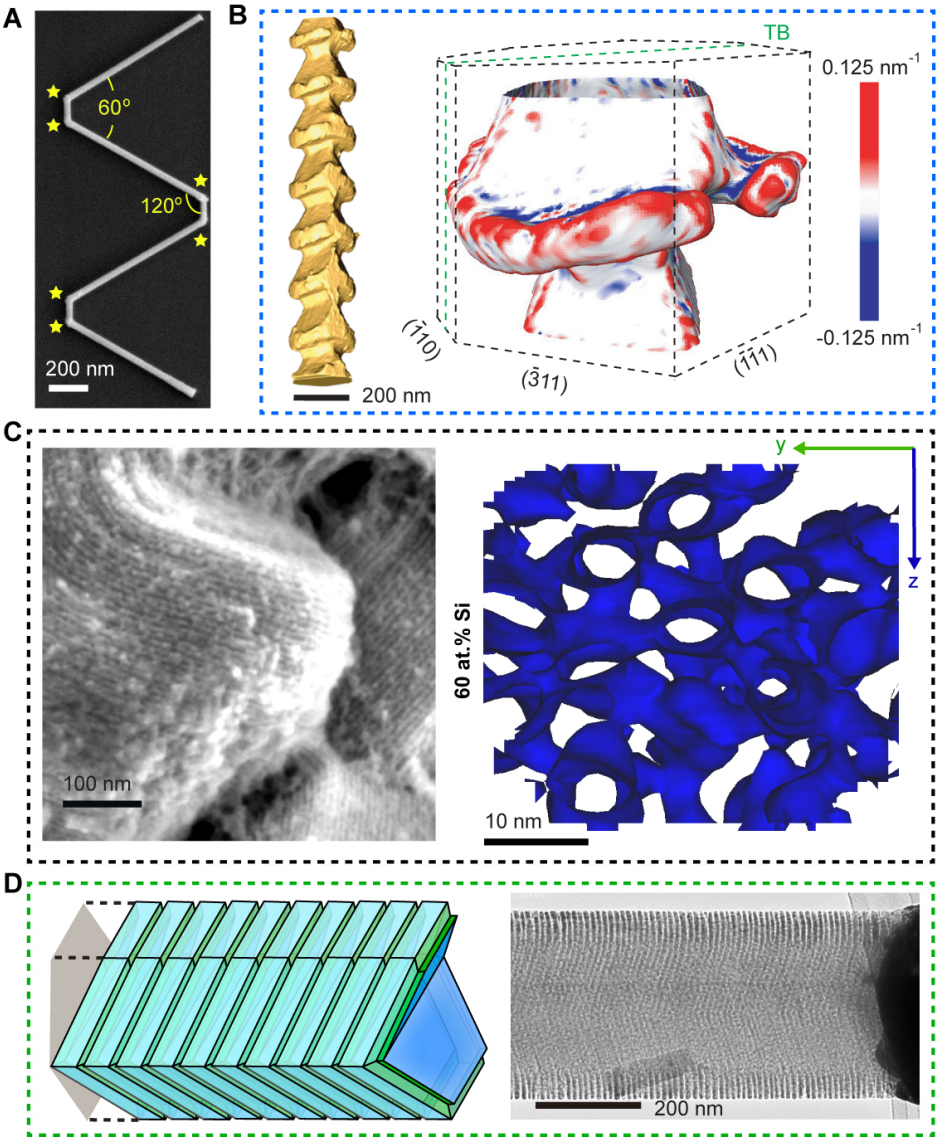

Figure 1.1. Structural designs of Si nanostructures can be explored for sub-cellular biointerfaces. (**A**) SEM image of a multiply-kinked SiNW, showing six kinks (yellow stars) with individual angles of 120°. (**B**) STEM tomography of a Si spicule, showing anisotropic features (left). A 3-D curvature map of one segment (right) shows convex and concave features in spicule. 'TB' denotes twin plane. (**C**) SEM (left) and 3D atom probe tomography iso-surface (right) images of mesoporous Si particles, revealing periodic arrangements of Si nanowire assembly (left) and 3D structures interconnected by micro-bridges (right). The iso-surface is plotted at 60 wt. % Si (**D**) A schematic

(Figure 1.1. continued) diagram (left) and a TEM image (right) of a SiNW with massively parallel sidewall grooves. Adapted with permission from ref (56). 2018 American Chemical Society.

VLS growth of nanowires is an example of the type of precise control that can be achieved during nanomaterial synthesis. One study by Tian *et al.* demonstrated this concept by using pressure modulations in a chemical vapor deposition (CVD) system to synthesize 2D multiply kinked Si nanowires (SiNWs) (Fig. 1.1A).[6,14] Kinks confined to a single plane are introduced at defined positions along SiNWs during the growth process via an abrupt modulation in growth pressure, yielding a nanostructure consisting of 2 straight single-crystalline segments oriented 60° apart,[6,14] as shown in Fig. 1.1A. This approach is unique in its ability to control the stereochemistry of adjacent kinks, paving the way for the synthesis of complex SiNW structures. This kinked morphology permits intracellular entry for electrical recordings of action potentials in excitable cells (*vide infra*).[6,29]

Another example of enabling angular features in nanowires uses the concept of metal diffusion along semiconductor surfaces that even in trace amounts can change the chemical etching behaviors of semiconductors.[13] It has been demonstrated that during VLS growth of SiNWs, the gold (Au) catalyst can diffuse down the sidewalls of SiNWs[30] under low silane partial pressure conditions. Luo *et al.* exploited this phenomenon by inducing periodic pressure modulations during SiNW growth to generate facet-selective, and potassium hydroxide (KOH)-resistant bands of atomic Au on the surfaces of the SiNWs (Fig. 1.1B).[13] Both Au deposition and diffusion processes over Si nanowires were found to be facet dependent, and thus Luo *et al.* were able to produce 3D graded Au/Si interfaces. KOH etching was then used to remove Si in

regions unprotected by the atomic Au, creating Si spicules with skeleton-like morphologies, 3D tectonic motifs, and reduced symmetries (Fig. 1.1B). These 3D nanowire sidewall features, similar to that of kinked nanowires, could potentially enhance bio-integration subcellularly.

1.1.2 Approaches for synthetic control of nanoscale features

In addition to controlling micron- and sub-micron-scale features in single nanowires, synthetic control of secondary nanoscale features (the primary feature being the 1D nanowire geometry) is possible, allowing for fabrication of materials with unconventional geometries and unique structural properties. Jiang *et al.* employed a nano-casting approach to synthesize 3D nanoporous Si particles (Fig. 1.1C).[8] In this work, silane was decomposed using a CVD system inside the pores of an ordered mesporous silica[31] (SBA-15) template, consisting of hexagonally-arranged channels. Wet chemical etching of the SBA-15 was used to generate uni-directionally-aligned SiNW arrays interconnected by micro-bridges, as shown in Fig. 1.1C. This material represents an example of a heterogeneous Si material with an amorphous atomic structure and ordered nanoscale framework. Approaches like this push the limits of conventional fabrication methods and allow for rational design of materials with novel capabilities.

Most recently, Fang *et al.* demonstrated that liquid Au-Si alloys established in classical VLS growth can deposit ordered 3D rings of isolated Au atoms over n-type phosphine-doped SiNW sidewalls.[32] This ordered deposition results from dynamic spontaneous instability of the liquid alloy droplets, where droplet sidewall oscillations promote atomic Au deposition. They performed *ab initio* molecular dynamics simulations and unveiled, surprisingly, single atomic Au-catalyzed chemical etching of Si in a

HF/H_2O_2 mixture. They subsequently verified this catalytic process in SiNWs and produced massive, ordered 3D grooves with spacings down to ~ 5 nm (Fig. 1.1D). These nanoscale features can allow for unique optical and mechanical interfaces with cellular structures, in addition to serving as delivery or storage matrices. Additionally, these ordered nanostructures may provide uniform and controllable geometrical cues for transport and biophysical dynamics of subcellular components; however, this direction still requires many in-depth investigations.

Another important demonstration of rational material design with nanoscale features and functions was the realization of coaxial *p-i-n* SiNWs for photovoltaic applications.[15,33] Here, introduction of dopant gases into VLS growth is used to create a nanoscale diode heterojunction in single SiNWs. *p-i-n* SiNWs, consisting of a *p*-type Si core with intrinsic and *n*-type Si shells, allow for charge separation to occur radially, yielding high efficiency carrier transport to the hetero-junction, reducing bulk recombination.[15,33]

1.2 Achieving robust bio-interfaces

1.2.1 Intracellular bio-interfaces

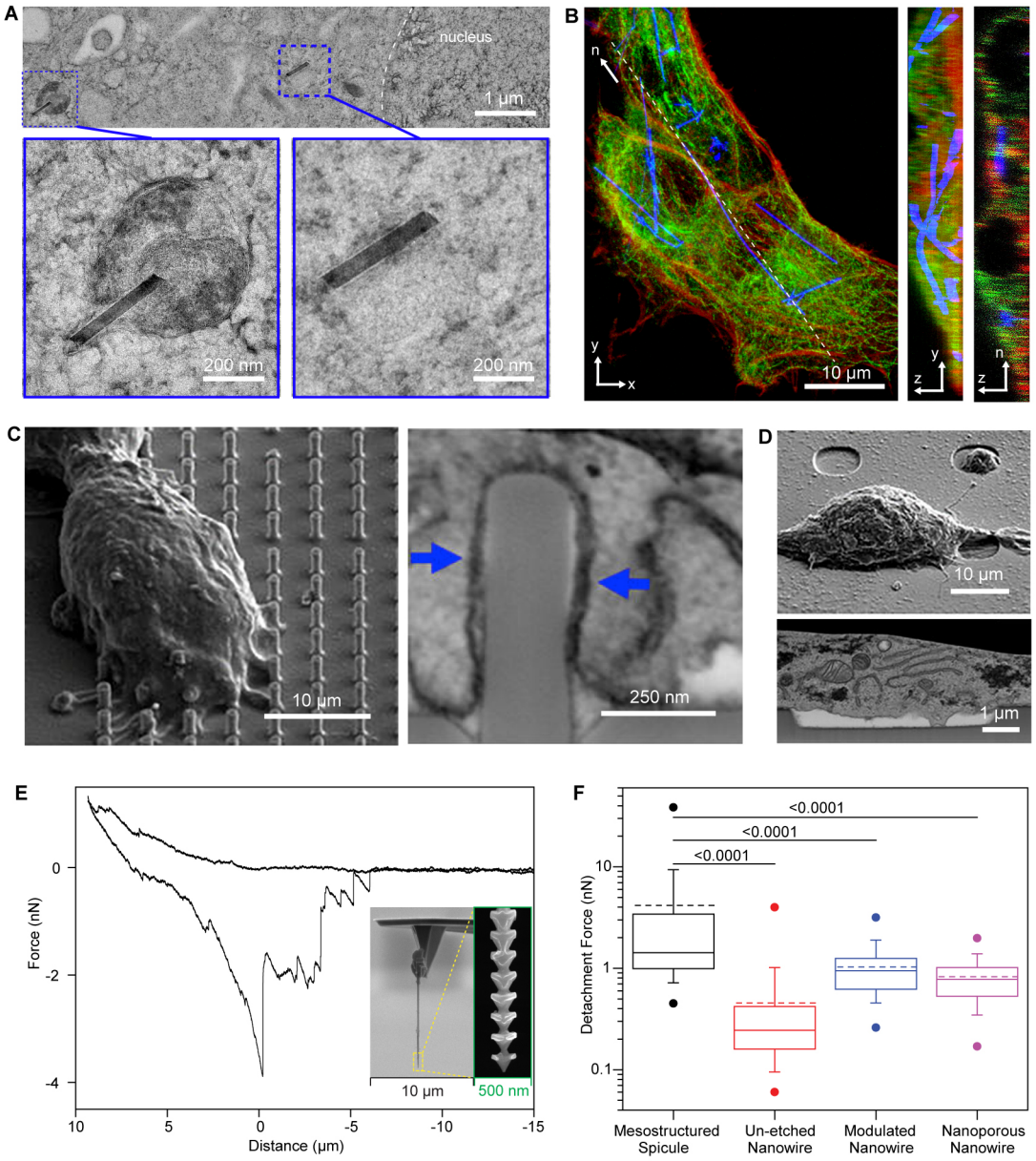

Figure 1.2. Nanostructured Si can enable tight biointerfaces at different cellular environments. (**A-B**) SiNWs can be internalized by mammalian cells. (**A**) TEM image of HUVEC thin section (~250 nm thick), with higher magnification insets, illustrating the distribution of internalized wires, both in vesicles and the cytosol (scale bar 1 μm, inset scale bar 200 nm). (**B**) Confocal fluorescence micrograph of HUVECs (red-actin, green-

(Figure 1.2 continued) tubulin) demonstrating SiNW internalization (blue-scattering). Maximum projection in the x-y plane (left, scale bar 10 μm), interpolated projection in the y-z plane (middle, height 3.5 μm), and thin confocal section taken along dashed line segment n (right, height 3.5 μm, length 48.3 μm). (**C-D**) Surface topography affects cleft distance between cell membrane and material surface. SEM of plasticized HEK cells on nanopillar arrays (**C**) and nanopore arrays (**D**). (**E-F**) Si spicules can enhance bio-integration at tissue level. (**E**) Representative force-distance (*F-D*) curve collected by inserting and retracting an individual Si spicule mounted onto an AFM tip into and from a collagen matrix. Insets display the spicule-based AFM probe at different magnifications. (**F**) Box-and-whisker plots of forces required to detach Si spicules (black), un-etched SiNWs (red), diameter-modulated SiNWs containing alternating segments of larger and smaller diameters axially down the wires as a result of alkaline etching (blue), and nanoporous SiNWs with pores 8.5 +/- 4.4 nm in size resulting from Ag-assisted chemical etching (purple). Half of the data points are within the box and 80% are within the whiskers. Solid and dashed lines mark median and mean, respectively. Dots represent maximum and minimum values. The means of detachment force are: 4.16 nN (mesostructured spicule), 0.455 nN (un-etched nanowire), 1.03 nN (modulated nanowire), and 0.827 nN (nanoporous nanowire). N=50, and numbers above bars indicate the P-value of the Mann-Whitney test. Adapted with permission from ref (56). 2018 American Chemical Society.

One method of achieving robust bio-interfaces is making use of natural cellular processes, such as phagocytosis.[3] Certain cell types, including macrophages and endothelial cells, are tasked with internalizing foreign materials and are thus able to uptake nanoscale materials such as SiNWs. Zimmerman et al. harnessed the phagocytic capabilities of human umbilical vein endothelial cells (HUVECs) to form robust interfaces between unlabeled SiNWs of varying diameters and HUVEC cells, as shown in Figs. 1.2A-B. Subsequently, an active transport process allows for transport of nanowires to the perinuclear region inside the cell, where they cluster and are later packaged into lysosomes (Fig. 1.2A).[3] This work has paved the way for the future usage of unlabeled high-aspect-ratio semiconductors for intracellular modulation of cellular behavior.

Due to the inability of some cell types to phagocytose foreign materials, work has been done to still allow for the creation of intracellular biointerfaces for those cell types. Wong Shi Kam *et al.* demonstrated that single-wall-carbon-nanotubes (SWNTs) functionalized with folate moieties could be selectively internalized into cancer cells expressing folate receptor tumor markers, allowing for targeted killing of cancer cells.[36] Another study by Lee *et al.* demonstrated that SiNWs surface-functionalized with trans-activating transcriptional activator cell-penetrating peptides can be internalized into both primary hippocampal and dorsal root ganglion neurons.[37] This study importantly demonstrates the ability of even non-phagocytic cells to form robust intracellular bio-interfaces with nanoscale materials.

One challenge specific to intracellular bio-interfaces, especially in complex tissue environments, is the ability to visualize individual nanostructures well. Adolfsson *et al.* provided a solution by using fluorescently barcoded GaP-GaInP axial nanowire heterostructures that could be identifiable in *Drosophila* fly gut tissue in a proof of concept experiment.[38]

1.2.2 Extracellular bio-interfaces

In addition to exploring intracellular bio-interfaces, examining cell-material interfaces extracellularly is of interest especially if the target component of the cell is the plasma membrane and the interface must be quickly formed. Drs. Bianxiao Cui's and Yi Cui's Labs have demonstrated that nanopillar arrays can minimally invasively pin embryonic cortical neuronal cell bodies [39] and more recently, that plasma membranes of HL-1 cardiomyocytes cultured on a quartz substrate with nanopillars can deform to wrap around the pillars but will not readily deform outwardly around invaginating structures

(Fig. 1.2C-D).[40] This differential membrane response to varying nanoscale topographical features must be considered during design of materials to be implanted into biological systems, as the tightness of the interface can vary significantly. At the membrane protein level, it was found that positively-curved membranes are Clathrin-mediated endocytosis (CME) hotspots. In particular, key CME proteins, such as clathrin and dynamin, are preferential for positively-curved membranes,[41] in contrast with many other membrane-associated proteins. Although these studies were performed primarily over quartz-based nanopillars, this concept can be applied to other semiconductor systems, suggesting that nanostructured semiconductor substrates can be used for investigating nanoscale topography-dependent processes in live cells.

Extracellular biointerfaces can also be enhanced by tuning mechanical properties of materials so that they match those of cellular components. Jiang *et al.* further explores this idea with their aforementioned 3D nanoporous Si particles.[8] These particles, when immersed in aqueous environments, exhibit a mechanical stiffness that is similar to that of components of extracellular matrices (ECM).[8] The increased surface area and roughness of the nanoporous particles, as well as decreased mechanical stiffness in aqueous environments, allow these particles to achieve tight cellular interfaces with many mammalian cells.

Extracellular bio-interfaces can also be tuned by external stimuli such as light. Pauzauskie *et al.* demonstrated a laser nanowire assembly method for locally manipulating and transporting nanowires to place one end of a 60 nm diameter cylindrical GaN nanowire against a HeLa cell membrane for several temporal

durations.[42] The ability to precisely arrange nanostructures with respect to their cellular targets can allow for meticulous control of bio-interfaces.

1.2.3 Tissue-level bio-interfaces

Tissue-level material interfaces can also be optimized during material synthesis. For example, Choi *et al.* demonstrated that soft materials like MoS_2-graphene heterostructures can form tight, conformal interfaces with retinal tissue *in vivo.*[43] We can also select for materials that can form close contacts with the ECM. Luo *et al.* demonstrated this concept with their anisotropic spicule SiNWs that, like a bee stinger, are harder to retract from collagen matrices.[13] This phenomenon was tested via atomic force microscopy (AFM) experiments in which spicules were mounted onto AFM tips and were subsequently inserted into and retracted from collagen matrices (Fig. 1.2E). The detachment force measured for these spicules and was found to be an order of magnitude higher than that of smooth nanowires (4.16 nN compared to 0.455 nN, respectively) (Fig. 1.2F).

Biodegradability without material fracturing is another important aspect of generating robust tissue level interfaces. Kang *et al.* developed a completely bioresorbable Si nanomembrane based device for intracranial pressure sensing.[44] The various components of the material include thin layers of SiO2 and a nanoporous Si membrane, which can degrade at rates of 8 nm/day and 23 nm/day, respectively, and can dissolve completely without fracture.[44]

1.3 Detecting cellular behaviors

1.3.1 Electrical signaling probes

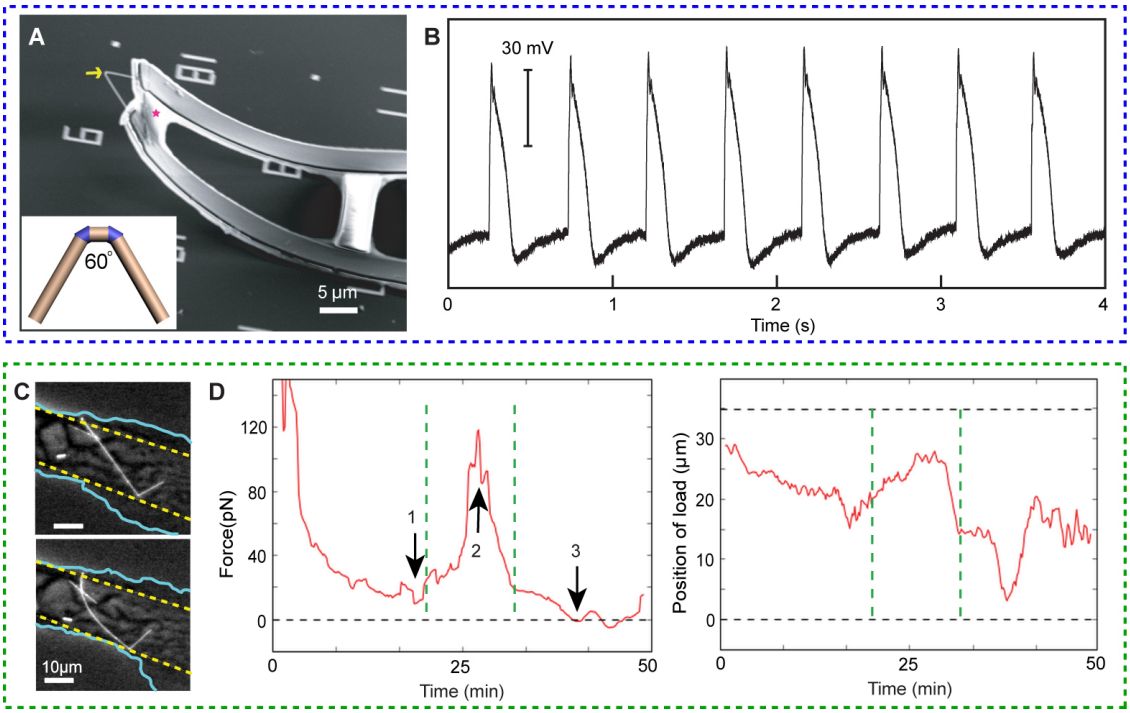

Figure 1.3. SiNWs can be used for intracellular sensing. (**A-B**) Intracellular electrical recording with a field effect transistor. (**A**) SEM image of a flexible NW-FET-based recording device. Yellow arrow highlights a kinked nanowire, and the magenta star marks part of a polymer backbone used to support metal interconnects. Inset displays kinked NW-FET consisting of two cis-linked kinked units with a probe tip angle of 60°. (**B**) Representative trace of intracellular electrical recording from a beating cardiomyocyte. (**C-D**) Intracellular force sensing. (**C**) Optical micrographs of Angiotensin II drug-induced HASMC contraction, showing straight (upper)/bent (lower) states (cyan, cell membranes; yellow, lamella boundary). (**D**) Time-lapse force data (left) with coincident-load position (right), showing a well-defined contraction peak (between dashed green lines). Upon introduction of Angiotensin II, a force minimum was observed due to relaxation of tension (arrow 1), followed by a contraction force peak (arrow 2), and a minimally strained state (arrow 3). Adapted with permission from ref (56). 2018 American Chemical Society.

Once robust bio-interfaces are achieved, materials can be used to detect cellular behaviors. These behaviors can include electrical and mechanical signaling in single

cells or whole tissues. Electrical signaling probes in cellular systems are of great interest due to limitations in currently-used technologies. While patch-clamp electrophysiology has revealed crucial mechanisms of biophysical behaviors in excitable cells, it is mechanically-invasive and is limited in its capability to measure electrical signals for long timespans. Field effect transistors (FETs) are an attractive alternative to this technology as they can be fabricated at length scales more compatible with biological systems. Tian *et al.* took advantage of this and fabricated nanowire-FETs (NW-FETs) using the aforementioned kinked nanowires, consisting of two cis-linked kinked units with probe tip angles of 60°, with heavy n++ type doping for the source and drain arms (Fig. 1.3A).[6] These NW-FETs sense target biological species by coupling interactions with those species with the surface potential of the channel and thus the channel conductance. Here, kinked NW-FETs were used as 3D probes that could be inserted into cells (Fig 1.3A).[6] These 3D probes are unique due to their nanoscale size, free-standing nature, and spatially separated FET and bulky interconnects, allowing for minimally invasive probing of electrical signaling in single cells. Electrical recordings, similar in quality to that of patch-clamp electrophysiology recordings, were demonstrated using these NW-FET probes in embryonic chicken cardiomyocytes (Fig. 1.3B).[6] Earlier work from Dr. Lieber's lab oriented olfactory cortex slices over NWFET arrays and produced extracellular recordings from various layers of cells.[45] The ability to tune the spatial arrangement and density of the NW-FETs in the array allows for multiplexed measurements across many length scales, which is especially relevant to teasing out neural circuitry.[45] These NW-FETs have now also

been integrated into polymeric meshes and function well after being injected through a syringe into mouse brains.[46]

1.3.2 Mechanical force probes

Mechanical forces experienced by cells and tissues can play crucial roles in tissue and organ function, homeostasis, and development. The current most widely-used techniques for probing these forces quantitatively both extracellularly and intracellularly include traction-force microscopy, optical tweezers, optical FRET sensors, and deformable material substrates.[47-49] Many of these tools are invasive and have length scales that are incompatible with probing components of single cells. However, recent work has demonstrated that more precise, minimally invasive cellular force measurements can be achieved with nanoscale material probes.[2,50,51] Dr. Christelle Prinz's group demonstrated the use of GaP nanowire arrays to detect forces associated with neuronal growth cone lamelapodia dynamics down to 15 pN.[51] Forces were measured by quantifying the displacement of fluorescently-labeled nanowire tips caused by growth and movement of neurons cultured atop the array.

Recent work by Zimmerman *et al.* uses a completely free-standing method to show that kinked SiNWs can probe intracellular forces in both HUVECs and human aortic smooth muscle cells (HASMCs).[2] Both of these cell types are phagocytic and using endogenous pathways, can internalize singly-kinked SiNWs.[3] These singly-kinked SiNWs were chosen so that the kink could be anchored to a part of the cytoskeleton, limiting rotational and translational movements of the nanowire (Fig. 1.3C). Intracellular forces experienced by the cells were then measured during live-cell imaging of kinked SiNW bending that occurred as a result of both drug-induced contractions, as well as

basal processes such as migration and division (Fig. 1.3C-D). Forces were quantified using Euler-Bernoulli beam theory.

1.4 Instructing cellular behavior

1.4.1 Topographical cues to instruct behavior

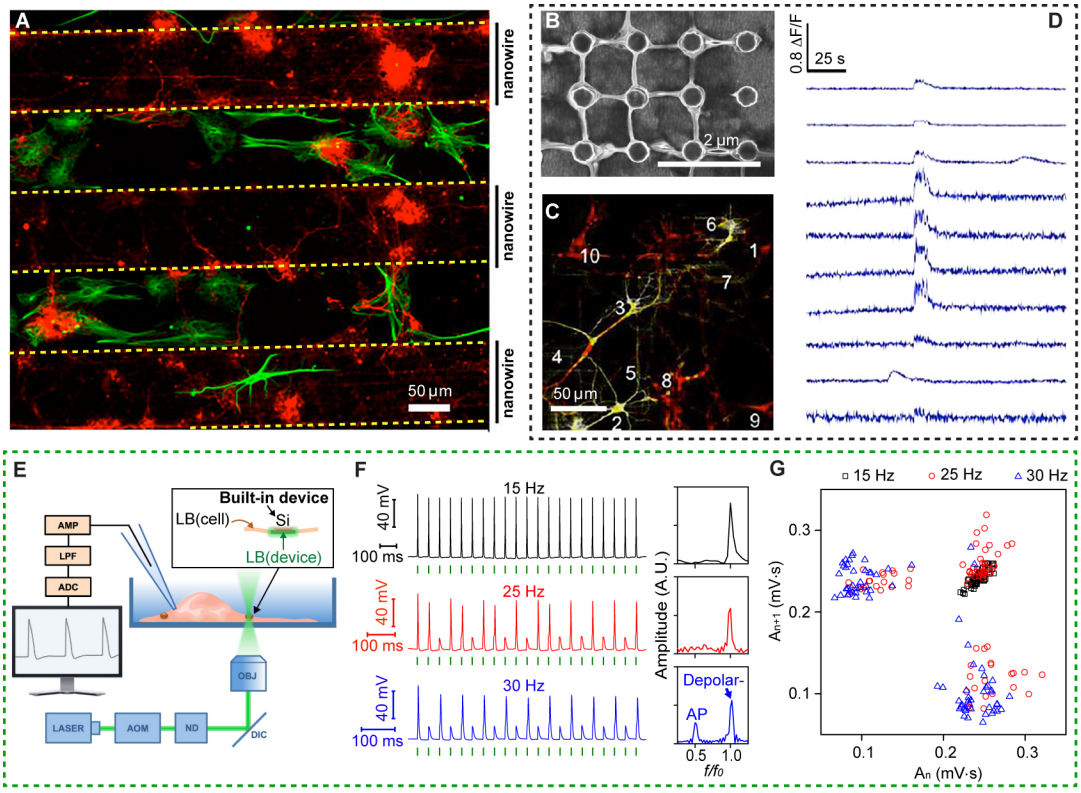

Figure 1.4. Si nanostructures can instruct cellular functions. (**A**) Neuronal cells (β-tubulin III, red) and glial cells (GFAP, green) on 100 µm-wide bands with dense arrays of GaP nanowires (indicated by vertical lines and "nanowires") separated by 100 µm-wide bands with a flat topography after 18 DIV. (**B-D**) Engineering highly-interconnected neuronal networks on InP nanowire scaffolds. (**B**) Neurite growth on an area of nanowires after 5 DIV showing anchoring and secondary branching of neurites at the nanowires. (**C**) Hippocampal neurons with correlated calcium signals. (**D**) ΔF/F vs time from numbered regions, suggesting high spatial correlation of neural activities as induced by the nanowire array. Top to bottom traces come from the regions of 1 to 10 in **C**. (**E-G**) Nanoporous Si particles for extracellular neuromodulation. (**E**) Experimental setup used to elicit action potentials in DRG neurons by illuminating a single Si particle attached to a cell. Neurons were patch-clamped in the current-clamp, whole-cell mode. AOM, acousto-optic modulator; ND, neutral density filters; DIC, dichroic mirror; OBJ,

(Figure 1.4 continued) microscope objective; AMP, amplifier; LPF, low-pass filter; ADC, analog-to-digital converter. Inset shows that a portion of the cell membrane functions as a built-in device. (**F**) Representative intracellular potential recordings of a DRG neuron to trains of laser pulses (5.32 μJ) at different frequencies, with corresponding FFTs (right). f and f_0 are output and input frequencies, respectively. Green bars indicate when laser pulses were delivered. (**G**) An area-based return map reveals an evolution of frequency-dependent 2D patterns. Data points are analyzed from 20 spikes per trial, 4 trials per frequency. Adapted with permission from ref (56). 2018 American Chemical Society.

In addition to detecting cellular behavior, semiconductor materials interfacing with biological systems can instruct single or ensemble cell behavior. The naturally occurring cues that inform cellular growth, excitability, and communication can be chemical, mechanical, topographical or even electrical in nature. Using biomaterials to mimic these naturally-occurring cues can be crucial in treating diseases characterized by aberrant cues. Traditional methods for generating physical cues to instruct cellular behavior include artificial substrates that have been patterned with chemical components of ECM or surface topographies such as invaginations or pillars. Work by Dr. Christelle Prinz's group showed that by fabricating substrates with patterned GaP nanowire regions, CNS neurons and glial cells can be spatially separated into distinct compartments (Fig. 1.4A).[4] The same group also showed that depending on the arrangement of the nanowires,[4,5,52] retinal ganglion neuron processes could be aligned along nanowire rows, suggesting the possibility of using nanowires to promote contact guidance, a phenomenon by which substrate geometry can guide cellular outgrowth or movement, of CNS neuronal processes. Vincent Daria's group also developed an isotropic arrangement of high-aspect-ratio InP nanowires into scaffolds that can provide strictly physical cues for neurite growth and interconnected neuronal networks, as shown in Fig. 1.4B.[53] Neurite extension in hippocampal neurons can be guided by

nanowire topography in these scaffolds and, as seen by calcium imaging studies, neuronal activity on the scaffold is highly coordinated (Figs. 1.4C-D). These studies suggest new neural engineering methods through topography control.

1.4.2 Electrical cues to instruct behavior

The most widely used methods of modulating cellular electrical excitability include patch clamp electrophysiology and optogenetics.[54,55] Semiconducting meso- and nanoscale materials are promising alternatives to these traditional methods given their minimally invasive and non-genetic manner. Jiang *et al.* used mesoporous Si particles to induce photothermal excitation of primary dorsal root ganglion neurons as shown in Fig. 1.4E-G.[8] After illuminating the plasma-membrane-supported Si particles, the fast photothermal effect from the Si induced a local temperature elevation, which subsequently caused a transient capacitance increase in the lipid bilayer and a depolarization of the bilayer due to capacitive current injection into the cells.

Nanoscale semiconductor devices offer an extremely promising direction for the synthesis of minimally invasive probes and manipulators of cellular behavior. Here, we have presented multiple approaches for the rational design of nanowire materials for the formation of robust bio-interfaces with an ability to detect and instruct behaviors in cellular- and tissue-level systems. Some of the main challenges that remain include the design of materials that are mechanically compliant with native tissue, targeting of materials to specific subcellular organelles for intracellular studies, development of a platform that can sense and stimulate via a logic-gated feedback loop, the ability to perform multiplexing to investigate coordination between cells in complex circuits, and the ability to precisely control the lifetime and fouling of materials in physiological

environments. Studies that continue to interface nanoscale materials with biological systems will deepen our understanding of how biological systems work and pave the way for novel life-saving therapeutics.

In my thesis, I synthesize and characterize a new Silicon nanowire material for use in extracellular modulation of cellular activity in three different biological systems. First, I use this material in a free-standing configuration for photoelectrochemical optical single cell neuronal excitability control. Secondly, I demonstrate that this material can be incorporated at a high density into a polymeric grid structure and used for optical training of cardiomyocytes to beat at a target frequency with a moving optical stimulus. Last, I label this material with an antibody that can bind specifically to T cells, generating free-standing T cell-nanowire complexes in solution, and optically modulate T cell activation in populations of T cells. My work is significant in its demonstration of non-invasive, non-genetic optical control of cellular behavior and can be advantageous for both fundamental bioelectric studies and photo-responsive therapeutics.

1.5 References

1. Zhang, A. Q.; Lieber, C. M. Nano-Bioelectronics. *Chemical Reviews* **2016**, *116*, 215-257.
2. Zimmerman, J. F.; Murray, G. F.; Wang, Y.; Jumper, J. M.; Austin, J. R.; Tian, B. Free-Standing Kinked Silicon Nanowires for Probing Inter- and Intracellular Force Dynamics. *Nano Letters* **2015**, *15*, 5492-5498.
3. Zimmerman, J. F.; Parameswaran, R.; Murray, G.; Wang, Y. C.; Burke, M.; Tian, B. Z. Cellular uptake and dynamics of unlabeled freestanding silicon nanowires. *Science Advances* **2016**, *2*.
4. Piret, G.; Perez, M. T.; Prinz, C. N. Support of Neuronal Growth Over Glial Growth and Guidance of Optic Nerve Axons by Vertical Nanowire Arrays. *ACS Applied Materials & Interfaces* **2015**, *7*, 18944-18948.
5. Prinz, C. N. Interactions between semiconductor nanowires and living cells. *Journal of Physics-Condensed Matter* **2015**, *27*.
6. Tian, B. Z.; Cohen-Karni, T.; Qing, Q.; Duan, X. J.; Xie, P.; Lieber, C. M. Three-Dimensional, Flexible Nanoscale Field-Effect Transistors as Localized Bioprobes. *Science* **2010**, *329*, 830-834.
7. Tian, B. Z.; Liu, J.; Dvir, T.; Jin, L. H.; Tsui, J. H.; Qing, Q.; Suo, Z. G.; Langer, R.; Kohane, D. S.; Lieber, C. M. Macroporous nanowire nanoelectronic scaffolds for synthetic tissues. *Nature Materials* **2012**, *11*, 986-994.
8. Jiang, Y. W.; Carvalho-de-Souza, J. L.; Wong, R. C. S.; Luo, Z. Q.; Isheim, D.; Zuo, X. B.; Nicholls, A. W.; Jung, I. W.; Yue, J. P.; Liu, D. J.; Wang, Y. C.; De Andrade, V.; Xiao, X. H.; Navrazhnykh, L.; Weiss, D. E.; Wu, X. Y.; Seidman, D. N.; Bezanilla, F.; Tian, B. Z. Heterogeneous silicon mesostructures for lipid-supported bioelectric interfaces. *Nature Materials* **2016**, *15*, 1023-1030.
9. Fu, T. M.; Hong, G. S.; Zhou, T.; Schuhmann, T. G.; Viveros, R. D.; Lieber, C. M. Stable long-term chronic brain mapping at the single-neuron level. *Nature Methods* **2016**, *13*, 875-+.
10. Liu, J.; Fu, T. M.; Cheng, Z. G.; Hong, G. S.; Zhou, T.; Jin, L. H.; Duvvuri, M.; Jiang, Z.; Kruskal, P.; Xie, C.; Suo, Z. G.; Fang, Y.; Lieber, C. M. Syringe-injectable electronics. *Nature Nanotechnology* **2015**, *10*, 629-+.
11. Hwang, S. W.; Park, G.; Edwards, C.; Corbin, E. A.; Kang, S. K.; Cheng, H. Y.; Song, J. K.; Kim, J. H.; Yu, S.; Ng, J.; Lee, J. E.; Kim, J.; Yee, C.; Bhaduri, B.; Su, Y.; Omennetto, F. G.; Huang, Y. G.; Bashir, R.; Goddard, L.; Popescu, G.; Lee, K. M.; Rogers, J. A. Dissolution Chemistry and Biocompatibility of Single-Crystalline Silicon Nanomembranes and Associated Materials for Transient Electronics. *ACS Nano* **2014**, *8*, 5843-5851.
12. Hwang, S. W.; Tao, H.; Kim, D. H.; Cheng, H. Y.; Song, J. K.; Rill, E.; Brenckle, M. A.; Panilaitis, B.; Won, S. M.; Kim, Y. S.; Song, Y. M.; Yu, K. J.; Ameen, A.; Li, R.; Su, Y. W.; Yang, M. M.; Kaplan, D. L.; Zakin, M. R.; Slepian, M. J.; Huang, Y. G.; Omenetto, F. G.; Rogers, J. A. A Physically Transient Form of Silicon Electronics. *Science* **2012**, *337*, 1640-1644.
13. Luo, Z. Q.; Jiang, Y. W.; Myers, B. D.; Isheim, D.; Wu, J. S.; Zimmerman, J. F.; Wang, Z. G.; Li, Q. Q.; Wang, Y. C.; Chen, X. Q.; Dravid, V. P.; Seidman,

D. N.; Tian, B. Z. Atomic gold-enabled three-dimensional lithography for silicon mesostructures. *Science* **2015**, *348*, 1451-1455.
14. Tian, B. Z.; Xie, P.; Kempa, T. J.; Bell, D. C.; Lieber, C. M. Single-crystalline kinked semiconductor nanowire superstructures. *Nature Nanotechnology* **2009**, *4*, 824-829.
15. Tian, B. Z.; Zheng, X. L.; Kempa, T. J.; Fang, Y.; Yu, N. F.; Yu, G. H.; Huang, J. L.; Lieber, C. M. Coaxial silicon nanowires as solar cells and nanoelectronic power sources. *Nature* **2007**, *449*, 885-U888.
16. Yang, C.; Zhong, Z. H.; Lieber, C. M. Encoding electronic properties by synthesis of axial modulation-doped silicon nanowires. *Science* **2005**, *310*, 1304-1307.
17. Gudiksen, M. S.; Lauhon, L. J.; Wang, J.; Smith, D. C.; Lieber, C. M. Growth of nanowire superlattice structures for nanoscale photonics and electronics. *Nature* **2002**, *415*, 617-620.
18. Lauhon, L. J.; Gudiksen, M. S.; Wang, C. L.; Lieber, C. M. Epitaxial core-shell and core-multishell nanowire heterostructures. *Nature* **2002**, *420*, 57-61.
19. Zhong, Z. H.; Wang, D. L.; Cui, Y.; Bockrath, M. W.; Lieber, C. M. Nanowire crossbar arrays as address decoders for integrated nanosystems. *Science* **2003**, *302*, 1377-1379.
20. Day, R. W.; Mankin, M. N.; Gao, R. X.; No, Y. S.; Kim, S. K.; Bell, D. C.; Park, H. G.; Lieber, C. M. Plateau-Rayleigh crystal growth of periodic shells on one-dimensional substrates. *Nature Nanotechnology* **2015**, *10*, 345-352.
21. Ledesma, H. A.; Tian, B. Z. Nanoscale silicon for subcellular biointerfaces. *Journal of Materials Chemistry B* **2017**, *5*, 4276-4289.
22. Zimmerman, J.; Parameswaran, R.; Tian, B. Z. Nanoscale semiconductor devices as new biomaterials. *Biomaterials Science* **2014**, *2*, 619-626.
23. Keren, K.; Yam, P. T.; Kinkhabwala, A.; Mogilner, A.; Theriot, J. A. Intracellular fluid flow in rapidly moving cells. *Nature Cell Biology* **2009**, *11*, 1219-U1137.
24. Gomez-Martinez, R.; Hernandez-Pinto, A. M.; Duch, M.; Vazquez, P.; Zinoviev, K.; de la Rosa, E. J.; Esteve, J.; Suarez, T.; Plaza, J. A. Silicon chips detect intracellular pressure changes in living cells. *Nature Nanotechnology* **2013**, *8*, 517-521.
25. Kornienko, N.; Sakimoto, K. K.; Herlihy, D. M.; Nguyen, S. C.; Alivisatos, A. P.; Harris, C. B.; Schwartzberg, A.; Yang, P. D. Spectroscopic elucidation of energy transfer in hybrid inorganic-biological organisms for solar-to-chemical production. *Proceedings of the National Academy of Sciences of the United States of America* **2016**, *113*, 11750-11755.
26. Sakimoto, K. K.; Wong, A. B.; Yang, P. D. Self-photosensitization of nonphotosynthetic bacteria for solar-to-chemical production. *Science* **2016**, *351*, 74-77.
27. Campagnolo, P.; Chiappini, C.; Leonardo, V.; Becce, M.; Perbellini, F.; Terracciano, C.; Smart, N.; Harding, S. A.; Stevens, M. M. Porous silicon nanoneedles for localised in situ gene transfer for cardiac therapy. *Cardiovascular Research* **2016**, *111*, S87-S87.

28. Chiappini, C.; De Rosa, E.; Martinez, J. O.; Liu, X.; Steele, J.; Stevens, M. M.; Tasciotti, E. Biodegradable silicon nanoneedles delivering nucleic acids intracellularly induce localized in vivo neovascularization. *Nature Materials* **2015**, *14*, 532-539.
29. Qing, Q.; Jiang, Z.; Xu, L.; Gao, R. X.; Mai, L. Q.; Lieber, C. M. Free-standing kinked nanowire transistor probes for targeted intracellular recording in three dimensions. *Nature Nanotechnology* **2014**, *9*, 142-147.
30. Hannon, J. B.; Kodambaka, S.; Ross, F. M.; Tromp, R. M. The influence of the surface migration of gold on the growth of silicon nanowires. *Nature* **2006**, *440*, 69-71.
31. Wan, Y.; Zhao, D. Y. On the controllable soft-templating approach to mesoporous silicates. *Chemical Reviews* **2007**, *107*, 2821-2860.
32. Fang, Y.; Jiang, Y. W.; Cherukara, M. J.; Shi, F. Y.; Koehler, K.; Freyermuth, G.; Isheim, D.; Narayanan, B.; Nicholls, A. W.; Seidman, D. N.; Sankaranarayanan, S. K. R. S.; Tian, B. Z. Alloy-assisted deposition of three-dimensional arrays of atomic gold catalyst for crystal growth studies. *Nature Communications* **2017**, *8,* 2014.
33. Kempa, T. J.; Cahoon, J. F.; Kim, S. K.; Day, R. W.; Bell, D. C.; Park, H. G.; Lieber, C. M. Coaxial multishell nanowires with high-quality electronic interfaces and tunable optical cavities for ultrathin photovoltaics. *Proceedings of the National Academy of Sciences of the United States of America* **2012**, *109*, 1407-1412.
34. Parameswaran, R.; Carvalho-de-Souza, J. L.; Jiang, Y. W.; Burke, M.; Zimmerman, J.; Koehler, K.; Phillips, A.; Yi, J.; Adams, E.; Bezanilla, F.; Tian, B. Z. Photoelectrochemical modulation of neuronal activity with free-standing coaxial silicon nanowires. *Nature Nanotechnology* **2018**.
35. Almquist, B. D.; Melosh, N. A. Fusion of biomimetic stealth probes into lipid bilayer cores. *Proceedings of the National Academy of Sciences of the United States of America* **2010**, *107*, 5815-5820.
36. Wong Shi Kam, N.; O'Connell, M.; Wisdom, J. A.; Dai, H. Carbon nanotubes as multifunctional biological transporters and near-infrared agents for selective cancer cell destruction. *Proceedings of the National Academy of Sciences of the United States of America* **2005**, *102*, 11600-11605.
37. Lee, J. H.; Zhang, A. Q.; You, S. S.; Lieber, C. M. Spontaneous Internalization of Cell Penetrating Peptide-Modified Nanowires into Primary Neurons. *Nano Letters* **2016**, *16*, 1509-1513.
38. Adolfsson, K.; Persson, H.; Wallentin, J.; Oredsson, S.; Saumelson, L.; Tegenfeldt, J. O.; Borstrom, M. T.; Prinz, C. Fluorescent Nanowire Heterostructures as a Versatile Tool for Bology Applications. *Nano Letters*. **2013**, *13*, 4728-4732.
39. Xie, C.; Hanson, L.; Xie, W. J.; Lin, Z. L.; Cui, B. X.; Cui, Y. Noninvasive Neuron Pinning with Nanopillar Arrays. *Nano Letters* **2010**, *10*, 4020-4024.
40. Santoro, F.; Zhao, W. T.; Joubert, L. M.; Duan, L. T.; Schnitker, J.; van de Burgt, Y.; Lou, H. Y.; Liu, B. F.; Salleo, A.; Cui, L. F.; Cui, Y.; Cui, B. X. Revealing the Cell-Material Interface with Nanometer Resolution by Focused Ion Beam/Scanning Electron Microscopy. *Acs Nano* **2017**, *11*, 8320-8328.

41. Zhao, W. T.; Hanson, L.; Lou, H. Y.; Akamatsu, M.; Chowdary, P. D.; Santoro, F.; Marks, J. R.; Grassart, A.; Drubin, D. G.; Cui, Y.; Cui, B. X. Nanoscale manipulation of membrane curvature for probing endocytosis in live cells. *Nature Nanotechnology* **2017**, *12*, 750-756.
42. Pauzauskie, P. J.; Radenovic; Trepagnier, E.; Shroff H.; Yang P.; Liphardt J. Optical trapping and integration of semiconductor nanowire assemblies in water. *Nature Materials.* **2006**, *5*, 97-101.
43. Choi, C.; Choi, M. K.; Liu, S.; Kim, M. S.; Park, O. K.; Im, C.; Kim, J.; Qin, X.; Lee, G. J.; Cho, K. W.; Kim, M.; Joh, E.; Lee, J.; Son, D.; Kwon, S-H; Jeom, N. L.; Song, Y. M.; Lu, N.; Kim, D-H. Human-eye-inspired soft optoelectronic device using high-density MoS2-graphene curved image sensor array. *Nature Communications.* **2017**, *8*, 1664.
44. Kang, S-K; Murphy, R. K. J.; Hwang, S-W; Lee, S. M.; Harburg, D. V.; Krueger, N. A.; Shin, J.; Gamble, P.; Cheng, H.; Yu, S.; Liu, Z.; McCall J. G.; Stephen, M.; Ying, H.; Kim, J.; Park, G.; Webb, R. C.; Lee, C. H.; Chung, S.; Wie, D. S.; Gujar, A. D.; Vemulapalli, B.; Kim, A. H.; Lee, K-M; Cheng, J.; Hunag, Y.; Lee, S. H.; Braun, P. V.; Ray, W. Z.; Rogers, J. Bioresorbable silicon electronic sensors for the brain. *Nature*. **2016**, *530*, 71-76.
45. Qing, Q.; Pal, S. K.; Tian, B.; Duan, X.; Timko, B. P.; Cohen-Karni, T.; Murthy, V. N.; Lieber, C. M. Nanowire transistor arrays for mapping neural circuits in acute brain slices. *Proceedings of the National Academy of Sciences of the United States of America.* **2010,** *107*, 1882-1887.
46. Liu, J.; Fu, T-M.; Cheng, Z.; Hong, G.; Zhou, T.; Jin, L.; Duvvuri, M.; Jiang, Z.; Kruskal, P.; Xie, C.; Suo, Z.; Fang, Y.; Lieber, C. M. Syringe-injectable electronics. *Nature Nanotechnology.* **2015**, *10,* 629-636.
47. Bippes, C. A.; Muller, D. J. High-resolution atomic force microscopy and spectroscopy of native membrane proteins. *Reports on Progress in Physics* **2011**, *74*.
48. Zheng, X. Y. R.; Zhang, X. Microsystems for cellular force measurement: a review. *Journal of Micromechanics and Microengineering* **2011**, *21*.
49. Addae-Mensah, K. A.; Wikswo, J. P. Measurement techniques for cellular biomechanics in vitro. *Experimental Biology and Medicine* **2008**, *233*, 792-809.
50. Hanson, L.; Zhao, W. T.; Lou, H. Y.; Lin, Z. C.; Lee, S. W.; Chowdary, P.; Cui, Y.; Cui, B. X. Vertical nanopillars for in situ probing of nuclear mechanics in adherent cells. *Nature Nanotechnology* **2015**, *10*, 554-U592.
51. Hallstrom, W.; Lexholm, M.; Suyatin, D. B.; Hammarin, G.; Hessman, D.; Samuelson, L.; Montelius, L.; Kanje, M.; Prinz, C. N. Fifteen-Piconewton Force Detection from Neural Growth Cones Using Nanowire Arrays. *Nano Letters* **2010**, *10*, 782-787.
52. Persson, H.; Li, Z.; Tegenfeldt, J. O.; Oredsson, S.; Prinz, C. N. From immobilized cells to motile cells on a bed-of-nails: effects of vertical nanowire array density on cell behaviour. *Scientific Reports* **2015**, *5*.
53. Gautam, V.; Naureen, S.; Shahid, N.; Gao, Q.; Wang, Y.; Nisbet, D.; Jagadish, C.; Daria, V. R. Engineering Highly Interconnected Neuronal Networks on Nanowire Scaffolds. *Nano Letters* **2017**, *17*, 3369-3375.

54. Kim, C. K.; Adhikari, A.; Deisseroth, K. Integration of optogenetics with complementary methodologies in systems neuroscience. *Nature Reviews Neuroscience* **2017**, *18*, 222-235.
55. Packer, A. M.; Roska, B.; Hausser, M. Targeting neurons and photons for optogenetics. *Nature Neuroscience* **2013**, *16*, 805-815.
56. Parameswaran, R.; Tian, B. Z. Rational Design of Semiconductor Nanostructures for Functional Biointerfaces. *Acc. Chem. Res.* **2018**, *51* (5), 1014-1022.

Chapter 2. Development and characterization of coaxial silicon nanowire structures

2.1 Introduction

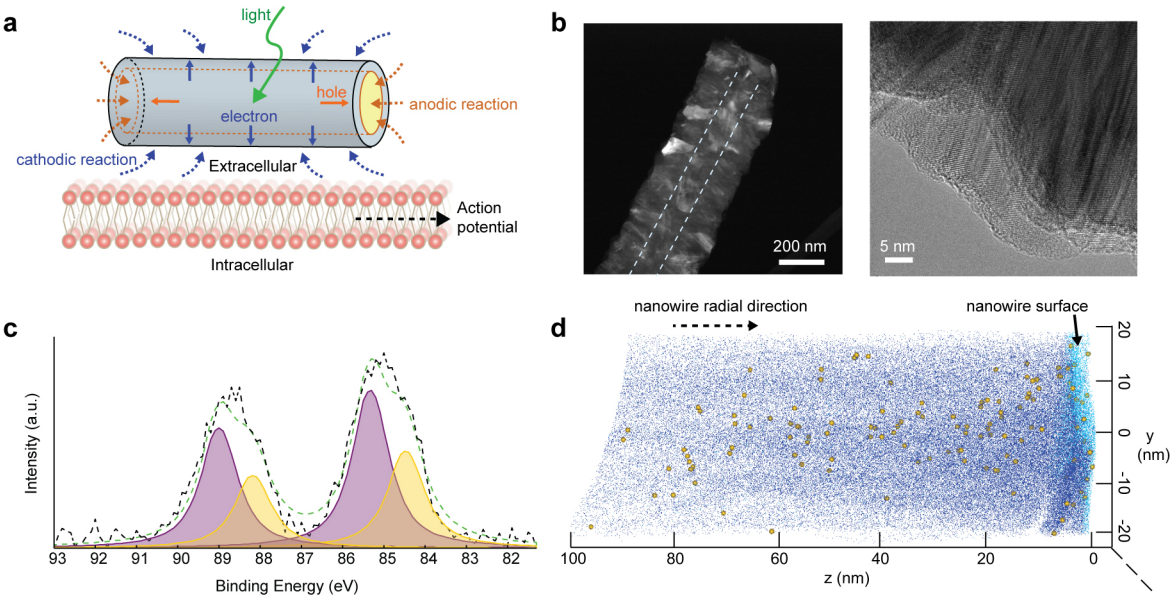

Figure 2.1. X-ray photoelectron spectroscopy and atom probe tomography reveal the presence of atomic Au on coaxial nanowire surfaces. **(a)** Schematic of the Faradaic current produced by a PIN-SiNW at the neuronal cell membrane upon light stimulation, inducing action potential generation in the neuron via membrane depolarization. Solid arrows represent movement of electrons and holes towards n-type and p-type Si respectively upon light stimulation. Dotted lines represent the cathodic and anodic reactions, respectively. **(b)** HAADF STEM image of PIN-SiNW (left) with p-type core outlined by white dotted line. This is a representative image from one of a total of 64 PIN-SiNWs imaged from 2 independent experiments. TEM image of PIN-SiNW (right). This is a representative image from one of a total of 8 PIN-SiNWs imaged from 3 independent experiments. **(c)** XPS spectrum (black dotted line) and the fitted curve (green dotted line) of Au 4f signals from the PIN-SiNWs. Deconvoluted peaks of Au 4f 7/2 and Au 4f 5/2 at 84.46 eV and 88.13 eV (yellow) represent nanoclustered Au species. Au 4f 7/2 and Au 4f 5/2 peaks at 85.4 eV and 89 eV (purple) represent atomic-like Au species. **(d)** 3D chemical reconstruction of local electrode APT data from a single PIN-SiNW displaying Si atoms (dark blue dots, 10% of all Si atoms displayed), O atoms (light blue dots, 100% of all O atoms displayed), and Au atoms (yellow balls, 100% of all Au atoms displayed). This is representative data from one of 3 independent probes that were prepared for APT analysis. Adapted with permission from ref (31).

Silicon (Si) nanomaterials are promising candidates for modulators of cellular activity and membrane votlage as they have been widely used for many biophysical or biomedical applications due to their highly tunable electrical and chemical properties, ability to absorb a broad range of wavelengths of light, and biocompatibility [3,8,11-18]. Si nanowires (SiNWs) are particularly advantageous due to their unique one-dimensional structure, precisely tunable doping profiles during growth, nanoscale diameter that allows for high spatial specificity, and ability to be dispersed in a drug-like fashion[19,20]. Here, we fabricate coaxial p-type/intrinsic/n-type (PIN) SiNWs, consisting of p-doped cores, and intrinsic and n-doped shells[21], to wirelessly and photoelectrochemically modulate cellular membrane voltage (Fig. 2.1a). Upon light stimulation at a cell-PIN-SiNW interface, electrons move towards the n-type shell and holes to the p-type core, inducing a cathodic process at the n-shell[22] that can locally depolarize a target cell (Fig 2.1a).

2.2 Characterization of coaxial nanowire surfaces

Sample	atomic-like 5/2 peak	atomic-like 7/2 peak	nanoclustered 5/2 peak	nanoclustered 7/2 peak
metallic Au				
p type SiNW	89.1	85.4	88.6	84.9
PIN-SiNW 1	88.8	85.1	88.3	84.6
PIN-SiNW 2	88.9	85.2	88	84.4
PIN-SiNW 3	88.9	85.2	87.9	84.3
PIN-SiNW 4	89	84.4	88.1	84.4
PIN-SiNW 5	89	85.4	88.1	84.5
PIN-SiNW 6	89	85.3	88.2	84.5

Sample	metallic 5/2 peak	metallic 7/2 peak
metallic Au	87.5	83.4
p type SiNW	87.7	84
PIN-SiNW 1		
PIN-SiNW 2		
PIN-SiNW 3		
PIN-SiNW 4		
PIN-SiNW 5		
PIN-SiNW 6		

Table 2.1. Au 4f binding energies for metallic Au, p-type SiNW, and PIN-SiNW samples. Atomic-like Au 5/2 and 7/2 peak, nanoclustered Au 5/2 and 7/2 peak, and metallic Au peak binding energies are displayed. Adapted with permission from ref (31).

The PIN-SiNWs were synthesized via a combination of gold (Au) nanoparticle (NP)-catalyzed vapor-liquid-solid growth of p-type SiNW cores, vacuum annealing, and a final vapor-solid growth of Si shells (Methods). High-angle annular dark field (HAADF) scanning transmission electron microscope (STEM) and transmission electron microscopy (TEM) show a final nanowire diameter of 200-250 nm with polycrystalline surfaces (Fig. 2.1b). NW shell synthesis of this kind at high temperatures and low pressures favors diffusion of the gold catalyst down the sidewalls of the NWs, resulting in atomic gold accumulation around the shells[23,24]. X-ray photoelectron spectroscopy (XPS) of PIN-SiNWs attached to their growth substrate indicates the presence of two types of Au within 7-10 nm from the surface of the NWs (Fig. 2.1c, Table 2.1). XPS peaks with binding energies of 84.5 eV and 88.1 eV represent Au nanoclusters, while

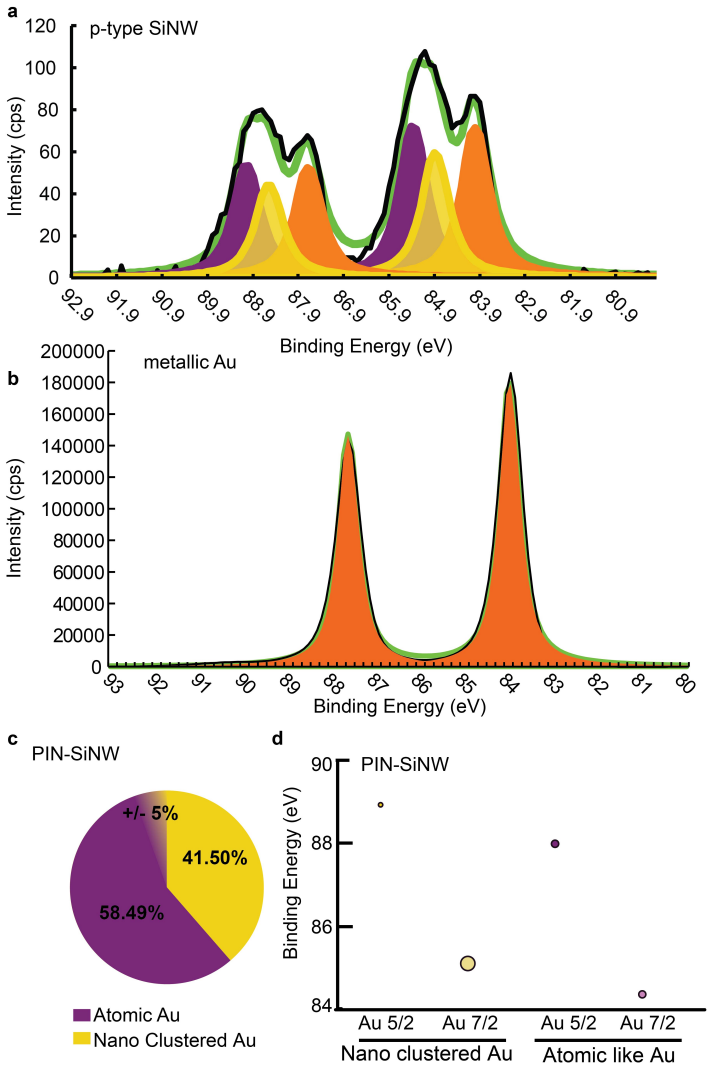

Figure 2.2. Comparison of XPS Au 4f spectra from PIN-SiNW, p-type SiNW, and metallic Au samples reveals that PIN-SiNW surfaces contain atomic and nanoclustered Au. (a) Au 4f XPS spectrum of control p-type SiNWs (black line) was modeled (green line). Deconvoluted peaks of Au 4f 7/2 and Au 4f 5/2 at 84.9 eV and 88.6 eV (yellow) represent nanoclustered Au species. Au 4f 7/2 and Au 4f 5/2 peaks at 85.4 eV and 89.1 eV (purple) represent atomic-like Au species. **(b)** XPS spectrum of metallic Au sample displaying Au 4f peaks. **(c)** Pie chart representing the average percentage of atomic-like Au and nanoclustered Au species from 6 PIN-SiNW samples. **(d)** Average binding energies for Au 5/2 and Au 7/2 nanoclustered Au and atom-like Au peaks from 6 PIN-SiNW samples. Size of the circle represents the standard error about the average. Adapted with permission from ref (31).

those with binding energies of 85.4 eV and 89.0 eV highlight the presence of atomic Au species (Fig. 2.1c, Table 2.1, Fig. 2.2). On average, 58.5% of the Au present is

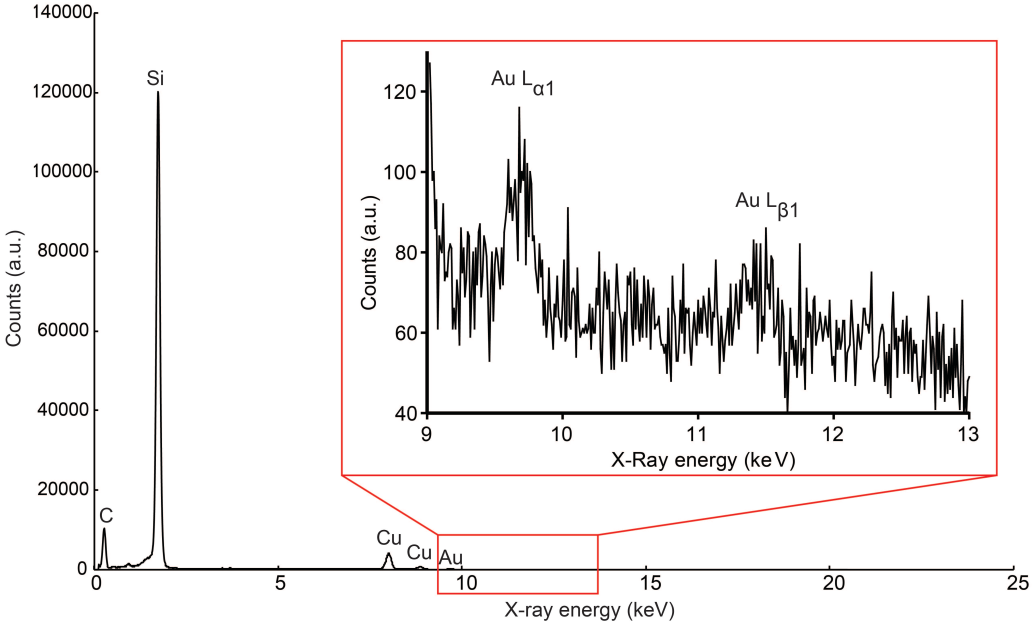

Figure 2.3. Energy dispersive x-ray spectrum for a single PIN-SiNW displaying Au peaks. Energy dispersive x-ray spectroscopy (EDS) was performed on 6 different PIN-SiNWs and characteristic Au elemental peaks were measured. Specifically, both Au Lα1 and Lβ1 peaks were detected above baseline at 9.7 and 11.4 keV X-ray energies (red boxed inset). Adapted with permission from ref (31).

represented by the atomic Au and 41.5% is represented by the nanoclustered Au (Fig. 2.2), and no metallic Au is identified. Energy dispersive x-ray spectroscopy (EDS) further confirms this result in single PIN-SiNWs. Spectra acquired displayed characteristic Au Lα1 and Lβ1 peaks at 9.7 and 11.4 keV X-ray energies respectively, thus confirming the presence of Au atoms in single PIN-SiNW nanowires (Fig. 2.3).

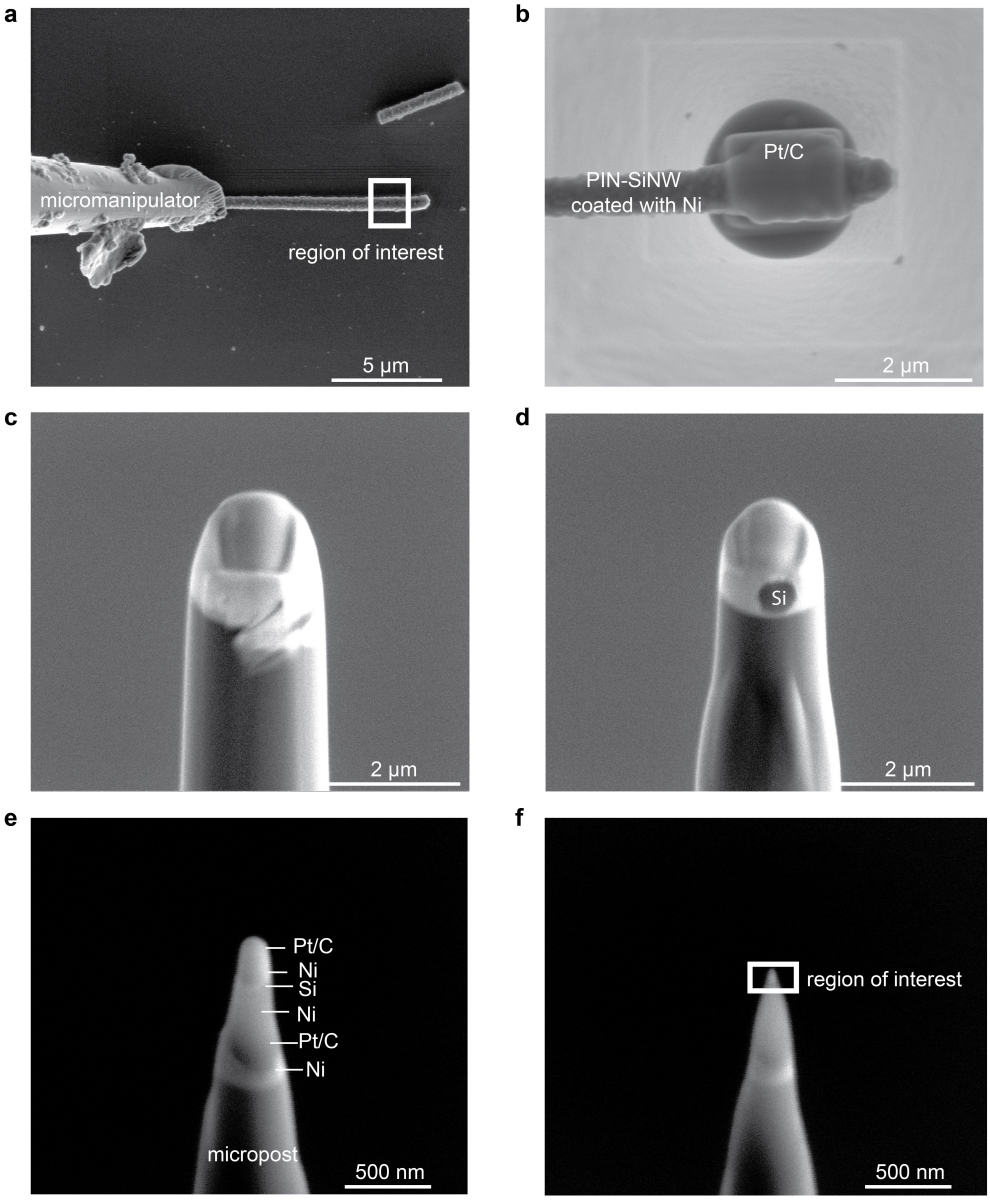

Figure 2.4. FIB allows for the fabrication of a fine tip for APT of PIN-SiNW samples. **(a-f)** SEM images of the APT tip preparation process. **(a)** Micromanipulator picking up a single Ni coated PIN-SiNW of interest from Si wafer subtrate. **(b)** PIN-SiNW bound to the Si micropost with Pt/C composite at the region of interest near the tip of the NW. **(c)** Sample pre-cut with a 30 kV Ga+ ion beam. **(d)** Sample milled with a 30 kV Ga+ ion beam. **(e)** Sample tip sharpened with a 5 kV Ga+ ion beam. Various material layers are indicated **(f)** Sample tip cleaned and region of interest for APT indicated. Adapted with permission from ref (31).

To more definitively characterize the amount and spatial distribution of atomic Au in our NWs, we performed local electrode atom probe tomography (APT) on a single PIN-SiNW (Fig. 2.4). The APT data demonstrate the existence of atomic Au in band-like domains with additional accumulation at the surface (Fig. 2.1d). We believe that the high temperature and low pressure conditions used for annealing and subsequent shell depositions allow for complete Au catalyst diffusion down the sidewalls of the nanowire cores [23,24] and the subsequent Au migration into the shells through grain boundaries or gettering effect [25]. Despite the dominant argument that atomic Au generates deep traps in Si, the Au at the Si surface may also confer properties that can be useful in a photoelectrochemical processes during cellular excitability modulation. Specifically, surface atomic Au may alter the surface states of the Si in such a way that is beneficial for reducing NW impedance in aqueous solutions [26], thus favoring the production of faradaic, not capacitive currents, as in traditional photoelectrochemical cells.

2.3 Estimation of the single nanowire photoelectrochemical behavior

We next developed a method to measure the photocurrents from single PIN-SiNWs in an interconnect free configuration, using a patch clamp setup under physiological conditions (modified Tyrode's solution), in response to a 532 nm light illumination, which was chosen according to previously measured action spectra for PIN-SiNWs[27]. We grew PIN-SiNWs with final diameters inside of quartz capillary tubes, pulled them into patch pipettes, and mounted them onto a patch clamp set-up. The laser was shone onto single NWs positioned so as to minimize any changes in pipette resistance due to increases in temperature produced by light absorption (Fig. 2.5a). All

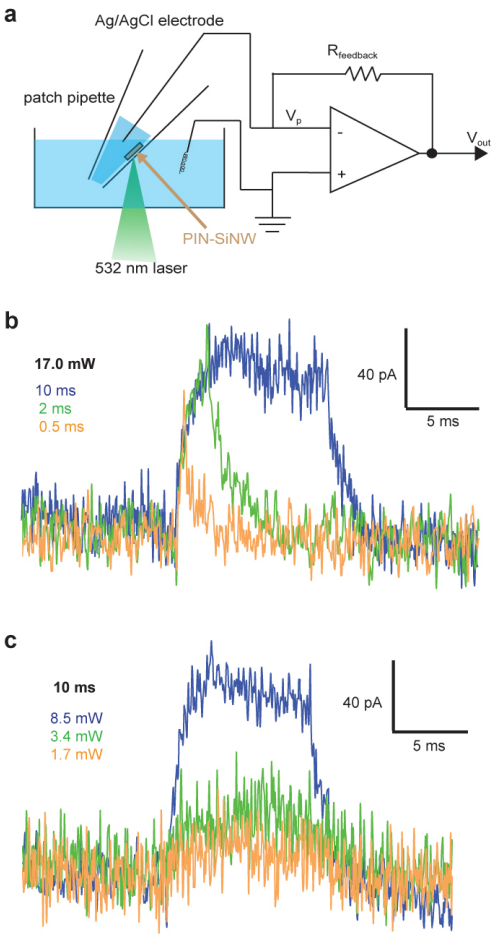

Figure 2.5. Single nanowire recordings reveal that coaxial Si nanowires are photoelectrochemical current sources. (a) Schematic of photocurrent measurement set-up. **(b)** Photocurrent traces from a single PIN-SiNW illuminated with a 532 nm laser at 17 mW for durations of 0.5 ms (orange), 2 ms (green), or 10 ms (blue). **(c)** Photocurrent traces from a single PIN-SiNW illuminated with a 532 nm laser at 8.5 mW (blue), 3.4 mW (green), or 1.7 mW (orange) for a duration of 10 ms. The traces in (**b**) and (**c**) are representative ones from a total of 40 current traces measured from 5 independent PIN-SiNWs. Adapted with permission from ref (31).

measurements were performed in voltage clamp mode, holding the voltage at zero in order to function as virtual ground. Keeping the power constant at 17 mW, we first altered the laser pulse duration (Fig. 2.5b). Measured pipette currents were characterized by a sharp and fast initial rise in current, likely limited by the system bandwidth, to peaks of 50.7 pA, 83.5 pA, and 101 pA for 0.5, 2, and 10 ms pulses,

respectively (Fig. 2.5b). While the observed currents do not represent absolute values of photocurrents produced by single PIN-SiNWs, as some current will be inevitably shunted by the surrounding solution, much can still be garnered from the relative amplitudes and durations of the photocurrents measured. Notably, the current resulting from the 10 ms pulse was sustained at 101 pA for the whole illumination duration (Fig. 2.5b). This production of a sustained current is not characteristic of a capacitive current given that the NW-associated electrical capacitance is below the pF range [28-30], and instead is suggestive of a faradaic process. This observed faradaic process, characterized by electron transfer between the NW and the electrolyte, may be particularly favorable in the context of biological systems as it mimicks basic cellular processes that inherently utilize redox reactions. Additionally, we observed light intensity-dependent current generation in another PIN-SiNW (Fig. 2.5c). For a laser pulse duration of 10 ms, the photocurrent peaks were measured to be 120 pA, 43.1 pA, and 22.3 pA for laser powers of 8.5 mW, 3.4 mW, and 1.7 mW, respectively. The polarity of the current suggests a photocathodic reaction over the PIN-SiNW surface. When the laser spot was moved off the nanowire onto plain glass, no current was

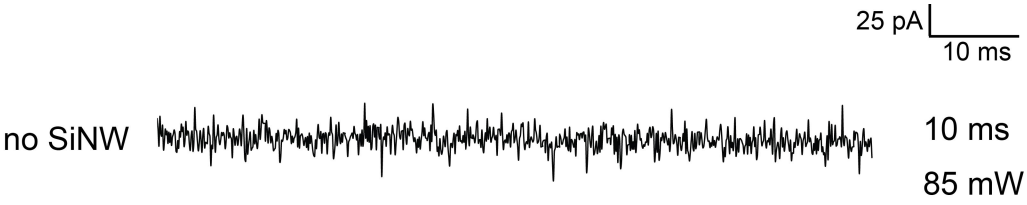

Figure 2.6. Laser stimulation in the absence of a SiNW produces no measurable photocurrent. Photocurrent trace from pipette glass with no SiNW illuminated with a 532 nm laser at 85 mW for a duration of 10 ms. Adapted with permission from ref (31).

recorded (Fig. 2.6). The observed unipolar photoelectrochemical current, for up to 10 ms (*i.e.*, a time scale relevant to neural excitation), suggests that the solution reaction kinetics for light-generated hole carriers is much slower than that for electrons, partially due to the much smaller exposed surface area for p-type Si core. We hypothesize that the surface atomic gold may also affect the observed non-equilibrium photoelectrochemical current production.

2.4 Conclusions and Outlook

In this chapter, we have demonstrated that we can enhance diffusion of the AuNP catalyst down the sidewalls of coaxial PIN-SiNWs and that this Au exists on the surface of these nanowires in the form of atomic Au. We have additionally developed a new method for measuring photocurrent from single nanowires using a modified patch clamp electrophysiology set-up in voltage clamp mode and measured sustained cathodic photocurrents from individual PIN-SiNWs that change in amplitude and duration with changes in laser power and duration. This material has the potential to be a non-invasive, non-genetic extracellular modulator of plasma membrane potential in cells.

2.5 Experimental Methods

2.5.1 Nanowire synthesis

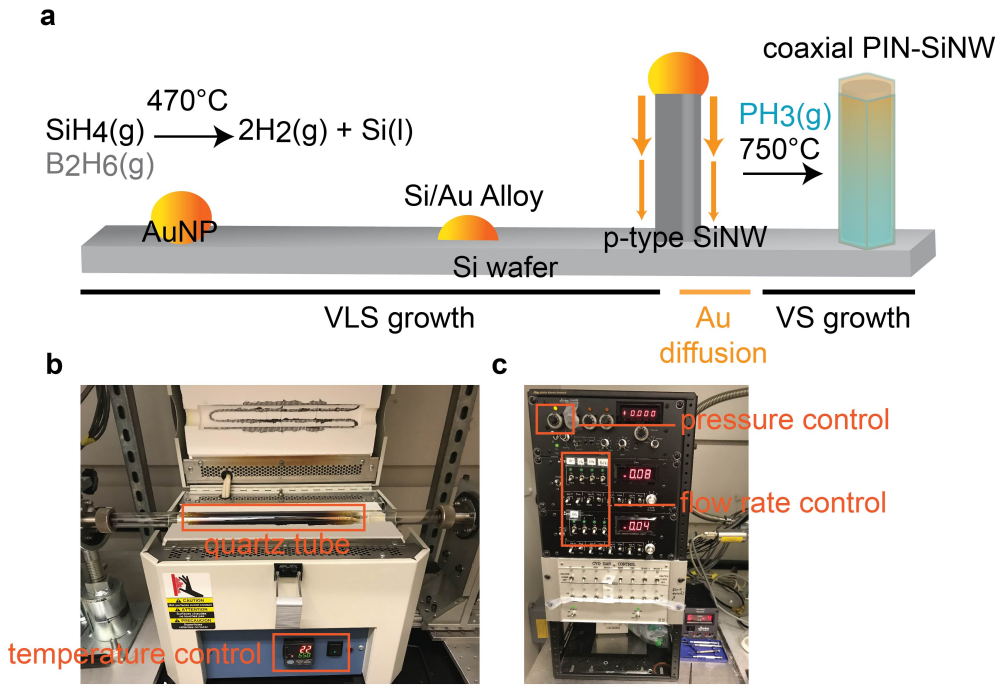

Figure 2.7. PIN-SiNW growth occurs via a vapor liquid solid and vapor solid growth mechanism. (a) Silicon nanowire growth occurs via a vapor liquid solid growth mechanism in which a Si wafer is plated with Au nanoparticles and silane gas is **(b-c)** Silicon nanowires are grown in a home-built chemical vapor deposition system in the Tian lab consisting of a furnace with a quartz tube serving as the growth chamber (b) and a panel for controlling flow rate of the reactant gases and pressure (c).

Coaxial pin silicon nanowires (PIN-SiNWs) were synthesized using a gold (Au) nanocluster-catalyzed chemical vapor deposition (CVD) process (Fig. 11a-c). Citrate-stabilized Au colloidal nanoparticles (Ted Pella Inc. 50 nm diameter) were deposited onto silicon (Si) <100 > substrates (Nova Electronic Materials, n-type, 0.001-0.005 Ωcm) and used as catalysts. During the nanowire growth, silane (SiH_4) was used as the Si reactant, diboron (B_2H_6, 100 ppm in H_2) as the p-type dopant, phosphine (PH_3, 1000

ppm in H_2) as the n-type dopant, and hydrogen (H_2) as the carrier gas. For the p-type core nanowire growth, SiH_4, B_2H_6, and H_2 were delivered at flow rates of 2, 10, and 60 standard cubic centimeters per minute (sccm), respectively (Fig. 11a). For the intrinsic Si shell (i-shell) deposition, SiH_4 and H_2 were delivered at 0.3 and 60 sccm, respectively (Fig. 11a). Flow of PH_3 gas was then added for the n-type outer shell deposition at a flow rate of 1.5 sccm (Fig. 11a). The core growth was carried out at 470°C at a pressure of 40 torr for 30 min (Fig. 11a). Prior to i-shell deposition, growth was paused in a vacuum for 20 minutes until the CVD furnace temperature was stabilized at 750°C in preparation for shell deposition (Fig. 11a). The shell depositions were performed at 750°C at a pressure of 20 torr for 15 min per shell (Fig. 11a).

P-doped Si nanowires (p-type SiNWs) were synthesized also using 250 nm Au nanocluster-catalyzed CVD. SiH_4, B_2H_6, and H_2 were delivered at flow rates of 2, 10, and 60 sccm, respectively, at 470°C at a pressure of 40 torr for 30 min.

Undoped Si nanowires were synthesized also using 250 nm Au nanocluster-catalyzed CVD. SiH_4 and H_2 were delivered at flow rates of 2 and 60 sccm, respectively, at 475°C at a pressure of 40 torr for 30 min.

P-doped Au diffused Si nanowires were synthesized also using 250 nm Au nanocluster-catalyzed CVD. SiH_4, B_2H_6, and H_2 were delivered at flow rates of 2, 10, and 60 sccm, respectively, at 470°C at a pressure of 40 torr for 30 min. Au catalyst was allowed to diffuse down the synthesized nanowires in a vacuum at 750°C for 30 min.

2.5.2 X-ray photoelectron spectroscopy

PIN-SiNWs still attached to their growth substrate were cleaned in 10% HF for 90 sec, rinsed in DI H_2O for 30 sec, and dried with N_2 gas. X-ray photoelectron

spectroscopy (XPS) was performed on the nanowire samples using a monochromatic Al Kα X-ray source (AXIS Nova Kratos Analytical) that probes elemental composition 7-10 nm from the surface of the sample. The Al anode was powered at 10 mA and 15 kV. The instrument work function was calibrated to give an Au $4f_{7/2}$ metallic gold binding energy (BE) of 83.95 eV. Instrument base pressure was *ca*. 1×10^{-9} Torr. The analysis area size was 0.3 x 0.7 mm^2. For calibration purposes, the binding energies were referenced to Si 2p peak at 99.8 eV and/or C 1s peak at 285.5 eV. To improve reliability of the calibration, Pt metal was also introduced to the surface of some samples and Pt 4f signal 71.0 eV was used for cross-checking the calibration. Survey spectra were collected with a step size of 1 eV and 160 eV pass energy. The high-resolution spectra of Si 2p and Au 4f were collected with a pass energy of 20 eV and 0.1 eV step size using 3 and 20 sweeps of 120 s for each sweep, respectively. XPS peaks were fitted with an asymmetric Gaussian/Lorentzian peak shape with linear background correction. Initial peak approximation model was based on the Au 4f peak modeling of the pure gold sample in order to better evaluate the asymmetric nature of the peak profile and the fit envelope.

2.5.3 Transmission electron microscopy

PIN-SiNWs synthesized from 50 nm AuNPs were sonicated off of their growth substrate in IPA, and then drop casted onto copper grids (Ted Pella Inc., USA, Lacey Formvar/Carbon, 200 mesh) for transmission electron microscopy (TEM) (FEI, USA, Tecnai F30) and for high-angle annular dark field (HAADF) scanning transmission electron microscopy (STEM). STEM images were recorded using an aberration corrected STEM (JEOL, Japan, JEM-ARM200CF).

2.5.4 Energy Dispersive X-ray Spectroscopy

PIN-SiNWs synthesized from 50 nm AuNPs were sonicated off of their growth substrate in IPA, and then dropcasted onto copper grids (Ted Pella Inc., USA, Lacey Formvar/Carbon, 200 mesh) for TEM (JEOL, Japan, JEM-3010) energy dispersive x-ray spectroscopy (EDS) (Thermo Fisher Scientific, USA, Thermo Noran Vantage XEDS). 840 second EDS measurements were taken for each nanowire and elemental peaks were assigned.

2.5.5 Atom probe tomography (APT)

200-350 nm PIN-SiNW were synthesized from 50 nm AuNPs and coated with 50 nm of Ni layers using an e-beam evaporator (AJA International, USA). The Ni-protected SiNWs were transferred onto Si microposts using a micromanipulator inside a focused ion beam (FIB) system (FEI, USA, Nova 600 NanoLab). Samples were then milled and sharpened into needle-like microtip specimens for APT characterization. The APT was run in an ultraviolet (UV) laser-assisted local-electrode atom-probe instrument (Cameca, USA, LEAP 400XSi). The surface atoms from each microtip were evaporated with an applied voltage of 1-6 kV and 20 pJ of 355 nm UV laser pulsing at a frequency of 250 kHz. The mass-to-charge (m/z) ratios of individual evaporated ions and their corresponding (x, y, z) coordinates in space were recorded with a position sensitive detector. The samples were held at 30 K and 2×10^{-11} Torr during APT experiments. The 3D reconstructions and data analyses were performed using Cameca's Integrated Visualization and Analysis Software (IVAS) 3.6 code. The proximity histogram was created with respect to the 80% Si isoconcentration surface.

2.6 References

1. Famm, K., Litt, B., Tracey, K. J., Boyden, E. S. & Slaoui, M. A jump-start for electroceuticals. *Nature* **496**, 159-161 (2013).
2. Vetter, R. J., Williams, J. C., Hetke, J. F., Nunamaker, E. A. & Kipke, D. R. Chronic neural recording using silicon-substrate microelectrode arrays implanted in cerebral cortex. *IEEE Transactions on Biomedical Engineering* **51**, 896-904 (2004).
3. Zhou, W., Dai, X. C. & Lieber, C. M. Advances in nanowire bioelectronics. *Reports on Progress in Physics* **80**, doi:10.1088/0034-4885/80/1/016701 (2017).
4. Ghezzi, D. *et al.* A hybrid bioorganic interface for neuronal photoactivation. *Nature Communications* **2**, doi:10.1038/ncomms1164 (2011).
5. Ghezzi, D. *et al.* A polymer optoelectronic interface restores light sensitivity in blind rat retinas. *Nature Photonics* **7**, 400-406 (2013).
6. Mathieson, K. *et al.* Photovoltaic retinal prosthesis with high pixel density. *Nature Photonics* **6**, 391-397 (2012).
7. Carvalho-de-Souza, J. L. *et al.* Photosensitivity of neurons enabled by cell-targeted gold nanoparticles. *Neuron* **86**, 207-217 (2015).
8. Jiang, Y. W. *et al.* Heterogeneous silicon rnesostructures for lipid-supported bioelectric interfaces. *Nature Materials* **15**, 1023-1030 (2016).
9. Packer, A. M., Roska, B. & Hausser, M. Targeting neurons and photons for optogenetics. *Nature Neuroscience* **16**, 805-815 (2013).
10. Boyden, E. S., Zhang, F., Bamberg, E., Nagel, G. & Deisseroth, K. Millisecond-timescale, genetically targeted optical control of neural activity. *Nature Neuroscience* **8**, 1263-1268 (2005).
11. Zimmerman, J., Parameswaran, R. & Tian, B. Z. Nanoscale semiconductor devices as new biomaterials. *Biomaterials Science* **2**, 619-626 (2014).
12. Rogers, J. A., Someya, T. & Huang, Y. G. Materials and mechanics for stretchable electronics. *Science* **327**, 1603-1607 (2010).
13. Hwang, S. W. *et al.* A Physically Transient Form of Silicon Electronics. *Science* **337**, 1640-1644 (2012).
14. Straub, B., Meyer, E. & Fromherz, P. Recombinant maxi-K channels on transistor, a prototype of iono-electronic interfacing. *Nature Biotechnology* **19**, 121-124 (2001).
15. Chiappini, C. *et al.* Biodegradable silicon nanoneedles delivering nucleic acids intracellularly induce localized in vivo neovascularization. *Nature Materials* **14**, 532-539 (2015).
16. Priolo, F., Gregorkiewicz, T., Galli, M. & Krauss, T. F. Silicon nanostructures for photonics and photovoltaics. *Nature Nanotechnology* **9**, 19-32 (2014).
17. Xie, P., Xiong, Q. H., Fang, Y., Qing, Q. & Lieber, C. M. Local electrical potential detection of DNA by nanowire-nanopore sensors. *Nature Nanotechnology* **7**, 119-125 (2012).
18. Yan, R. X. *et al. Nature Nanotechnology* **7**, 191-196 (2012).
19. Zimmerman, J. F. *et al.* Cellular uptake and dynamics of unlabeled freestanding silicon nanowires. *Science Advances* **2**, doi:10.1126/sciadv.1601039 (2016).

20. Zhang, A. Q. & Lieber, C. M. Nano-Bioelectronics. *Chemical Reviews* **116**, 215-257 (2016).
21. Tian, B. Z. *et al.* Coaxial silicon nanowires as solar cells and nanoelectronic power sources. *Nature* **449**, 885-888 (2007).
22. Su, Y. D. *et al.* Single-nanowire photoelectrochemistry. *Nature Nanotechnology* **11**, 609-612 (2016).
23. Hannon, J. B., Kodambaka, S., Ross, F. M. & Tromp, R. M. The influence of the surface migration of gold on the growth of silicon nanowires. *Nature* **440**, 69-71 (2006).
24. Luo, Z. Q. *et al.* Atomic gold-enabled three-dimensional lithography for silicon mesostructures. *Science* **348**, 1451-1455 (2015).
25. Seibt, M. *et al.* Gettering in silicon photovoltaics: current state and future perspectives. *Physica Status Solidi a-Applications and Materials Science* **203**, 696-713 (2006).
26. Yuan, G. B. *et al.* Understanding the origin of the low performance of chemically grown silicon nanowires for solar energy conversion. *Angewandte Chemie-International Edition* **50**, 2334-2338 (2011).
27. Kim, S. K. *et al.* Tuning light absorption in core/shell silicon nanowire photovoltaic devices through morphological design. *Nano Letters* **12**, 4971-4976 (2012).
28. Garnett, E. C. *et al.* Dopant profiling and surface analysis of silicon nanowires using capacitance-voltage measurements. *Nature Nanotechnology* **4**, 311-314 (2009).
29. Liu, Z. *et al.* Anomalous high capacitance in a coaxial single nanowire capacitor. *Nature Communications* **3**, doi:10.1038/ncomms1833 (2012).
30. Vogel, E. M. Technology and metrology of new electronic materials and devices. *Nature Nanotechnology* **2**, 25-32 (2007).
31. Parameswaran, R. *et al.* Photoelectrochemical modulation of neuronal activity with free-standing coaxial silicon nanowires. *Nature Nanotechnology* **13**, 260-266 (2018).

Chapter 3. Photoelectrochemical modulation of neuronal activity with free-standing PIN-SiNWs

3.1 Introduction

Extracellular electrical stimulation of excitable cells is the basis for many implantable devices that treat a variety of diseases[1]. While these devices have been efficacious, they are often limited by their bulkiness, mechanical invasiveness, and inability to target single cells[2,3]. Thus, researchers have looked to optical stimulation techniques, where organic or inorganic photodiode substrates, such as silicon photodiode arrays and conductive polymers, are used for photovoltaic neuronal stimulation[4-6]; however, these tools cannot be easily administered in a drug-like fashion. While some photothermally-modulating materials, like gold nanorods and mesoporous Si particles, meet these criteria[7,8], chronic cellular effects due to heat from such devices are unknown. Optogenetics has been promising for addressing these issues, but fundamentally requires genetic modifications[9,10], which can be difficult to implement *in vivo*. As a result, there is still a need for exploring a non-genetic approach that can be administered in a drug-like fashion. Here, we use coaxial PIN-SiNWs to wirelessly and photoelectrochemically modulate primary rat dorsal root ganglion neuron excitability.

3.2 Basic coaxial nanowire/neuron interfaces

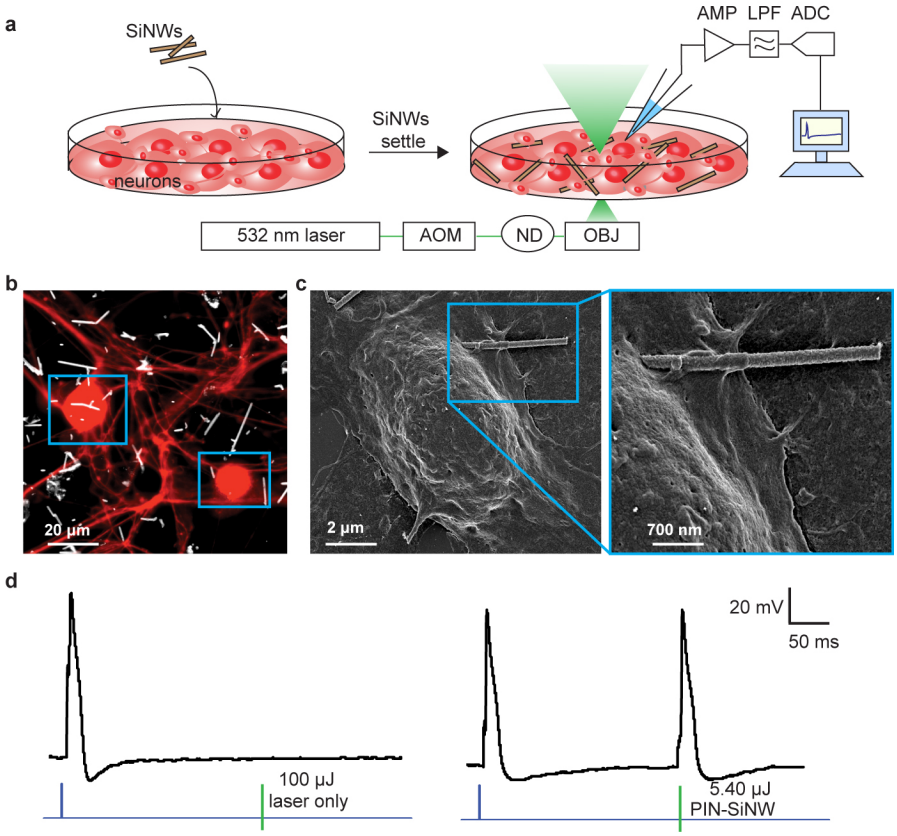

Figure 3.1. Basic silicon nanowire-based neural interfaces. (a) Schematic of the set-up used to record DRG neuron APs in response to a 532 nm laser stimulation at a single neuron/SiNW interface. This set-up includes an ordinary electrophysiology capability for patch clamp experiments, with an amplifier (AMP), used in current clamp mode, a low pass filter (LPF), and an analog to digital converter (ADC). In addition the setup was implemented with a 532 nm laser beam controlled by an acoustic modulator (AOM) and various neutral density (ND) filters (to attenuate the power). The laser beam is aligned to the optical central axis of the objective lens (OBJ) of an inverted microscope. SiNWs were sonicated off of their growth substrate and drop casted onto the primary neuron culture. After 20 min of settling, the experiments were performed. **(b)** Confocal microscopy image of primary neonatal rat dorsal root ganglion (DRG) neurons stained with anti-β-tubulin III (red) co-cultured with PIN-SiNWs (white). This is a representative image from one of a total of 10 images taken from 2 independent experiments. **(c)** Scanning electron microscopy images of a single DRG neuron interacting with a single PIN-SiNW (left); zoomed in image displaying neuron-PIN-SiNW interface (right). This is a representative image from one of a total of 63 images taken from 4 independent experiments. **(d)** Patch clamp electrophysiology current clamp trace of membrane voltage in DRG neuron stimulated (blue pulse) or a laser pulse (green bar) of various energies as labeled at the neuron/SiNW interface. Two conditions are displayed: laser only with no SiNW (left) and PIN-SiNW (right). These are representative

(Figure 3.1 continued) traces from one of 173 total action potential traces measured from 30 neurons with PIN-SiNWs, and one of 27 total traces from 2 neurons with PIN-SiNWs. Adapted with permission from ref (19).

We drop-casted PIN-SiNWs onto primary dorsal root ganglion (DRG) neurons cultured from neonatal rats (Fig. 3.1a-b). Scanning electron microscopy (SEM) shows that PIN-SiNWs form close interactions with neuronal membranes without being internalized into cells (Fig. 3.1c). We hypothesized that the photocathodic electrochemical effect produced from a single nanowire could cause membrane depolarization (by reducing the potential in a local extracellular region) and trigger action potentials (APs). We aligned a neuron/PIN-SiNW interface to a 532 nm laser spot, and used a whole cell current clamp set-up to record the neuronal membrane voltage before, during and after laser stimulation (Fig. 3.1a). We found that laser stimulation at the neuron/PIN-SiNW

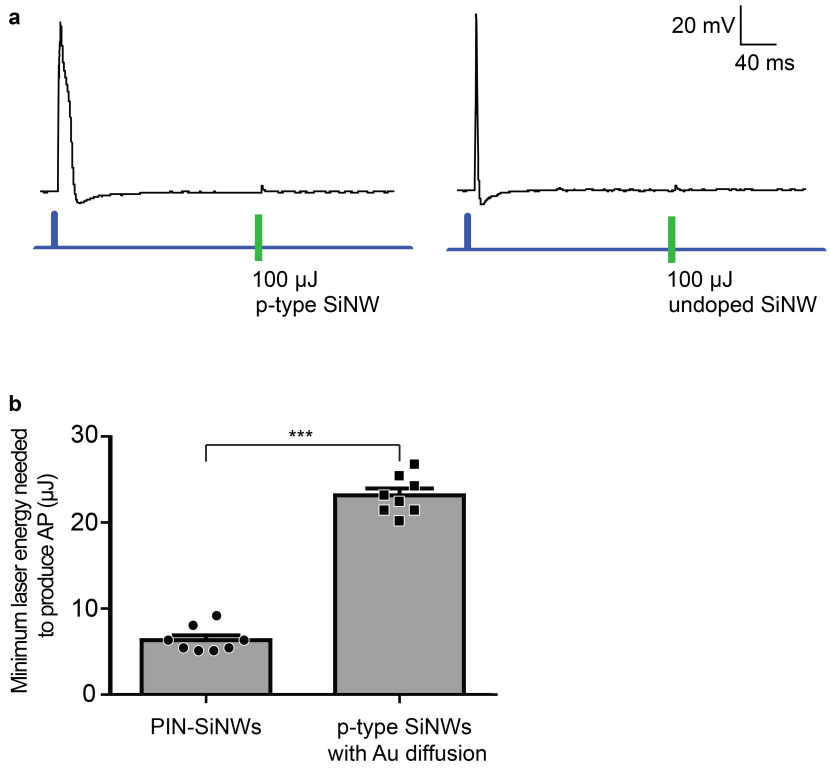

Fig 3.2. Comparison of optical modulation of neuronal cell excitability with PIN-SiNWs, undoped SiNWs, p-type SiNWs, and p-type SiNWs with Au diffusion. (a)

(Figure 3.2 continued) Patch clamp electrophysiology current clamp trace of membrane voltage in DRG neuron stimulated (blue pulse) or a laser pulse (green bar) of various energies as labeled at the neuron-SiNW interface. **(b)** Average minimum laser energy necessary for PIN-SiNWs and p-type SiNWs with Au diffusion to generate APs in DRG neurons (N = 6 biological replicates for each condition with a total of 8 technical replicates for each). Individual data points are indicated by the black circles (PIN-SiNWs) or black squares (p-type SiNWs with Au diffusion). Paired t-test performed to determine statistical significance. Error bars represent the standard error about the mean. *p* value: ***, < 0.0001. Adapted with permission from ref (19).

interface can elicit APs in neurons at an average minimum laser energy of 6.44 μJ for laser pulse durations ranging from 0.5 ms to 5 ms (Fig. 3.1d and Fig. 3.2). This laser energy is similar to or less than that required for other photothermally stimulating materials to elicit APs in neurons[7,8], even though the direct cell contact area is at least 10 times smaller in the present case. Additionally, the same minimal energy necessary to trigger APs at several stimulating pulse durations suggests that the PIN-SiNW mimicks a classic external stimulation electrode without the mechanical invasiveness and bulkiness inherent to physical electrodes [11]. Control experiments using pure p-type and undoped SiNWs were unable to elicit APs, and only produced sub-threshold depolarizations upon laser stimulation, even at high energies of 100 μJ and 1 ms durations (Fig. 3.2). In the absence of a NW, laser stimulation with an energy of up to 100 μJ at 1 ms laser pulse durations cannot depolarize the cell's membrane (Fig. 3.1d).

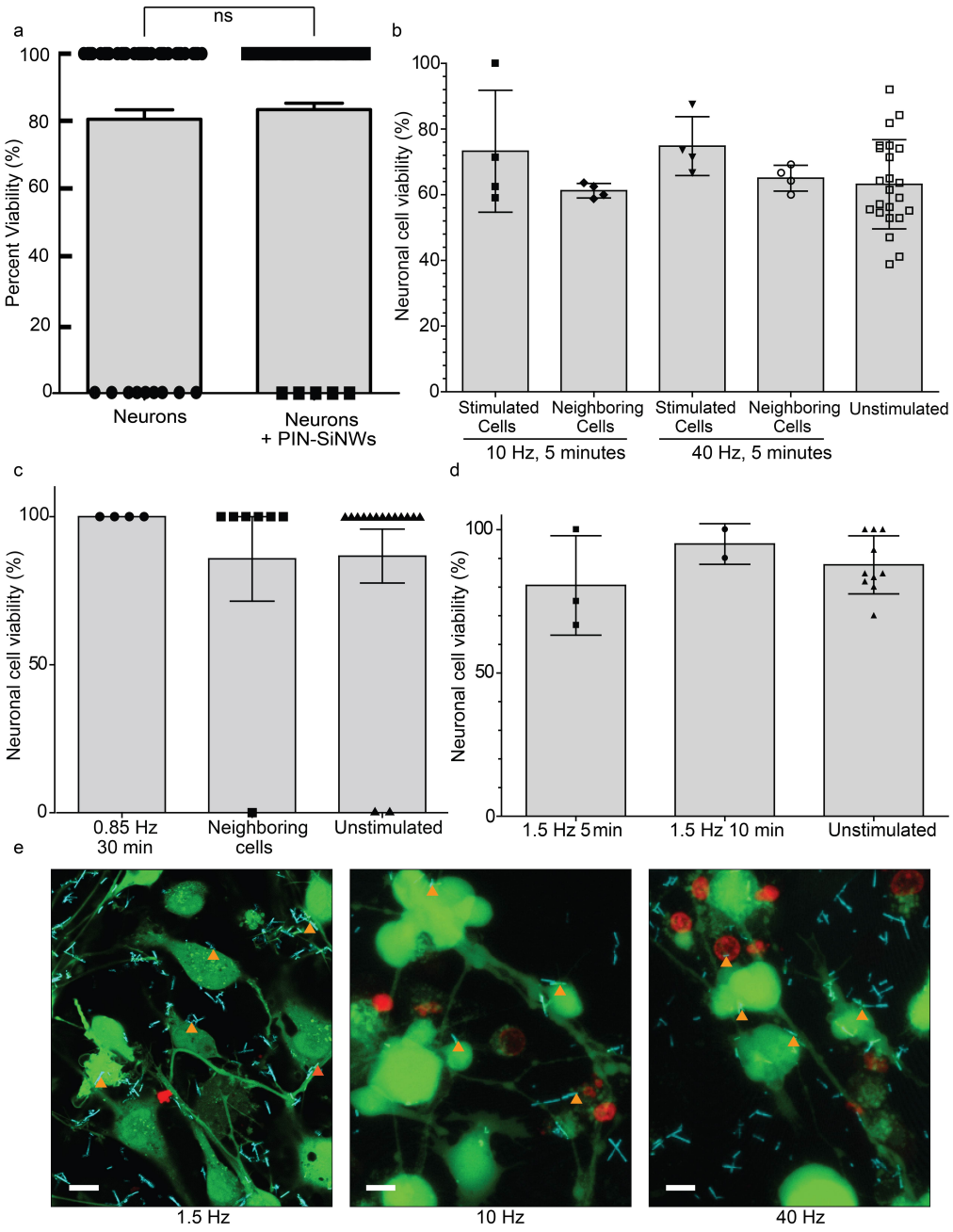

Figure 3.3. PIN-SiNWs do not induce significant cytotoxicity in primary DRG neurons with and without laser illumination. (a) Neuronal cell viability was measured by treating each cell assayed as a data point with the option of either being live (100% viability) or dead (0% viability), as indicated by green (live) or red (dead) staining in the live/dead assay. Percentage of viable neurons 24 hours after initial culture with and without PIN-SiNWs (N = 42 neurons for each condition). Each circle (neurons) and square (neurons + PIN-SiNWs) represents one data point. Paired t-test was performed to determine statistical significance. **ns** = not significant. **(b)** Neuronal cell viability was

(Figure 3.3 continued) measured by calculating the percentage of viable neurons in each of several experiments performed. Each data point depicted represents the percentage of neuronal viability from each experiment performed. Percentage of viable neurons after 40 Hz (N = 41 stimulated neurons and N = 75 neighboring neurons from 4 experiments performed (black triangles and open circles, respectively)) and 10 Hz (N = 43 stimulated neurons and N = 77 neighboring neurons from four experiments performed (black squares and black circles, respectively)) 592 nm laser illumination at PIN-SiNW-neuron interfaces for 5 min durations. Viability of stimulated neurons, neighboring neurons, and completely unstimulated neurons (N = 498 unstimulated neurons from 23 experiments performed (open squares)) were assessed. **(c)** Neuronal cell viability was measured by treating each cell assayed as a data point with the option of either being live (100% viability) or dead (0% viability), as indicated by green (live) or red (dead) staining in the live/dead assay. Percentage of viable neurons after 0.85 Hz (N = 4 stimulated neurons, 7 neighboring neurons, and N = 16 unstimulated neurons) 592 nm laser illumination at PIN-SiNW-neuron interfaces for 30 min durations. Individual data points for the 0.85 Hz stimulated neurons (black circles), neighboring neurons (black squares), and unstimulated neurons (black triangles) are indicated. Viability of stimulated neurons, neighboring neurons, and completely unstimulated neurons were assessed. **(d)** Neuronal cell viability was measured by calculating the percentage of viable neurons in each of several experiments performed. Each data point depicted represents the percentage of neuronal viability from each experiment performed. Percentage of viable neurons after 1.5 Hz 592 nm laser illumination at PIN-SiNW-neuron interfaces for 5 (N = 16 stimulated neurons from 3 experiments performed (black squares)), and 10 min (N = 15 stimulated neurons from 2 experiments performed (black circles)) durations. Viability of stimulated neurons, and completely unstimulated neurons (N = 28 unstimulated neurons from 10 experiments performed (black triangles)) were assessed. All error bars in this figure represent the standard error about the average. **(e)** Live/Dead images taken on the SP5 Leica confocal microscope after 592 nm laser stimulation for 5 min at 1.5 Hz, 10 Hz, and 40 Hz (left to right). Live cells (green); Dead cells (red); PIN-SiNWs (blue); laser stimulated neuron-PIN-SiNW interfaces (orange arrows). Scale bars, 10 μm. Adapted with permission from ref (19).

We also confirmed via a live-dead cell viability assay that the presence of PIN-SiNWs in the neuron culture had a negligible effect on cell viability and that laser stimulation on the time scales explored here also had a negligible effect on cell viability (Fig. 3.3).

3.3 Systematic neuromodulation studies

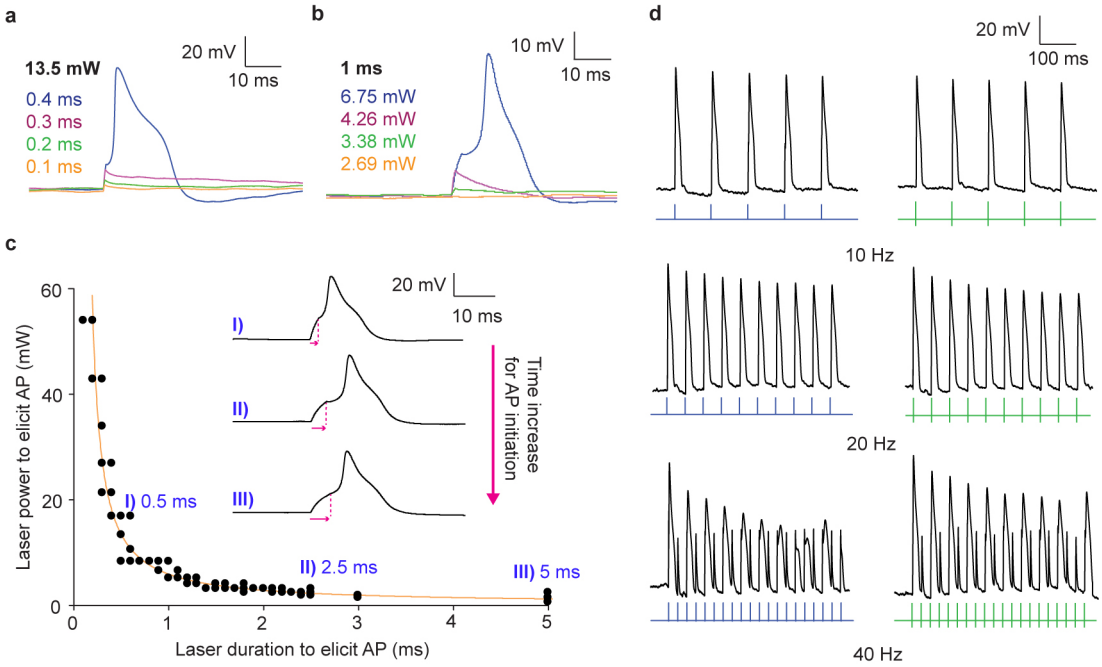

Figure 3.4. Photocurrent generated by coaxial nanowires can be harnessed to elicit action potentials in primary rat dorsal root ganglion neurons. (a and b) Patch clamp electrophysiology current clamp traces of membrane voltage in DRG neurons illuminated by a 532 nm laser pulse at the neuron/PIN-SiNW interface at **(a)** 13.5 mW with durations of 0.1 ms (orange), 0.2 ms (green), 0.3 ms (pink), and 0.4 ms (blue) and **(b)** 2.69 mW (orange), 3.38 mW (green), 4.26 mW (pink), and 6.75 mW (blue) for 1 ms. These traces in **(a)** and **(b)** are representative traces from one of a total of 1398 traces from 30 independent neurons, many of which are sub-threshold depolarizations at various laser powers and durations. 173 traces out of the 1398 represent action potentials. **(c)** Excitability curve displaying 532 nm laser power and duration combinations that produce APs in neurons (N=6 neurons; total of N=78 replicates) interacting with a single PIN-SiNWs with specific traces and time to peak response for each of those traces (pink arrows) at I) 0.5 ms, II) 2.5 ms, and III) 5 ms durations highlighted. Error bars represent the standard error about the average. Some of the data points are overlaid. **(d)** AP traces from neurons interacting with single PIN-SiNWs pulsed at 10, 20 and 40 Hz with light (green bars) and injected current from patch amplifier (blue pulses). These are representative traces from a total of 6 pulse train traces for each frequency taken from 3 independent neurons. Adapted with permission from ref (19).

We further studied PIN-SiNW enabled neuron excitation by altering the laser power and pulse duration. At a laser power of 13.5 mW, we were able to produce sub-threshold depolarizations at increasing durations of 0.1, 0.2, and 0.3 ms, respectively

(Fig. 3.4a). At a laser duration of 0.4 ms and energy of 5.4 µJ, an AP was generated (Fig. 3.4a). Keeping the stimulus duration constant at 1 ms, we were able to passively depolarize the membrane at increasing laser powers until reaching 6.75 mW and a total energy of 5.95 µJ, at which an AP was generated in the cell (Fig. 3.4b). We then constructed an excitability curve and found that as the duration of the laser stimulus increased, the amount of laser power required to generate an AP decreased (Fig. 3.4c).

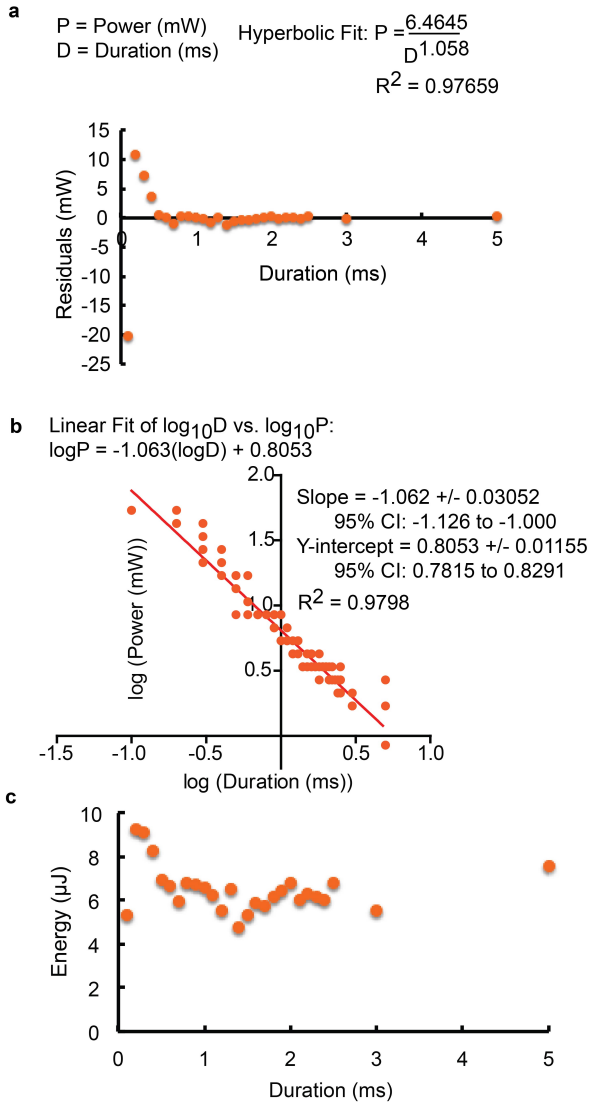

Figure 3.5. Excitability curve is hyperbolic and the minimal total energy to trigger APs is independent of pulse duration. (a) Residual plot illustrating the goodness of fit

(Figure 3.5 continued) of the hyperbolic fit curve (equation displayed above) to the data. **(b)** Log D vs Log P plot with linear fit. Some of the data points are overlaid. **(c)** Minimum laser pulse energy necessary to trigger an AP using a PIN-SiNW plotted as a function of laser pulse duration. Adapted with permission from ref (19).

We fit the data to a hyperbolic function and found that the minimum total energy required to trigger an AP is independent of the pulse duration, as would be expected for current injecting electrodes [11] (Fig. 3.5). This phenomenon can both be seen by directly plotting minimum total energy as a function of the laser pulse duration, as well as by the exponent in the denominator of the hyperbolic function, which is close to 1 (Fig. 3.5). The rheobase of the fitted curve is 1.178 mW and chronaxie 2.597 ms, which compares well to literature chronaxie values for DRG neurons [11] (Fig. 3.4c). We also found that with increasing laser pulse durations, the time to AP initiation was increased (Fig. 3.4c). These results together demonstrate that PIN-SiNWs can elicit APs in a manner that is physiologically indistinguishable from those induced by classical external current injecting electrodes.

We also pulsed the laser at varying frequencies at the neuron/PIN-SiNW interface and assessed the cellular response. We found that neurons are able to generate trains of APs at 10 and 20 Hz both with injected current and laser stimulation (Fig. 3.4d). At 40 Hz, the cell depicted failed to produce APs in response to every pulse of laser light or injected current (Fig. 3.4d). This neuron produced 10 APs in the case of the light stimulation and 9 in the case of the injected current out of 20 pulses at 40 Hz (Fig. 3.4d). At the lowest frequency that neurons begin to fail to generate one AP for

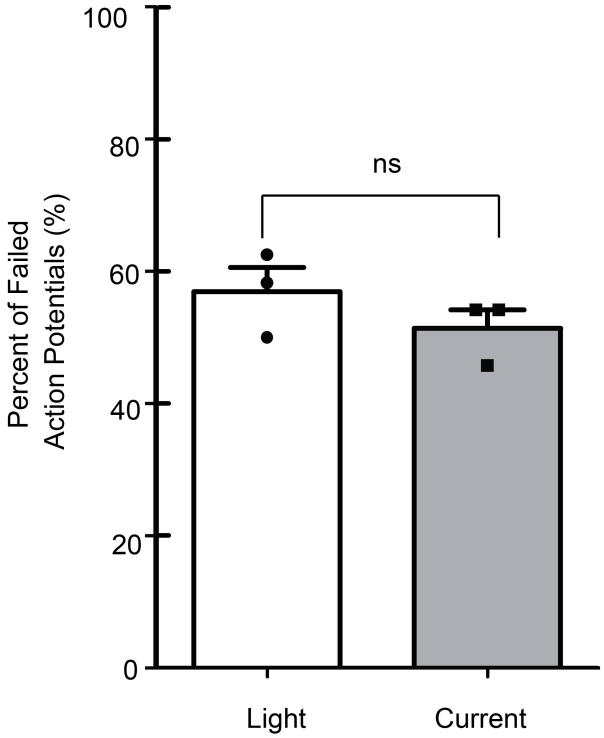

Figure 3.6. APs from pulse train stimulations fail at the same rate upon light stimulation of the PIN-SiNW interface and injected current. Graph comparing the percentage of failed APs at the lowest frequency that the neuron begins to fail to generate 1 AP per pulse of current or light from three neurons. Individual data points are indicated with black circles (Light) and squares (Current). A paired t-test was used to determine statistical significance. **ns** = not significant. Error bars represent the standard error about the mean. Adapted with permission from ref (19).

every pulse of current or light, the percentage of failed APs tended to be the same when comparing the two stimuli (Fig. 3.6). These results indicate that APs produced in neurons through PIN-SiNW-enabled optical stimulation are physiologically representative and follow the intrinsic limitation of the cell to fire trains of APs above a specific frequency.

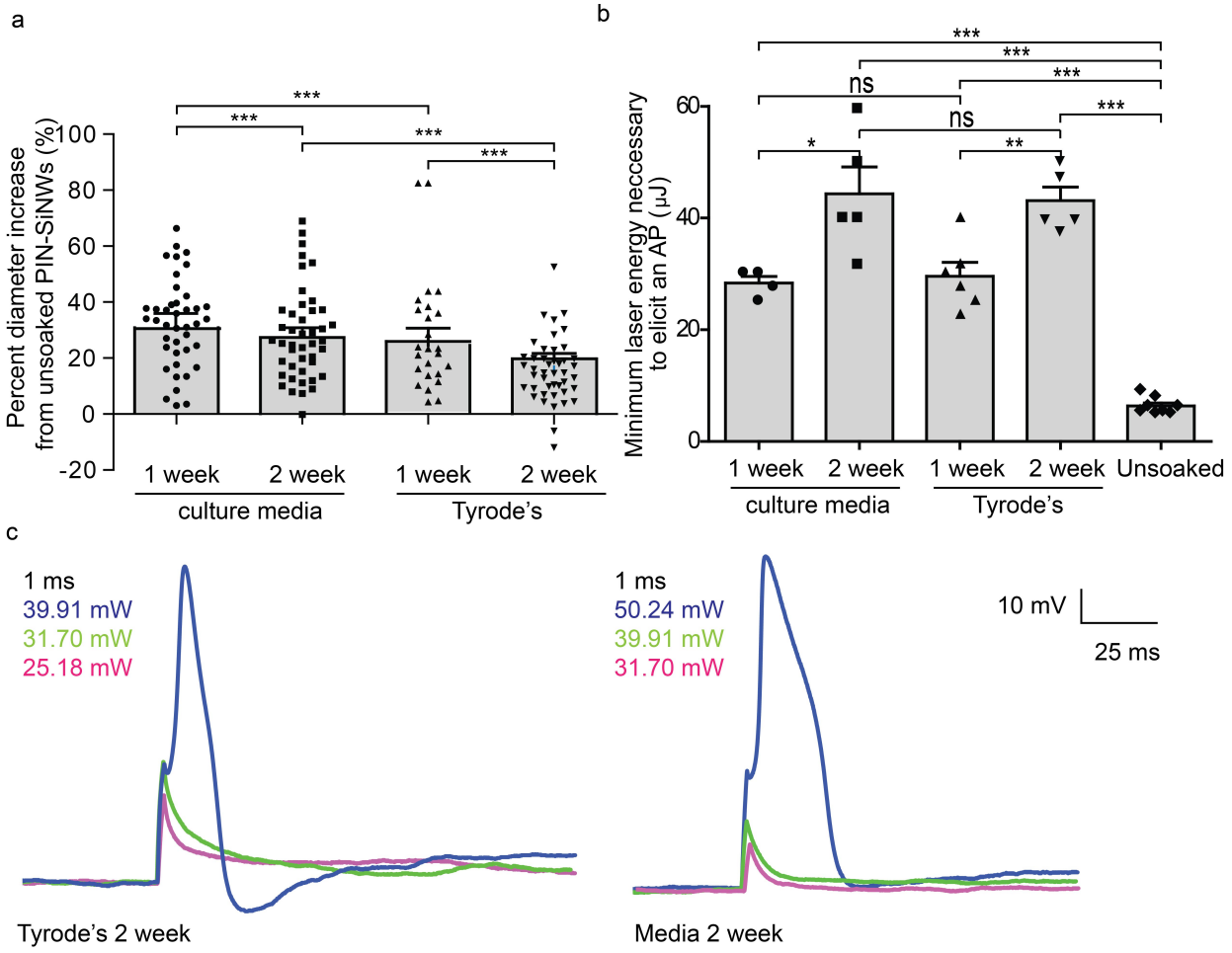

Figure 3.7. PIN-SiNWs soaked in Tyrode's buffer or culture media for 1-2 weeks are less efficient at triggering APs in neurons. (a) Graph comparing the percent increase in diameter of PIN-SiNWs under the various soaking conditions. We observed these NWs via SEM and found that PIN-SiNWs soaked in media for 1 and 2 weeks experienced a 32.36%+/-3.85% and 28.37%+/-3.58% increase in diameter, respectively, as compared to an average diameter from 109 unsoaked NWs (N = 41, 1 week (circles); N = 44, 2 week (squares)). Those NWs soaked in Tyrode's buffer for 1 and 2 weeks experienced a 28.02%+/-4.44% and 15.76%+/-1.51% increase in diameter, respectively, as compared to unsoaked NWs (N = 25, 1 week (triangles); N = 45, 2 week (inverted triangles)). It is possible that this increase in diameter in the first week is a result of oxidization/hydration-induced swelling and formation of a protein corona around NWs in media. The 2-week time point for both conditions showed a decrease in diameter from that of the 1-week, indicating a subsequent degradation process. **(b)** Graph comparing the minimum laser energy threshold necessary for PIN-

(Figure 3.7 continued) SiNWs under various conditions to elicit APs in neurons. Individual data points are indicated with black circles (N =4, 1 week media), squares (N=5, 2 week media), triangles (N=6, 1 week Tyrode's), inverted triangles (N=5, 2 week Tyrode's), and diamonds (N=8, unsoaked). Paired t-tests were used to determine statistical significance in (**a**) and (**b**). **ns** = not significant. All error bars in this figure represent the standard error about the mean. **(c)** Patch clamp electrophysiology current clamp traces of membrane voltage in DRG neurons illuminated by a 532 nm laser pulse (1 ms duration) at the neuron-PIN-SiNW interface. The NWs were soaked in Tyrode's and media for 2 weeks. *p* values: *, < 0.05; **, < 0.01; ***, < 0.0001. Adapted with permission from ref (19).

To understand how effectively the PIN-SiNWs would be able to perform neuromodulation when not used fresh, we incubated PIN-SiNWs in culture media or Tyrode's buffer for 1- and 2-week time points and used them to trigger APs in primary rat DRG neurons. The minimum laser energy threshold necessary to elicit APs increased from the previously observed 6.44 μJ to an average of 28.33 μJ and 29.58 μJ for the 1-week time point in media and Tyrode's respectively, and 44.30 μJ and 43.10 μJ for the 2-week time point in media and Tyrode's respectively (Fig. 3.7). We propose that the increased laser energy threshold is caused by oxidation/hydration induced degradation of both the Si heterojunction and atomic Au activity.

3.4 Probing of the neuromodulation mechanism

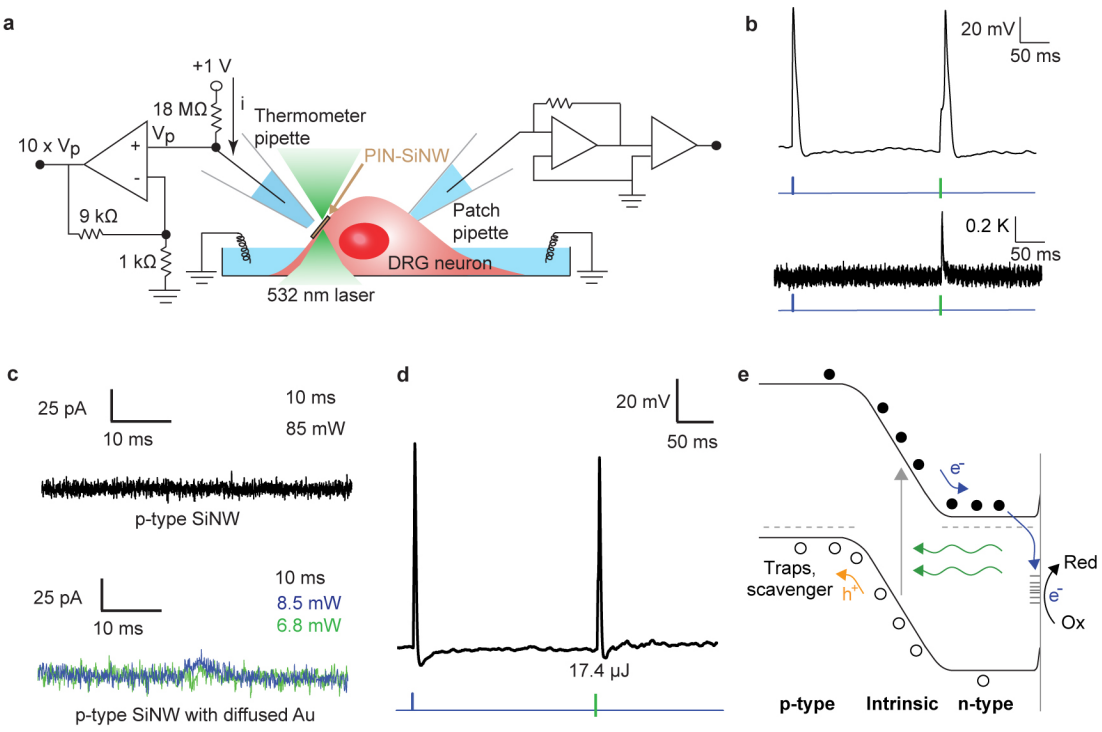

Figure 3.8. The mechanism of coaxial nanowire photocurrent generation and neuronal modulation is primarily photoelectrochemical, aided by surface atomic Au. (**a**) Schematic of temperature measurement setup for simultaneous measurement of temperature and neuronal APs produced by laser stimulation or injected current through patch amplifier. **(b)** Patch clamp electrophysiology current clamp trace of membrane voltage (top) in DRG neuron stimulated by injected current (blue pulse) and illuminated by a 532 nm laser pulse at the neuron-PIN-SiNW interface (green bar). Corresponding temperature measurement (bottom) taken 2 µm away from neuron/PIN-SiNW interface produced by calibrating the thermometer pipette resistance with temperature changes. This is a representative temperature measurement from one of 18 total traces from 3 independent neurons. **(c)** Photocurrent measurement taken from a single p-type SiNW illuminated with 532 nm laser light for 10 ms at a laser illumination power of 85 mW (top). This is a representative trace from one of a total of 71 traces measured from 4 independent p-type SiNWs. Photocurrent measurement taken from a p-type SiNW with diffused Au for 10 ms at laser illumination powers of 8.5 mW (blue) and 6.8 mW (green). These are representative traces from a total of 52 traces measured from 6 independent p-type SiNWs with diffused Au. **(d)** Patch clamp electrophysiology current clamp trace of membrane voltage (top) in DRG neuron stimulated by injected current (blue pulse) and illuminated by a 1 ms 17.4 µJ 532 nm laser pulse at the neuron-p-type SiNW with diffused Au interface (green bar). This is a representative trace from one of a total of 40 traces measured from 5 independent neurons. **(e)** Band diagram representing the redox reaction that occurs at the interface between the PIN-SiNW and the electrolyte solution. Kinetic barrier for the

(Figure 3.8 continued) photoelectrochemical reaction is lowered by the presence of atomic Au. Adapted with permission from ref (19).

Having demonstrated the optical modulation of single primary neuron excitability with PIN-SiNWs, we next further studied the mechanism of this stimulation. Previous work has demonstrated that mesoporous silicon materials can elicit APs in neurons via a photothermal effect[8]. Thus, we wanted to understand the contribution of photothermal current generation to PIN-SiNW-enabled neuromodulation. We used a calibrated

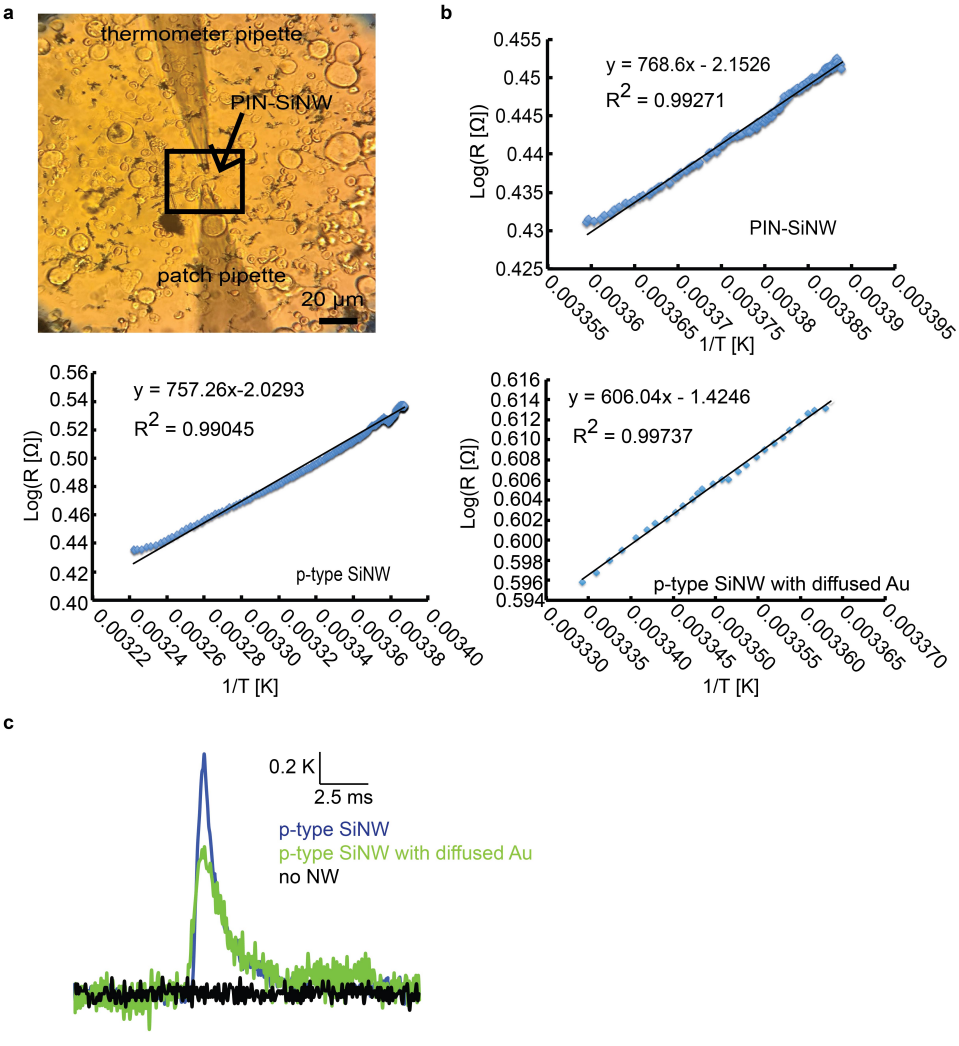

Figure 3.9. Photothermal effect can be pronounced at higher illumination energy. **(a)** Brightfield image of a neuron during a simultaneous membrane voltage and temperature recording experiment. Thermometer pipette is positioned within ~ 2 µm of

(Figure 3.9 continued) the neuron/PIN-SiNW interface. Neuron is current clamped by a patch pipette from the other side. **(b)** Calibration curves demonstrating the relationship between the thermometer pipette resistance and temperature. These curves are used to calculate the temperature change produced as a result of laser stimulation at the neuron-SiNW interface from a measured change in resistance of the thermometer pipette. **(c)** Comparison of temperature change produced by a p-type SiNW, a p-type SiNW with diffused Au, and no SiNW upon a 1 ms laser stimulation. The laser energy used for these three measurements were 100 μJ (p-type SiNW), 16.96 μJ (p-type SiNW with diffused Au), and 100 μJ (no NW). When a laser stimulus energy of 100 μJ (i.e., >18 times of the power threshold for PIN-SiNW based stimulation) was applied at the neuron-p-type SiNW interface, only a sub-threshold depolarization was produced and a temperature increase of 1.27 K was measured. At a laser stimulus energy of 16.96 μJ and duration of 1 ms at the Au-diffused and neuron-p-type SiNW interface, an AP was produced in the neuron and a temperature increase of 0.72 K was measured. No AP was generated without a NW present. Adapted with permission from ref (19).

micropipette resistance method to measure the temperature change ~ 2 μm away from the neuron-PIN-SiNW interface during laser induced AP generation in the neuron (Fig. 3.8a and Fig. 3.9). Laser induced AP generation at a 5.36 μJ laser energy (minimum energy necessary to produce an AP with PIN-SiNWs) resulted in a 0.36 K increase in temperature at the neuron-PIN-SiNW interface (Fig. 3.8b). In comparison to other photothermally-stimulating materials that produce 2 K temperature increases at similar pipette distances, this temperature increase is minor, suggesting a minor photothermal contribution to the stimulation mechanism described here. No temperature increase was observed in the absence of a SiNW (Fig. 3.9). Other control experiments further suggest that a photothermal effect is not the primary mechanism here (Fig. 3.9).

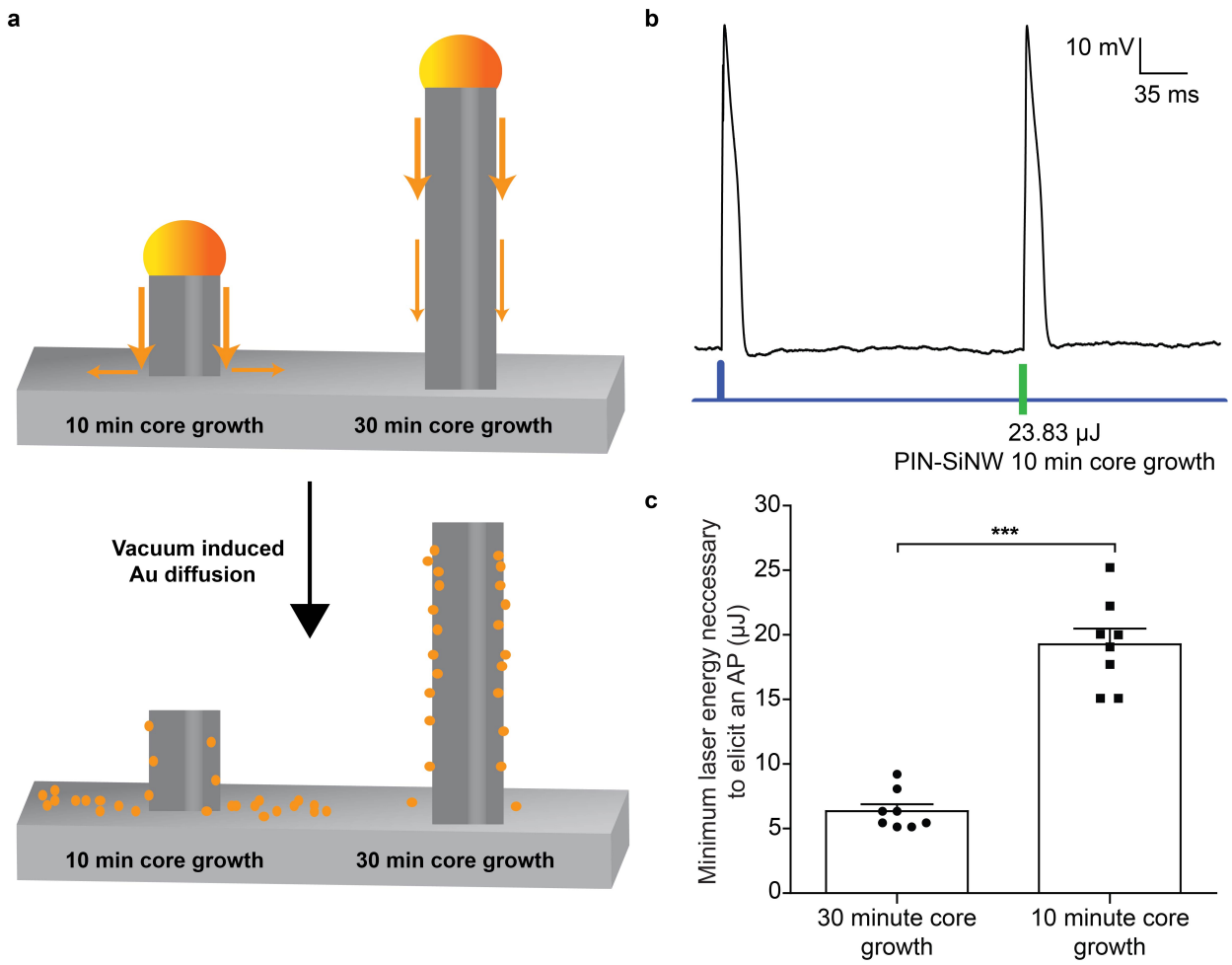

Figure 3.10. Decreasing core growth time decreases the efficiency of neuromodulation. (a) Schematic of Au diffusion during 10 min and 30 min core growth. (Top) During vacuum annealing, Au from the catalyst diffuses down the sidewalls of the PIN-SiNW and the growth substrate (also Si); orange arrows represent Au diffusion. (Bottom) After Au diffusion for 30 min in vacuum, we expect that for the much shorter NW core (left), much of the Au would have diffused off of the NW onto the growth Si substrate. **(b)** Patch clamp electrophysiology current clamp trace of membrane voltage (top) in DRG neuron stimulated by injected current (blue pulse) and illuminated by a 1 ms 28.83 µJ 532 nm laser pulse at the neuron-p-type SiNW with diffused Au interface (green bar). **(c)** Comparison of the minimum 532 nm laser energy necessary to elicit APs in several neurons interfaced with PIN-SiNWs grown with either a 30 min core (N = 6 biological replicates and a total of N=8 technical replicates) or 10 min core (N = 6 biological replicates and a total of N=8 technical replicates). Individual data points are indicated with black circles (30 minute growth) and squares (10 minutes growth). A paired t-test was used to determine statistical significance. p value < 0.0001. Error bars represent the standard error about the mean. Adapted with permission from ref (19).

In further delving into the neuro-excitation mechanism, we wanted to evaluate if the surface atomic gold plays a role in the observed photoelectrochemical current generation and neuromodulation. Since Au diffusion inherently occurs during PIN-SiNW shell deposition, we were unable to grow PIN-SiNWs without diffused Au. Thus, we first reduced the atomic Au distribution at the PIN-SiNW surfaces by promoting Au diffusion into the Si growth substrate (Fig. 3.10). We found that the average minimum laser energy necessary to elicit APs became 19.26 μJ, ~ 3 times that needed for typical PIN-SiNWs used in this work.

In a second approach, we compared the photoelectrochemical behaviors of pure 200-250 nm p-type SiNWs, and 200-250 nm p-type SiNWs with intentional Au diffusion (Fig. 19c-d, Methods). We chose p-type Si, instead of n-type Si to serve as controls, as p-type semiconductors in contact with electrolyte solutions experience band bending in such a manner that drives photogenerated electrons towards the semiconductor-electrolyte interface [12]. Thus, light illumination would allow for electron injection from the nanowire into the solution, yielding similar cathodic reaction as what occurs in the case of PIN-SiNWs. Indeed, both p-type and p-type/n-type (n- is the exposed end) diode Si devices have been used for photocathodes in electrochemical cells [12,13].

We measured photocurrents generated by these different nanowires as we did with the PIN-SiNWs. Currents could not be detected when the laser spot was shone onto a single p-type SiNW (Fig. 3.8c). However, currents from p-type nanowires with Au catalyst diffused at 750 °C for 30 min after growth were recorded at a laser duration of 10 ms (Fig. 3.8c). These current peaks were measured to be 28.8 pA and 15.0 pA for laser powers of 8.5 mW and 6.8 mW, respectively (Fig. 3.8c). Subsequent neuron

excitation experiments showed that Au-diffused p-type SiNWs and not p-type SiNWs were able to elicit APs with a minimum laser pulse energy of 17.4 μJ at a 1 ms pulse duration (Fig. 3.8d). The fact that diffused Au along p-type SiNW enhances photoelectrochemical current generation suggests its catalytic role in the interfacial chemical reaction. This is feasible given Au is more electronegative than Si; therefore, the photogenerated electrons can accumulate near the surface Au sites for cathodic reaction even under physiological condition. The exact chemical species that promote the cathodic reaction is unknown given the heterogenous nature of the culture medium used in the present study. Additionally, the atomic Au covered p-type SiNWs still yield lower amplitudes of currents and require a greater energy threshold to elicit APs in neurons upon light stimulation when compared with those recorded from PIN-SiNWs at similar laser powers and durations (Fig. 2.5b-c, 3.8b and 3.2).

Taken together, these results indicate the combined importance of the diffused Au in promoting the interfacial reaction at the PIN-SiNW surface and charge separation at the diode junction, both enabling photoelectrochemical current generation. More specifically, upon light illumination, holes migrate to the p-type core and electrons to the n-type shell (Fig. 3.8e). The electrons in the n-type shell are injected through surface state[14] (i.e., atomic Au and other surface defects)-enhanced processes into the electrolyte solution and are able to participate in cathodic reactions (e.g., reduction of protons) (Fig. 3.8e). The photogenerated holes, however, are swept into a spatially separated region, and consumed by recombination within Si or chemical scavengers at the exposed ends. The anodic reaction is expected to be slower given the exposed p-type surfaces (of the coaxial nanowire) have much smaller surface areas and contain no

catalyst, yielding the unipolar photocurrent recording at a timescale relevant to neural excitation. In this way, the PIN-SiNW behaves similarly to a wireless, nanoscale photoelectrochemical cell, with atomic Au to promote the cathodic process, which locally modulates neuronal function (Fig. 3.8e).

3.5 Conclusions and Outlook

This work represents the first study of single nanowire-based photoelectrochemical modulation of cellular excitability in a non-invasive, non-genetic, drug-like manner. Our results have implications for both fundamental studies and clinical therapeutics. For fundamental studies, coaxial p-type/i-type/n-type silicon nanowires are advantageous because gene transfection is not required for their use in neuromodulation, they can be administered in a drug-like fashion, their length scale allows for high spatial specificity, and their surfaces can be modified easily to allow for high affinity binding to specific cell types. Additionally, atomic Au plays the role that a catalyst would play in traditional photoelectrochemical devices in that it reduces the kinetic barrier necessary for photoelectrochemical current generation. The introduction of an even more potent "catalyst"[12] or internalization of these nanowires into neurons[15] could be used to reduce the optical power density necessary for stimulation, allowing for the use of an LED instead of a laser. These optimizations could be advantageous for expanding the possibilities of target organs for *in vivo* stimulation.

In clinical therapeutics, the potential degradability of silicon nanowires *in vivo* can be advantageous for temporally dependent applications and can be tuned by surface functionalization. Moreover, the ability of Si to absorb light in the near infrared regime can be useful for penetrating tissue. Due to the light penetration depth in tissue,

injecting these nanowires to target peripheral nerves could be a non-invasive treatment for diseases such as diabetic peripheral neuropathy, which are characterized by severe neuropathic pain. Collectively, our findings demonstrate a new nanotechnology for cellular membrane potential and excitability control, which may be broadly applicable to both fundamental single cell bioelectric studies[16,17] and photoresponsive therapeutics[18] in the clinic.

3.6 Experimental Methods

3.6.1 Cell culture protocol

Dorsal root ganglia (DRG) were excised from P1-P3 neonatal rats into DMEM-F12 on ice. They were then digested in 2.5 mg/mL trypsin (Worthington) in EBSS for 20 min in a 37°C shaker. Following trypsinization, digested DRGs were resuspended into EBSS + 10% FBS in order to inhibit further digestion by any remaining trypsin. Digested ganglia were then mechanically triturated via three glass pipettes decreasing in size. The resulting dispersed DRG cells were then resuspended into DMEM + 5% FBS + 100 U/mL penicillin + 100 µg/mL streptomycin and seeded onto glass bottom dishes previously treated with 0.01% poly L lysine.

3.6.2 Neuron electrophysiology experiments

DRG neurons were patch clamped in whole cell current clamp configuration using an Axopatch 200B amplifier (Molecular Devices). The output voltage signal was digitized at 16-bit resolution by an Innovative Integration SBC-6711-A4D4 data acquisition board. The digital analogue converter (DAC) of the data acquisition board supplied the command voltage to the amplifier. DRG neurons were mounted onto a Zeiss IM 35 microscope (Carl Ziess Microscopy) and visualized through a 40X (0.55 NA) microscope objective lens. Si nanowires were sonicated for 10 seconds off of the growth substrate into a modified Tyrode's bath solution (NaCl 132 mM, KCl 4 mM, $MgCl_2$ 1.2 mM, $CaCl_2$ 1.8 mM, HEPES 10 mM, glucose 5.5 mM, pH 7.4). These wires were then drop casted on top of the cultured neurons and allowed to settle for 20 minutes. Cells visually interacting directly with a single nanowire were then chosen to be tested for the generation of action potentials by laser pulses. Borosilicate glass pipettes

pulled on a CO_2 laser micropipette puller (Sutter Instruments P-2000) and flame polished using a custom microforge to produce 2 MΩ resistances when filled with internal pipette solution (NaCl 10 mM, KF 130 mM, $MgCl_2$ 4.5 mM, HEPES 10 mM, EGTA 9 mM, ATP 2 mM, pH 7.3) were used as patch pipettes. The 40X objective lens was used to focus a 532 nm DPSS laser (UltraLasers) spot (spot size: ~5 μm) onto the cell nanowire interface. This laser beam was modulated with an acousto-optic modulator (NEOS Technologies, Gooch & Housego, PLC) and power adjusted via a series of neutral density filters. Current injections were performed with amplitudes varying from 500 to 1000 pA depending on the current amplitude necessary to generate an action potential in each cell at a duration of 1 ms. Laser pulse durations at the neuron-SiNW interface were varied from 0.1 to 10 ms and powers varied from 1 to 85 mW as described in the results. The University of Chicago Animal Care and Use Committee approved all animal protocols used in this work.

3.6.3 Scanning electron microscopy

DRG neurons were cultured onto a glass coverslip. PIN-SiNWs were sonicated into culture medium, drop casted onto the cells, and left to be co-cultured with the cells for 24 hours. The cell/NW co-culture was then fixed with 4% paraformaldehyde and then stained with 4% osmium tetroxide for 1 hour at room temperature. The culture was then dehydrated with ethanol and critical point dried before being sputter coated with 8 nm of Platinum/Palladium metal. Images were taken on a Carl Zeiss Merlin FE-SEM.

3.6.4 Fluorescent microscopy

DRG neurons were cultured onto a glass coverslip. PIN-SiNWs were sonicated into culture medium, drop casted onto the cells, and left to be co-cultured with the cells for 24 hours. Neurons were fixed in 4% paraformaldehyde and stained with a rabbit anti-rat anti-β tubulin III primary antibody (Abcam ab18207) and a goat anti-rabbit Texas Red secondary antibody (Abcam ab6719). Cells were visualized on an inverted fluorescent microscope under a Texas Red filter and nanowires visualized via SEPC as demonstrated previously.

3.6.5 Temperature measurements

Thermometer pipettes with resistances of 2 MΩ were filled with bath solution and placed 2 μm away from the neuron/SiNW interface being tested. Pipette resistance was monitored as part of a tension divider using a voltage amplifier during action potential generation in the nearby cell. Conversion of pipette resistance to temperature was achieved by using a calibration curve produced individually for each pipette by pairing resistance values with a broad range of temperatures as a solution starting at 40^{o} C was cooled down passively to room temperature. The temperature was simultaneously recorded by a thermocouple placed very close to the pipette tip during the calibration procedure.

3.6.6 Photocurrent measurements

Si nanowires were synthesized as described above using a gold (Au) nanocluster-catalyzed chemical vapor deposition (CVD) process. Citrate-stabilized Au colloidal nanoparticles (Ted Pella Inc. 50 nm diameter) were deposited into quartz glass capillary

tubes (Sutter Instruments) and used as catalysts. Nanowire growth was performed under the same conditions as described above. Quartz capillary tubes containing silicon nanowires were pulled to produce pipettes with 14-20 MΩ resistances (pipette tip diameter, ~ 1 μm) and filled with bath solution. These pipettes were then mounted onto the aforementioned electrophysiology setup and current recordings were performed in voltage-clamp mode at 0 mV with the 532 nm laser focused onto single nanowires positioned ~10-30 μm from the tip of the pipettes, thus minimizing any changes in pipette resistance due to increases in temperature produced by light absorption . Laser pulses between 0.5 and 10 ms durations and 1 to 20 mW powers were used. Raw traces were filtered by averaging every 10 points of data.

3.6.7 Cell viability assay

DRG neurons were cultured onto glass bottom petri dishes. PIN-SiNWs were sonicated into culture medium, drop casted onto the cells, and left to be co-cultured with the cells for 24 hours. For experiments without light stimulation, cells were stained with a LIVE/DEAD cell viability assay kit (ThermoFisher Scientific) and the numbers of live cells in culture with and without nanowires were counted. For experiments with light stimulation, cells were stimulated via the 592 nm depletion laser on an SP5 laser scanning confocal microscope (Leica, USA, SP5 II STED-CW) under a 40x objective (Leica, USA, HCX PL APO) at various frequencies for various durations at a total energy density of 0.31 $\mu J/\mu m^2$ for each pulse. After stimulation, cells were stained with a LIVE/DEAD cell viability assay kit (ThermoFisher Scientific) and the numbers of live stimulated neurons, neurons neighboring the stimulated neurons, and unstimulated neurons were counted.

3.7 References

1 Famm, K., Litt, B., Tracey, K. J., Boyden, E. S. & Slaoui, M. A jump-start for electroceuticals. *Nature* **496**, 159-161 (2013).

2 Vetter, R. J., Williams, J. C., Hetke, J. F., Nunamaker, E. A. & Kipke, D. R. Chronic neural recording using silicon-substrate microelectrode arrays implanted in cerebral cortex. *IEEE Transactions on Biomedical Engineering* **51**, 896-904 (2004).

3 Zhou, W., Dai, X. C. & Lieber, C. M. Advances in nanowire bioelectronics. *Reports on Progress in Physics* **80**, doi:10.1088/0034-4885/80/1/016701 (2017).

4 Ghezzi, D. *et al.* A hybrid bioorganic interface for neuronal photoactivation. *Nature Communications* **2**, doi:10.1038/ncomms1164 (2011).

5 Ghezzi, D. *et al.* A polymer optoelectronic interface restores light sensitivity in blind rat retinas. *Nature Photonics* **7**, 400-406 (2013).

6 Mathieson, K. *et al.* Photovoltaic retinal prosthesis with high pixel density. *Nature Photonics* **6**, 391-397 (2012).

7 Carvalho-de-Souza, J. L. *et al.* Photosensitivity of neurons enabled by cell-targeted gold nanoparticles. *Neuron* **86**, 207-217 (2015).

8 Jiang, Y. W. *et al.* Heterogeneous silicon rnesostructures for lipid-supported bioelectric interfaces. *Nature Materials* **15**, 1023-1030 (2016).

9 Packer, A. M., Roska, B. & Hausser, M. Targeting neurons and photons for optogenetics. *Nature Neuroscience* **16**, 805-815 (2013).

10 Boyden, E. S., Zhang, F., Bamberg, E., Nagel, G. & Deisseroth, K. Millisecond-timescale, genetically targeted optical control of neural activity. *Nature Neuroscience* **8**, 1263-1268 (2005).

11 Mogyoros, I., Kiernan, M. C., Burke, D. & Bostock, H. Strength-duration properties of sensory and motor axons in amyotrophic lateral sclerosis. *Brain* **121**, 851-859 (1998).

12 Walter, M. G. *et al.* Solar Water Splitting Cells. *Chemical Reviews* **110**, 6446-6473 (2010).

13 Reece, S. Y. *et al.* Wireless Solar Water Splitting Using Silicon-Based Semiconductors and Earth-Abundant Catalysts. *Science* **334**, 645-648 (2011).

14 Sachsenhauser, M., Sharp, I. D., Stutzmann, M. & Garrido, J. A. Surface State Mediated Electron Transfer Across the N-Type SiC/Electrolyte Interface. *Journal of Physical Chemistry C* **120**, 6524-6533 (2016).

15 Lee, J. H., Zhang, A. Q., You, S. S. & Lieber, C. M. Spontaneous Internalization of Cell Penetrating Peptide-Modified Nanowires into Primary Neurons. *Nano Letters* **16**, 1509-1513 (2016).

16 Liu, C., Colon, B. C., Ziesack, M., Silver, P. A. & Nocera, D. G. Water splitting-biosynthetic system with CO_2 reduction efficiencies exceeding photosynthesis. *Science* **352**, 1210-1213 (2016).

17 Sakimoto, K. K., Wong, A. B. & Yang, P. D. Self-photosensitization of nonphotosynthetic bacteria for solar-to-chemical production. *Science* **351**, 74-77 (2016).

18 Silva, G. A. Neuroscience nanotechnology: Progress, opportunities and challenges. *Nature Reviews Neuroscience* **7**, 65-74 (2006).

19 Parameswaran, R. *et al.* Photoelectrochemical modulation of neuronal activity with free-standing coaxial silicon nanowires. *Nature Nanotechnology* **13**, 260-266 (2018).

Chapter 4: Optical training of cardiomyocytes with an SU8-PIN-SiNW composite material

4.1 Introduction

Electronic pacemakers can treat electrical conduction disorders in hearts. However, they are invasive, bulky, and linked to increased incidence of infection at the tissue-device interface. Thus, researchers have looked to other more biocompatible methods for cardiac pacing or resynchronization, such as femtosecond infrared light pulsing, optogenetics, and polymer-based cardiac patches with metal electrodes. Here, we demonstrate uninformed search-based non-genetic optical modulation of cells and tissues, in a manner that mimics naturally occurring extracellular signaling, *i.e.*, with random, fast and multisite input signals. Specifically, we developed a polymer-silicon nanowire composite mesh for serial and parallel generation of a massive number of optical inputs to biointerfaces. This is enabled by fast-moving light at silicon interfaces (*i.e.,* serial search) and nanowire-induced waveguiding (*i.e.,* parallel search), yielding low radiance optical training and memory effects in cultured cardiomyocytes. We also adapted these search processes in a more general manner for optical training of isolated hearts.

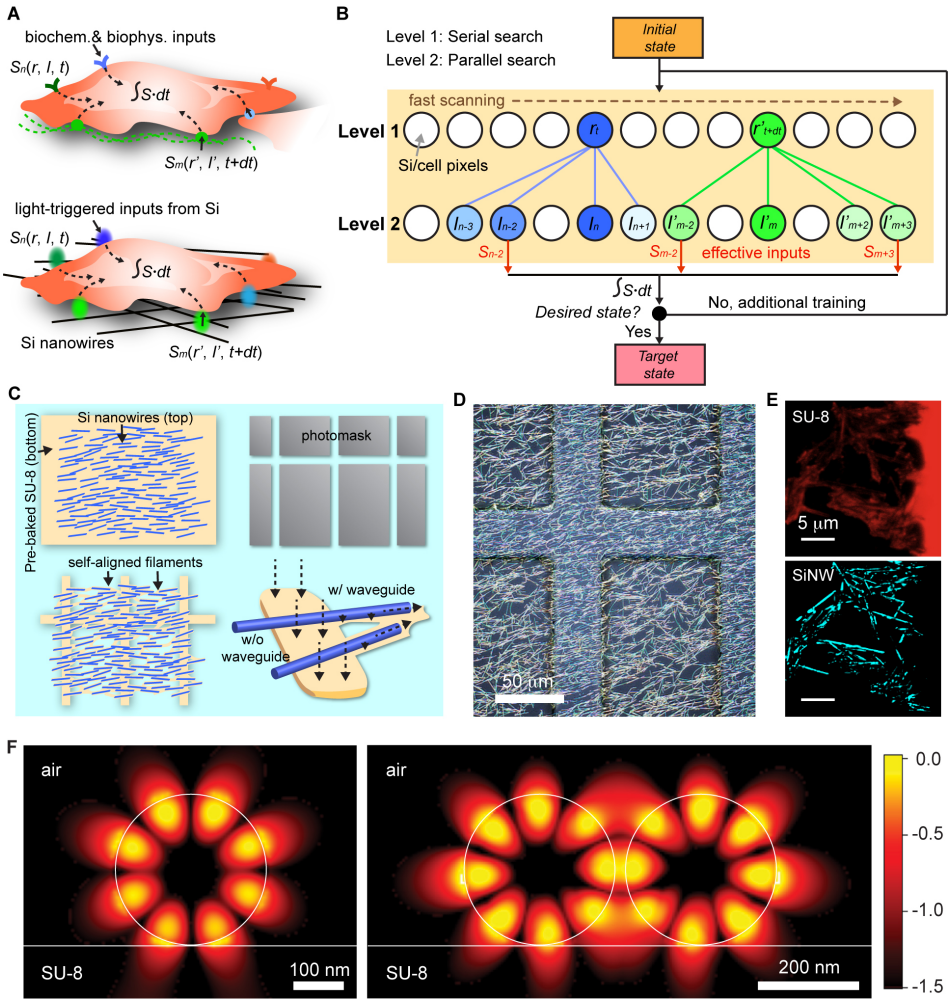

Figure 4.1. SU-8/PIN-SiNW mesh for uninformed search-based cellular stimulation. (**A**) Extracellular signaling under physiological conditions (top) and biomimetic optical training with a SU-8/PIN-SiNW mesh (bottom). (Top) Cells receive different types of biochemical and biophysical inputs (black dashed arrows, *e.g.*, $S_n(r,l,t)$ and $S_m(r',l',t+dt)$) *via* receptors (Y-shaped objects), focal adhesions (green dots) over the extracellular matrix (green dotted lines), and gap junctions (blue dot) at different times (*i.e.*, *t and t+dt*) across their surfaces. *r*, *I*, and *t* denote position, intensity, and time. Cells can then integrate these signals (*i.e.*, $\int S \cdot dt$) to perform their cellular functions. (Bottom) A scanning laser stimulus over single cells on a SU-8/PIN-SiNW mesh would yield random, transient, and minute photoelectrochemical inputs at multiple cell/Si interfaces (colored dots), mimicking the extra- and intercellular signaling. The cells can integrate these signals (*i.e.*, $\int S \cdot dt$) to trigger one overall modulation response. (**B**) Schematic diagram of the uninformed search-based optical training for cells and tissues. **Level 1** serial search scans across massive biointerface 'pixels' with either fixed or varied optical flux intensity, while **Level 2** utilizes the SiNW waveguiding effect to yield intensity variations in a group of pixels that are optically connected to (*i.e.*,

(Figure 4.1 continued) marked with blue and green lines) the illumination pixel. The search would continue until the target state is reached. (**C**) Schematic of fabrication for SU-8/PIN-SiNW mesh. After the SU-8 precursor (yellow) is deposited and pre-baked onto a glass slide, SiNWs (blue lines) are deposited into the upper layer of the polymer via mechanical transfer (top left). Photolithography is performed with a photomask (gray grid structure; top right) to produce a SU-8 grid structure with interconnected SiNWs (bottom left). SiNW waveguiding behavior during photolithography allows for the production of self-aligned SU-8 filaments (bottom left). Without waveguiding effect, we would not expect SU-8 filament formation under the SiNWs. (**D)** Wide-field reflected light microscopy image of a SU-8/PIN-SiNW mesh taken via a CMOS color camera on a 3D confocal laser microscope. (**E**) Confocal microscopy image of SU-8/PIN-SiNW mesh stained with Rhodamine 6G (blue: nanowires (bottom); red: SU-8 (top)), showing position matching between SiNWs and SU-8 filaments. (**F**) Calculated intensity profiles ($\log |E|^2$) of the waveguide modes in a single SiNW (left) and two SiNWs (right) at a wavelength of 365 nm. The simulation in the two SiNWs with a gap of 20 nm (right) shows that the waveguided light in the left SiNW is efficiently coupled to the right SiNW. The evanescent field penetrates into the polymer layer underneath the SiNWs, leading to polymerization of SU-8 filaments.

Cells receive stimuli via the engagement of receptors and membrane proteins on their surfaces, often integrating multiple chemical, mechanical, thermal, and electrical signals that are minute, random, and transient in nature, spatially from all over the cell to alter cellular function[1-2] (Fig. 4.1A). This type of stimuli has not been completely recapitulated in existing biological modulation methodologies, such as optogenetics, molecular uncaging and biomaterials based techniques[3-21]. Here, we develop a freestanding polymer-silicon nanowire (SiNW) mesh for use in optical training of cultured neonatal rat cardiomyocytes as well as adult rat hearts *ex vivo* to beat at a target frequency (Fig. 4.1A). We use an uninformed search approach for generating a large set of transient and localized input signals (*e.g.*, $S_n(r, I, t)$) to trigger a single integrated cardiac response (*i.e.,* $\int S \cdot dt$). This is enabled by (1) a fast-moving illumination interface via constant changes of either the light source or the sample locations (**Level 1**, serial process, Fig. 4.1B), and (2) a high density array of SiNWs that can not only

generate light-induced physicochemical outputs but also exhibit waveguiding behavior[22-25] for additional light intensity modulation (**Level 2**, parallel process, Fig. 4.1B). Integrating these modalities allows for our training approach to mimic physiological stimuli, by spatially engaging whole cells with massive numbers of optical inputs during a short period of time (Fig. 4.1A). Our training method consists of: (1) identifying a pre-stimulus frequency via imaging, (2) optically training cells using a moving laser stimulus with programmed ON/OFF cycles, and (3) tracking a post-stimulus frequency as feedback for subsequent training until the cells beat at the target frequency (Fig. 4.1B). This method can avoid the potential issue of missing optimal conditions (*e.g.*, $S_n(r, I, t)$ or $S_m(r', I', t+dt)$ or their combinations) for cellular modulation, as might be the case in point stimulation techniques[7-10,18], and does not require any prior knowledge about the exact biointerfaces being generated.

4.2 Polymer-silicon nanowire mesh characterization

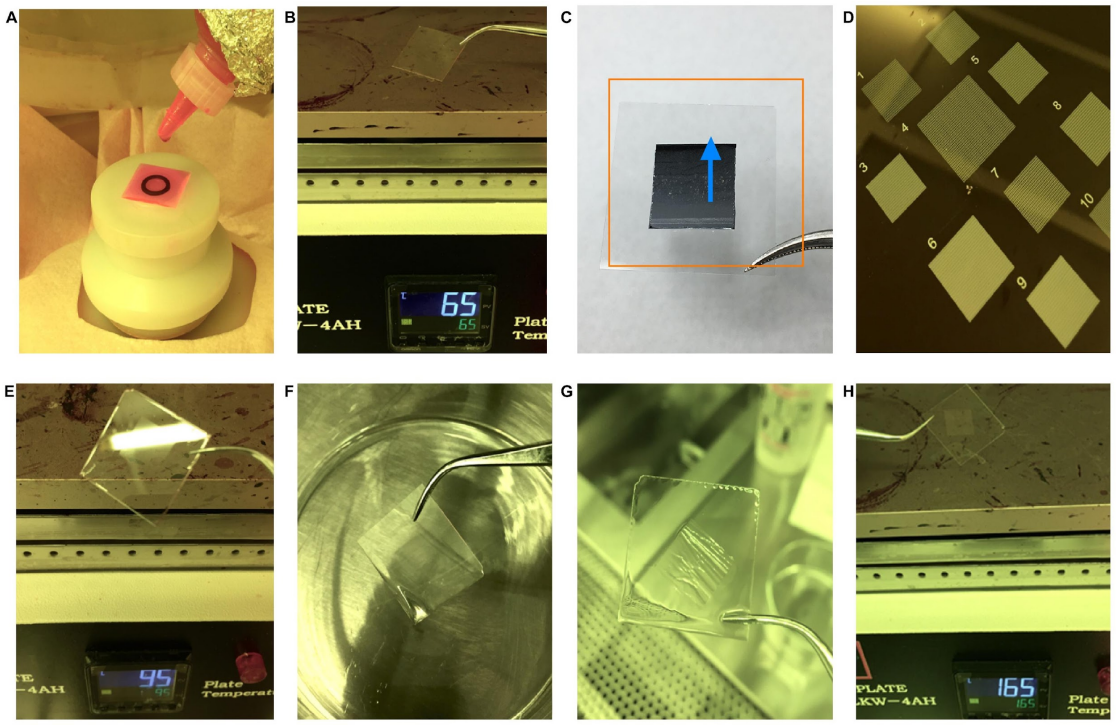

Figure 4.2. SU-8/SiNW meshes are prepared via a photolithographic process. SU-8 grid structure is fabricated via photolithography. (**A**) SU-8 2005 precursor is spun onto a glass slide at 2500 rpm for 5 sec and 3500 rpm for 55 sec to form a 5 μm thick SU-8 layer on the glass slide. (**B**) SU-8 precursor is heated to 65° C for 180 sec and then 95° C for 180 sec. (**C**) After this pre-bake step, SiNWs are mechanically translated from the original growth wafer onto the surface of the SU-8. Orange box denotes glass slide with SU-8. SiNW growth wafer (SiNWs face glass slide) is translated across SU-8 surface in the direction of blue arrow, and SiNWs break off growth substrate and become embedded in the SU-8 surface. (**D**) Samples are patterned via a chrome photolithography mask and hard contact lithography using a UV light exposure dose of 175 mJ. (**E**) After exposure, samples are baked again at 65° C for 180 sec and 95° C for 180 sec for the post-bake step to crosslink SU-8. (**F,G**) Samples are developed in SU-8 developer for 30 seconds, rinsed in IPA for 15 sec, and dried under N_2. (**H**) Finally a post-bake step is performed at 165° C for 20 min.

The composite mesh was fabricated using SU-8 (*MicroChem*) as the polymer support component and coaxial *p-type/intrinsic/n-type* silicon nanowires (PIN-SiNWs), previously shown to produce photoelectrochemical currents and elicit action potentials in single neurons(*9*), as the semiconductor modulation component (Fig. 4.2). With

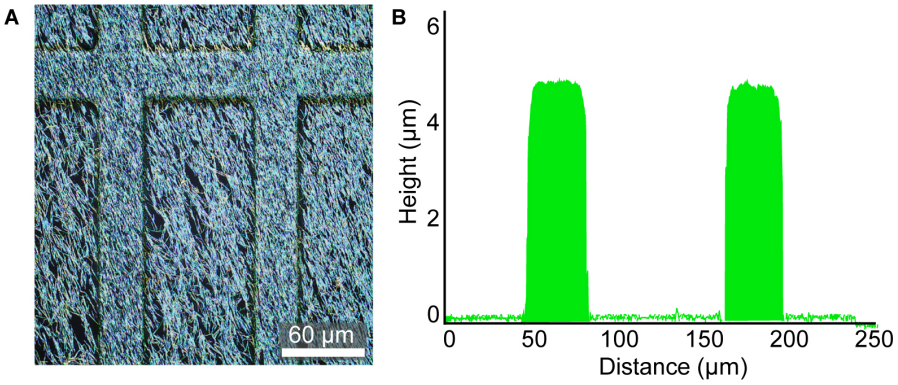

Figure 4.3. SU-8/PIN-SiNW mesh has SiNWs incorporated into the window regions. (**A**) Confocal reflected light microscope image showing a high density SU-8/PIN-SiNW mesh. **(B**) Corresponding height profile from confocal reflected light 3D reconstruction of image (**A**) showing 5 µm height of SU-8/PIN-SiNW mesh. These height profile scans are representative of 30 scans from 30 different samples.

mechanical transfer and subsequent photolithography (Fig. 4.1C), we integrated a high-density mesh of PIN-SiNWs onto a SU-8 grid (Fig. 4.1D, 4.2, 4.3). The resultant composite (SU-8/SiNW) contains a high density PIN-SiNW network that spans across the 86 µm x 424 µm window regions in the SU-8 grid (Fig. 4.1D, 4.3). Using confocal microscopy, we identified thin filaments of SU-8 polymerized beneath the SiNWs in the window regions (Fig. 4.1E). These thin SU-8 structures were not formed by direct

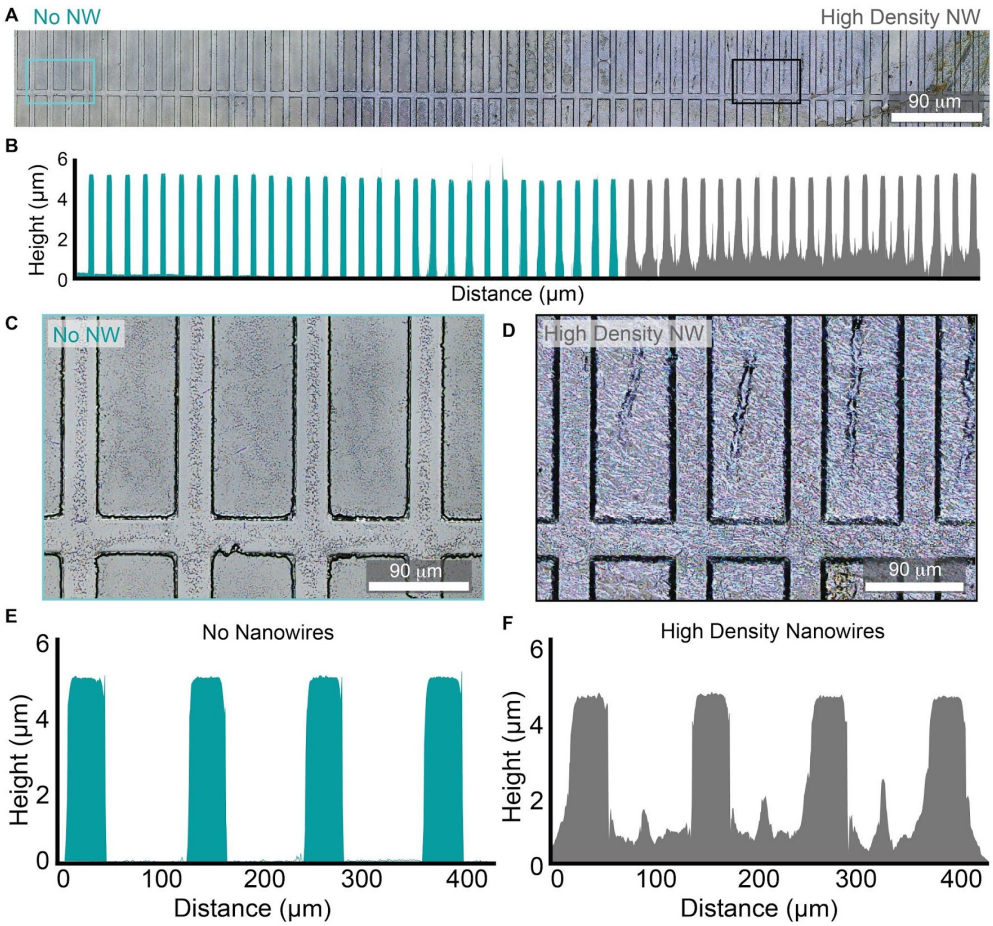

Figure 4.4. SiNWs waveguide light during the UV exposure. (**A**) Confocal 3D reflected light microscopy widefield color image of SU-8 mesh with a very high photolithography UV exposure dose (400 mJ) fabricated with SiNWs only present in the right half. A higher exposure dose was intentionally used here (higher than that of normal sample preparation in all other parts of the text) to enhance the over-exposure of the SU-8 film in the window regions, so that it is detectable in 3D reconstruction. This higher exposure dose does not cause excessive SU-8 crosslinking in the window regions in the absence of nanowires. (**B**) Height profiles reconstructed from confocal 3D data of the SU-8 mesh in (**A**). This displays the existence of SU-8 film in the mesh window regions in the presence of high density SiNWs (gray traces) and minimal SU-8 in the window regions with negligible SiNWs (blue traces). These are representative traces of 4 different meshes. (**C,D**) Zoomed in confocal 3D images of the SU-8 mesh from (**A)** in the presence of SiNWs (black box inset from (**A**)) and in the absence of nanowires (blue box inset from (**A**)). (**E,F**) Height profiles reconstructed from laser scanning confocal 3D data of SU-8 mesh regions in (**C**) and (**D**), respectively.

exposure to UV light, as the window regions are blocked by the photolithography mask (Fig. 4.1C, 4.4). Moreover, in the absence of SiNWs, we saw no evidence of these thin

SU-8 filaments (Fig. 4.4), suggesting that the mechanically transferred SiNWs can act as an optical guide for SU-8 polymerization (Fig. 4.1C). Simulations performed via a

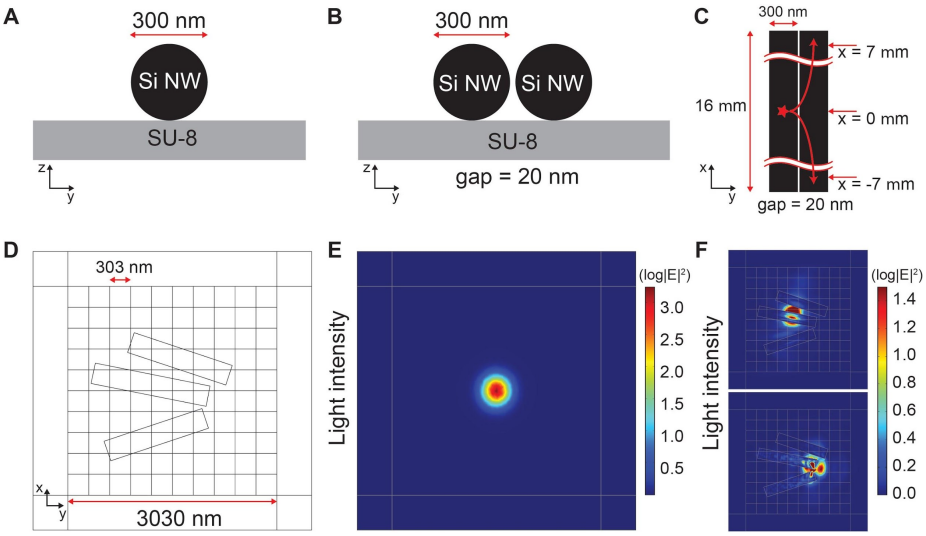

Figure 4.5. 3D FDTD and FEM Simulations demonstrate nanowire waveguiding. (**A-C**) 3D FDTD simulations to calculate intensity profiles of waveguide modes in single and double SiNWs on the SU-8 substrate. The SiNWs with a diameter of 300 nm are positioned along the x-axis in the calculation domain with a size of 16000 x 1200 x 550 nm^3. Cross-sectional views of (**A**) a single SiNW and (**B**) double SiNWs with a gap of 20 nm. (**C**) Top-view of the double SiNWs. Dipole sources are introduced in the x=0 plane in the left SiNW. Waveguide modes are coupled to the right SiNW and detected in the x=±7 mm plane. The time-averaged intensity profile of the waveguide mode with the strongest intensity is shown in Fig. 1F. (**D-F**) 3D FEM simulations to calculate light absorption in SiNWs. (**D**) Simulation domain with a size of 3030 x 3030 x 3000 nm^3 which is digitized by 10 x 10 pixels in the x-y plane. Three SiNWs with diameters of 300 nm are introduced. The surrounding is water with a refractive index of 1.33. (**E**) Horizontally-polarized Gaussian beam with a wavelength of 514 nm and a spot size of 520 nm, which scans across the calculation domain. (**F**) Calculated light intensity (log $|E|^2$) for two different pump positions (top and bottom), which are the same as the ones in Fig. 2E. The field profiles are shown in the z=0 plane.

finite-difference time-domain (FDTD) method (Fig. 4.5) show that SiNWs can synergistically waveguide UV light with neighboring SiNWs during the photolithography process. The evanescent field of the waveguided light around single (Fig. 4.1F, left) or multiple (Fig. 4.1F, right) SiNWs allows for *in situ* SU-8 polymerization to produce well-aligned mechanical support for the high-density SiNW mesh.

4.3 Uninformed search-based optical training of primary cardiomyocytes

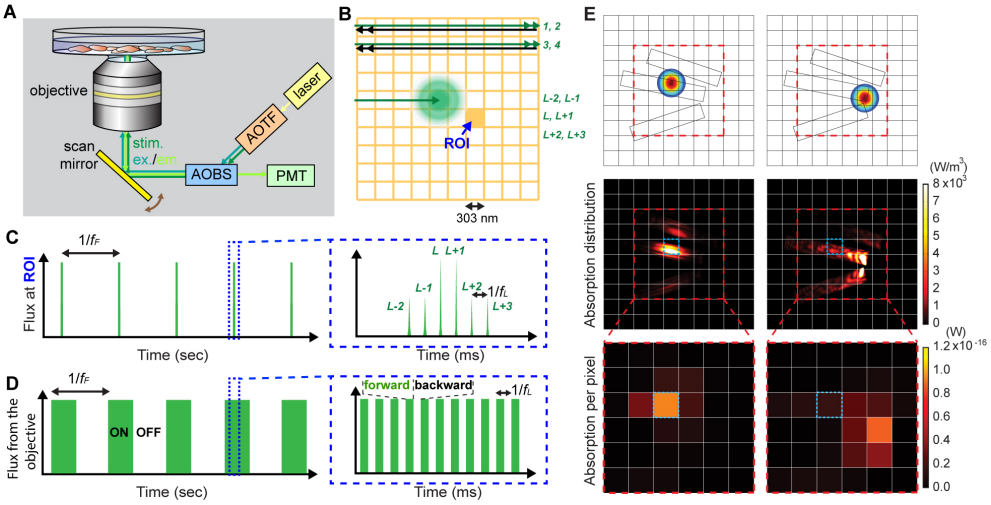

Figure 4.6. Uninformed search platform integrates massive variations in biointerface location and stimulation strength. (**A**) Scanning confocal microscopy set-up used to optically train primary neonatal cardiomyocytes cultured on a SU-8/PIN-SiNW mesh. The stimulation light (514 nm, green) is focused through a 40x objective lens via a scan mirror (yellow) onto the sample. For recording beating patterns, either DIC imaging or Fluo-4 calcium imaging (shown here) can be used. AOTF, acousto-optical tunable filter (orange); AOBS, acousto-optical beam splitter (blue); PMT, photomultiplier tube. (**B**) Schematic of optical stimulus on a miniaturized pixel grid. The individual pixel size is 303 nm x 303 nm. During optical stimulation, the 514 nm laser (green spot) is scanned line by line at a 1 kHz line-scan rate (f_L) with 2 repeats for each line. Each line contains half in the forward direction (green), and the other half in the backward direction (black). The laser is on when forward (green double head arrow, scans 1,2,3,4) and off when backward (black double head arrow). A given pixel, region of interest (ROI), will experience photon fluxes L-2 and L-1 from the pixel above, L and L+1 at the ROI, and L+2 and L+3 from the pixel below as the laser scans. (**C**) Schematic of photon flux (y-axis) at one given ROI (*e.g.*, the filled orange grid in **B**) over time (x-axis). f_F is the scanning frame rate or the targeted training frequency. At a single ROI, the flux during a single scanning/training frame would experience 2 low intensity (L-2, L-1), 2 high intensity (L, L+1), and 2 low intensity (L+2, L+3) pulses (Zoom-in view in **C**). It is doublet because we used 2 repeats for each line scan. Additionally, the intensity variation is a result of the fact that the laser beam is an airy disc which expands beyond the pixel size. The time between pulses at the ROI is $1/f_L$, where f_L is the laser line-scan rate, *i.e.*, 1 kHz in the present study. (**D**) Schematic of the photon flux directly coming out from the objective (y-axis) over time (x-axis). The laser is set to scan over the training area with a period of $1/f_F$. 'ON' and 'OFF' denote 'search' and 'not search' within a single training frame, respectively. During the 'ON' stage, the laser is turned on only in the forward scan (green bar, the zoom-in view in **D**) and is off during the backward scan (space between green bars, the zoom-in view in **D**). (**E**) FEM simulation to calculate a map of light absorption in regions with SiNWs in a pixel grid. Three 300-nm-diameter SiNWs are introduced for proof-of-concept demonstration, and

(Figure 4.6 continued) two different pump positions are examined (top). The wavelength and spot size of the pump light are set to 514 nm and 520 nm, respectively. The calculated absorption distribution in each pump position (middle panel) is used to plot the 6 x 6 digitized absorption matrix (bottom). In the bottom panel, the absorption per pixel is calculated by integrating the absorption distribution in each single pixel with a volume of 303 x 303 x 400 nm^3. We also mark the same pixel as a blue dotted box for a clear comparison of the pump position-dependent absorption.

With this polymer-silicon nanowire mesh, we designed an uninformed search-based optical training method for cultured cardiomyocytes (Fig. 4.6). This approach pairs confocal laser scanning[20,26] (*i.e.,* the serial search for optimal stimulation locations on each cell, Fig. 4.1B) with PIN-SiNW-enabled waveguiding of the light stimulus (*i.e.,* the parallel search for optimal photoelectrochemical(*9*) stimulation intensities; Fig. 4.1B) to produce a combinatorial collection of transient inputs over whole cell areas (lower, Fig. 4.1A). First, we scanned a diffraction-limited 0.6 μW 514 nm laser spot over a region of interest, at a 1 kHz line-scan rate (f_L) with 2 repeats for

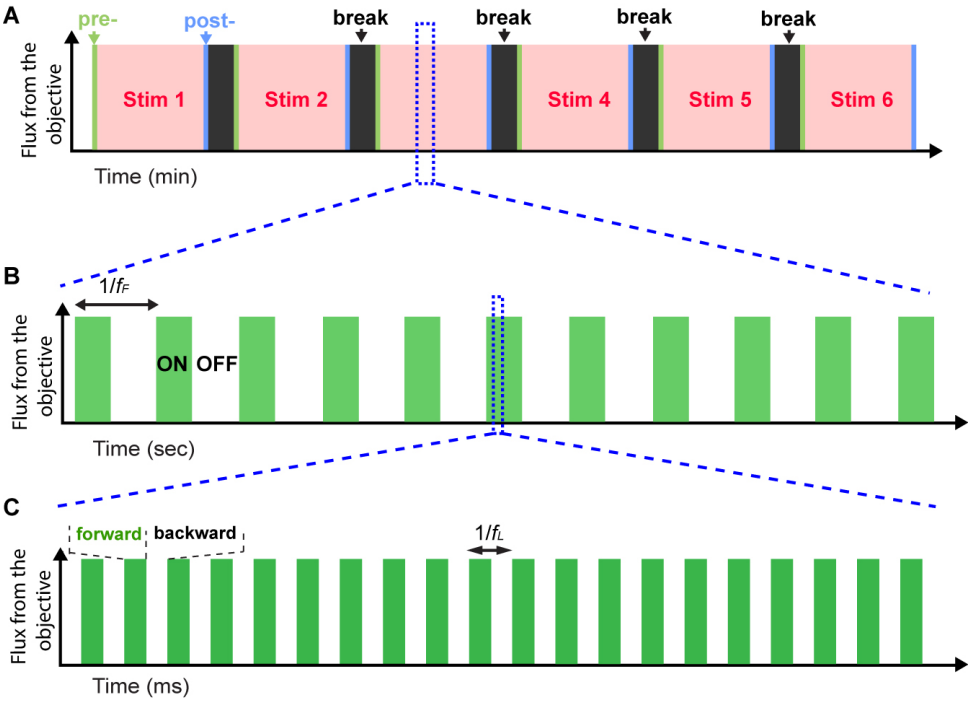

Figure 4.7. Laser Scanning Confocal stimulation pattern used for optical training of cardiomyocytes. (**A**) Trace of a hypothetical optical training scheme with light flux over the full pixel grid as the y-axis and time as the x-axis. Groups of pink bars

(Figure 4.7 continued) represent optical stimulation periods, of which 6 are shown here. Breaks between these training periods are shown in black, which are used to avoid light-induced cytotoxicity. Green and blue bars represent the pre- and post-stimulation recording periods, which can be done with either calcium imaging or DIC imaging. Cycles of a pre-stimulation recording, training, post-stimulation recording, and break, are repeated until cells reach the desired training frequency. (**B**) Hypothetical trace of a portion of an optical stimulation period. Light flux over the full pixel grid is displayed on the y-axis, and time on the x-axis. The targeted frequency or the scanning frame-rate (f_F) is set by the timing of "ON/OFF" stimulation cycles. Here, during the 'ON' period, 514 nm light scans line by line across the whole pixel grid (green bars). During the 'OFF' period, no scanning occurs. In this way, cells are trained to beat at the targeted frequency (f_F). (**C**) Hypothetical trace of the light flux through the objective (y-axis) over time (x-axis) during a port of the "ON" period. The laser scans across the pixel grid at a line-scan frequency (f_L) of 1,000 Hz with the laser on in the forward direction and off in the backward direction.

each line (Figs. 4.6A-B, 4.7). Given each line crosses a total of 1,024 pixels (pixel area, ~ 0.09 μm^2), this yields an average pixel-scan rate of 1.024 MHz, that is much faster than the frequency range for targeted cardiomyocyte contractions or the training frame rate (~ 0.5 – 2 Hz, $\boldsymbol{f_F}$). The significant temporal difference between the individual stimulus and the final biological response allows for cellular integration (*i.e.,* $\int S \cdot dt$) of multiple tiny inputs that are delivered from individual locations (*i.e.*, the "*r"* in $S_n(r, I, t)$). After the full area of interest is scanned (*i.e.*, "ON" state), an "OFF" state without laser scanning is employed to match the desired training frame rate ($\boldsymbol{f_F}$, Fig. 4.6C). The training towards $\boldsymbol{f_F}$ is achieved via cycles of "ON/OFF" modulations (Fig. 4.6C). Each pixel (*e.g.*, the orange square in Fig. 4.6B) experiences six direct incident fluxes per training frame, due to the larger diffraction-limited airy disc diameter (> 500 nm) of the laser beam versus the size of a single pixel (303 nm), and the choice of 2 scanning repeats used in the present study (Fig. 4.6D). Second, in parallel with the scanning modality, the light absorption and correspondingly the subsequent cellular input (*e.g.*, $S_n(r, I, t)$) from each pixel (pixel size: ~ 0.09 μm^2) also varies due to the distribution of

SiNWs. We performed finite-element method (FEM) simulations to generate a map of light absorption in regions of the mesh with SiNWs when the laser spot scans across those regions (Fig. 4.6E, 4.5). The simulation shows that the SiNWs allow for light propagation into surrounding pixels. Moreover, light propagation to pixels outside of the diffraction-limited spot only occurs at pixels containing SiNW segments (Fig. 4.6E, 4.5). The exact configuration of the SiNWs around the illumination spot determines the distribution of absorbed energy at nearby pixels that contain both a cell and SiNW(s). A region of interest (blue dotted box; Fig. 4.6E) will then absorb light energy under both direct laser illumination (bottom left, Fig. 4.6E) and laser illumination at a nearby pixel (bottom right, Fig. 4.6E). The variation of the absorbed energy at each pixel during one "ON" period (Fig. 4.6D) would also be massive, given the range of the laser spot location (> 3,000 μm^2) and the high density SiNWs; this would provide the variable input strengths (*i.e.*, the I in $S_n(r, I, t)$) at each localized biointerface (*i.e.*, at each pixel, ~ 0.09 μm^2). Taken together, the combination of the scanning operation (*i.e.*, level 1, serial search) and the SiNW network (*i.e.*, level 2, parallel search) efficiently utilizes the laser stimulus, by drastically expanding the cellular modulation positions (*i.e.*, as defined by the 1.024 MHz pixel-scan rate, and the pixel size of ~ 0.09 μm^2) and intensities (*i.e.*, through SiNWs-enabled waveguiding and photoelectrochemical effect[9], while keeping the laser radiant low.

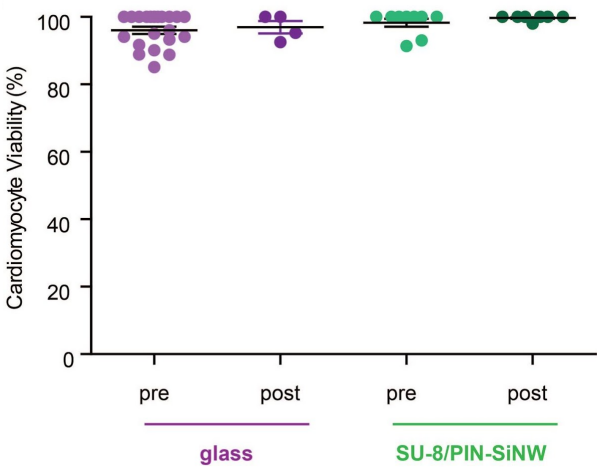

Figure 4.8. Viability assay demonstrates that optical training of cells cultured on SU-8/PIN-SiNW mesh does not induce cytotoxicity. (**a**) Live/Dead staining of cardiomyocytes and cardiac fibroblasts cultured on fibronectin coated SU-8/PIN-SiNW meshes before optical training (top) and after optical training (bottom). Live cells are green, dead cells are red, and the SU-8/PIN-SiNW mesh is purple. (**b**) Percentage of live cardiomyocytes cultured on glass (purple) and the SU-8/PIN-SiNW mesh (green) before and after optical training (lighter dots and darker dots, respectively). Only cardiomyocytes were counted (not fibroblasts) and cardiomyocytes were distinguished from fibroblasts by cell morphology. Each point represents the percent viability from one image taken from a total of 4 different glass samples and 3 different SU-8/PIN-SiNW meshes. Percent viability was calculated from 21, 4, 9, and 7 images for glass pre training and post training, and SU-8/PIN-SiNW pre-training and post-training, respectively. Averages and standard error are indicated with a black horizontal line and black bars above and below average, respectively.

We next demonstrate the use of this uninformed search method to train cardiomyocytes to beat at a target frequency. We cultured neonatal rat ventricular cardiomyocytes on fibronectin-coated composite meshes, and confirmed the substrate biocompatibility via a live/dead viability assay (Fig. 4.8). Immunofluorescence images

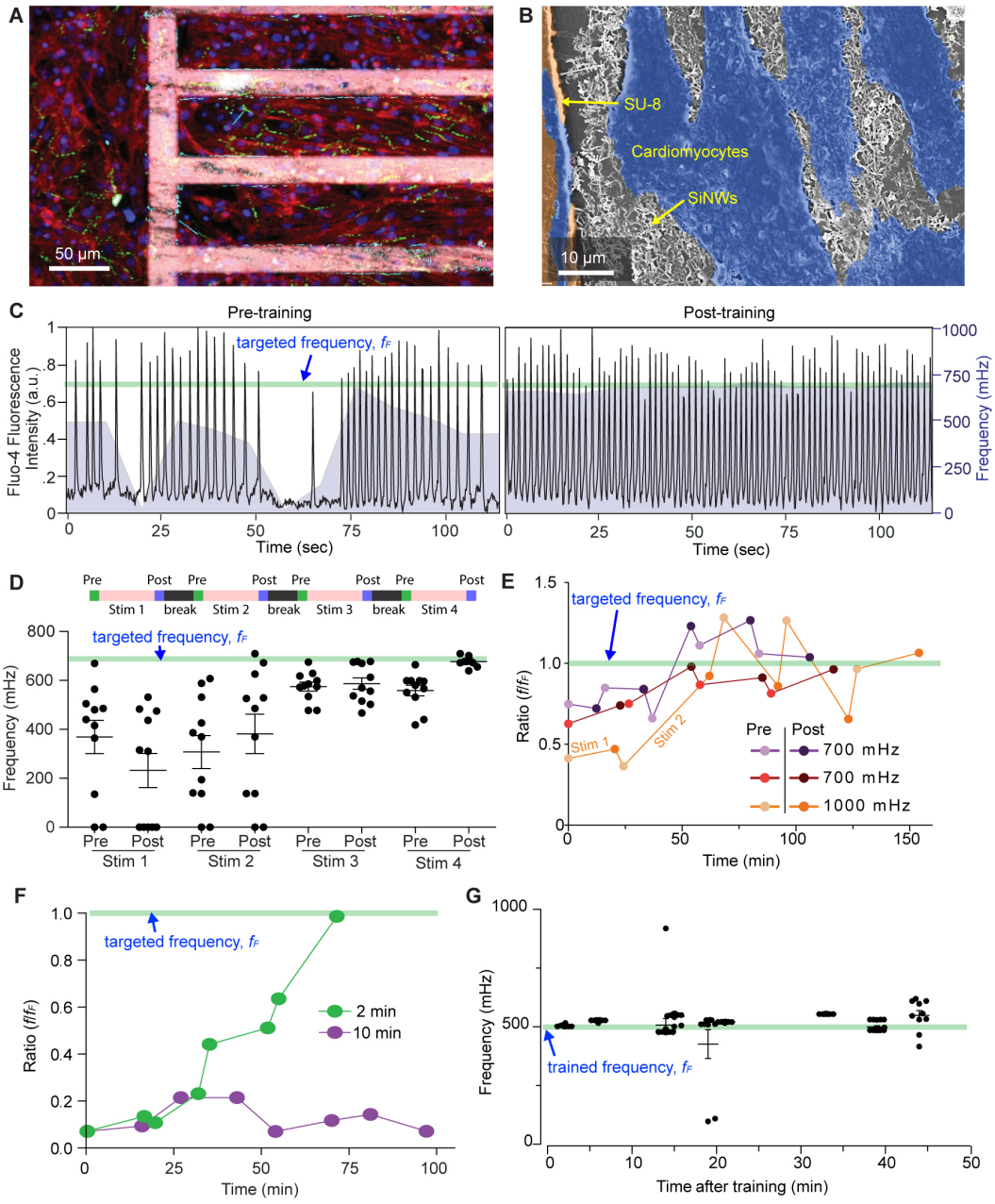

Figure 4.9. Optical training of cardiomyocytes with the composite mesh. (**A**) Confocal fluorescence microscope image of primary neonatal cardiomyocytes cultured partly on a fibronectin-coated SU-8/PIN-SiNW mesh (middle and right) and partly on fibronectin-coated glass (left end). Mesh was stained with Rhodamine B (pink) and cardiomyocytes were stained with anti-troponin (red), anti-connexin 43 (green), and DAPI (blue). (**B**) False colored scanning electron microscopy image of the biointerface, showing cardiomyocytes (blue), SU-8 grid (orange) and PIN-SiNWs (white). (**C**) Fluo-4 calcium imaging traces (black traces) depicting pre- and post-training beating patterns for a representative cell, from a group of 11 cardiomyocytes that were trained to beat at 700 mHz (light green line). Running averages of the frequencies of 11 cells (window

(Figure 4.9 continued) size: 18 seconds or 100 imaging frames) were overlaid with the black traces as the purple mountain plots. (**D**) Average frequencies for each stimulation period throughout the training. The stimulation periods were 20.98 (880 frames), 25.64 (1075 frames), 25.64, and 25.64 minutes for Stim 1, Stim 2, Stim 3 and Stim 4. 11 data points (*i.e.*, recorded from 11 cells) are plotted for each pre- and post- condition, with their means (black horizontal line) and S.E.M. (black bars above and below average). For all training experiments, length of one particular stimulation period (*e.g.*, Stim 2) was determined based on how the cells responded to the previous stimulation period (*e.g.*, Stim 1). (**E**) Average beating frequencies were plotted as ratios of the beating frequency to the targeted beating frequency (or the scanning frame rate, f_F) over time for cells from 3 different training experiments. 4 cells were used in the 700 mHz experiment (purple), 5 cells in the second 700 mHz experiment (red), and 7 cells in the 1000 mHz experiment (orange). The frequencies of pre- and post-trainings are depicted with lighter colored dots (pre-) and darker colored dots (post-). Time between pre- and post-stimulation measurements includes that used for the pre-stimulation frequency measurement and the stimulation time. Time between the post- and next pre-stimulation measurements includes that used for the recording of the post-stimulation frequency and the 2 min break time. The green line indicates the targeted frequency (f_F). Connections between dots do not represent real data and are included as a way to guide the trend. These are representative traces of N=9 experiments (91 cells total). (**F**) Average beating frequencies were plotted as ratios of the beating frequency to the targeted beating frequency over time for cells from 2 different training experiments, with varying break times (2 min – green; 10 min – purple). 6 cells were trained in the 2 min break experiment (green) and 8 cells in the 10 min break experiment (purple). Time between pre- and post- stimulation measurements includes both the recording of the pre-stimulation frequency as well as the stimulation time. Time between the post- and next pre- stimulation measurements includes both the recording of the post-stimulation frequency and the 2 or 10 min break time. Connections between dots do not represent real data and are included as a way to guide the trend. These are representative traces of N=9 experiments (91 cells total) for the 2 min break time, and N=2 experiments (15 cells total) for the 10 min break time. (**G**) Beating frequencies of cells within a ~300 μm radius from the center of a training area, at various times after training at 500 mHz. Beating frequencies of 8 cells, 8 cells, 16 cells, 13 cells, 9 cells, 10 cells, 11 cells, 17 cells, and 10 cells were measured at each post-stimulation time point (from short to long), including the times for recordings. The field of view for each frequency recording was different. Means (black horizontal line) and S.E.M. (black bars above and below average) are depicted for each time point.

demonstrated that the cells in contact with the mesh aligned with the long axis of the SU-8 grid structure, and were well connected via gap junctions (green) (Fig. 4.9A). Scanning electron microscopy imaging confirmed direct contact between the

cardiomyocytes and the PIN-SiNWs both on the SU-8 grid itself and in the window regions of the mesh (Fig. 4.9B).

In order to characterize the cellular response to optical training, we used either differential interference contrast (DIC) or calcium imaging (Fig. 4.9C) to record the beating frequency (see Supplementary Information). The recordings of the cells were done pre- and post- each optical stimulation period (*i.e.*, green/purple/pink bars, upper inset of Fig. 4.9C), and were separated by user-defined break times (black bars, upper inset of Fig. 4.9D). Each stimulation (*e.g.*, Stim 2) includes cycles of "ON/OFF" modulations (Fig. 4.9D). In a representative experiment, we trained a group of 11 cardiomyocytes to beat at 700 mHz (light green line, Fig. 4.9C), The cells displayed an incoherent beating pattern with frequencies ranging from 0 to 669 mHz prior to any stimulations, as shown by calcium imaging traces of a representative cell (Fig. 4.9C). After optical training for a total of four stimulations that are separated by 2 min breaks, this cell beat at ~ 700 mHz (Fig. 4.9C**)**. We observed that the spread of the frequencies decreased with more optical training and that the frequencies measured trended towards the target frequency of 700 mHz (Fig. 4.9D). The post-stimulus frequency is not always the same as the pre-stimulus frequency for the next training session, as expected for a training process (Fig. 4.9D). The estimated stimulation laser radiant exposure is ~ 1.3 mJ/cm^2 per training frame (*i.e.*, during each cycle of "ON/OFF", or 1/$\boldsymbol{f_F}$, Fig. 4.6D), which is the lowest among existing non-genetic biological modulation methods[7-10,15,18,19]. We also confirmed that the calcium imaging itself cannot yield a

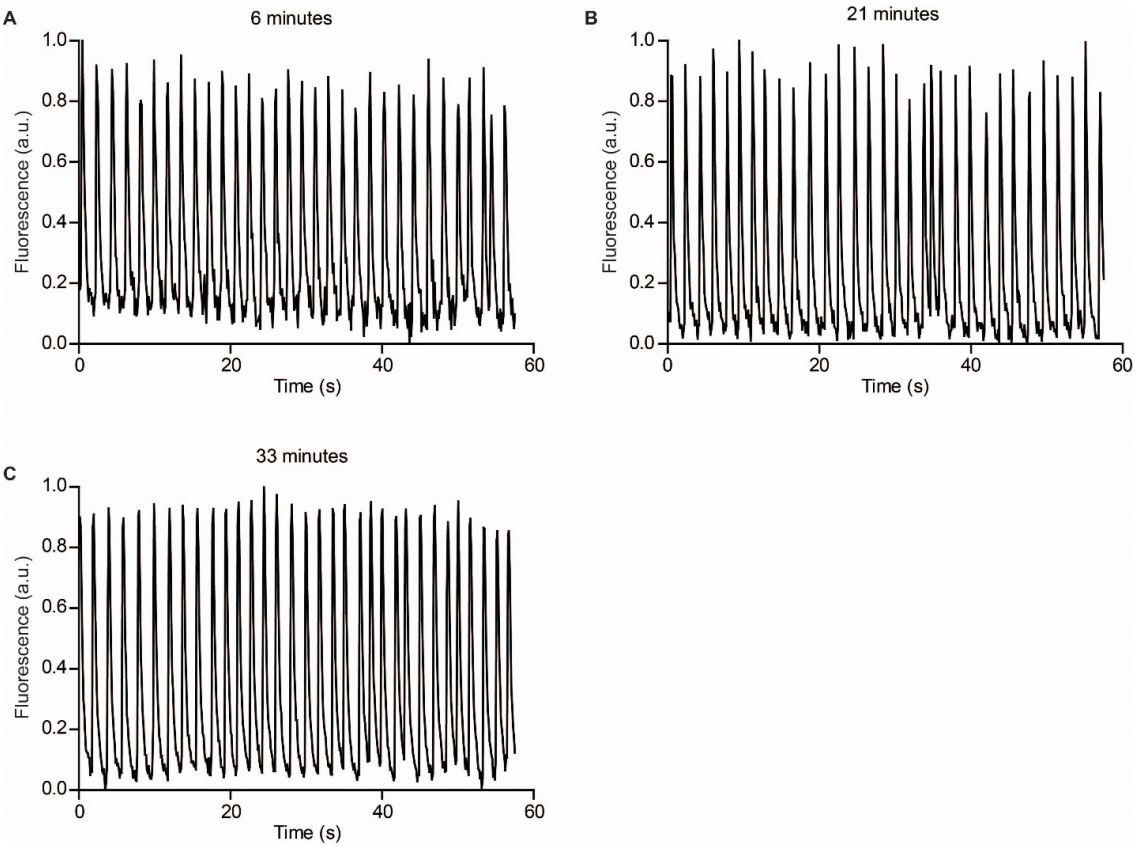

Figure 4.10. Fluo-4 recordings do not affect the beating frequency of the cardiomyocytes. (A-C) Fluo-4 recording of 3 different cardiomyocytes cultured on an SU-8/PIN-SiNW mesh (**A**) 6 min, (**B**) 21 min, and (**C**) 33 min after being optically trained to a 500 mHz beating frequency. All recordings were performed on laser scanning confocal microscope using a 488 nm laser.

training effect (Fig. 4.10), given its high acquisition rate (> 5 frames per second) is beyond the range that isolated cardiomyocytes can respond to. This approach can be applied to cardiomyocytes with different initial and targeted frequencies (Fig. 4.9E), but the paths can vary as shown in the 2 traces from targeted training at 700 mHz (Fig. 4.9E). Additionally, the condition for individual stimulations (*i.e.*, duration) can be controlled by the user as a real time feedback to improve the overall training efficacy, *e.g.*, the Stim 2 is 2x in duration than that of Stim 1 for a targeted training at 1000 mHz (Fig. 4.9E). This fact also suggests that although the searching is uninformed (*i.e.,* the

"Level 1" and "Level 2", in Fig. 4.1B), the complete training at this stage would still involve decision making from the users (*i.e.*, "Desired state?", "Yes", "No, additional training", in Fig. 4.1B).

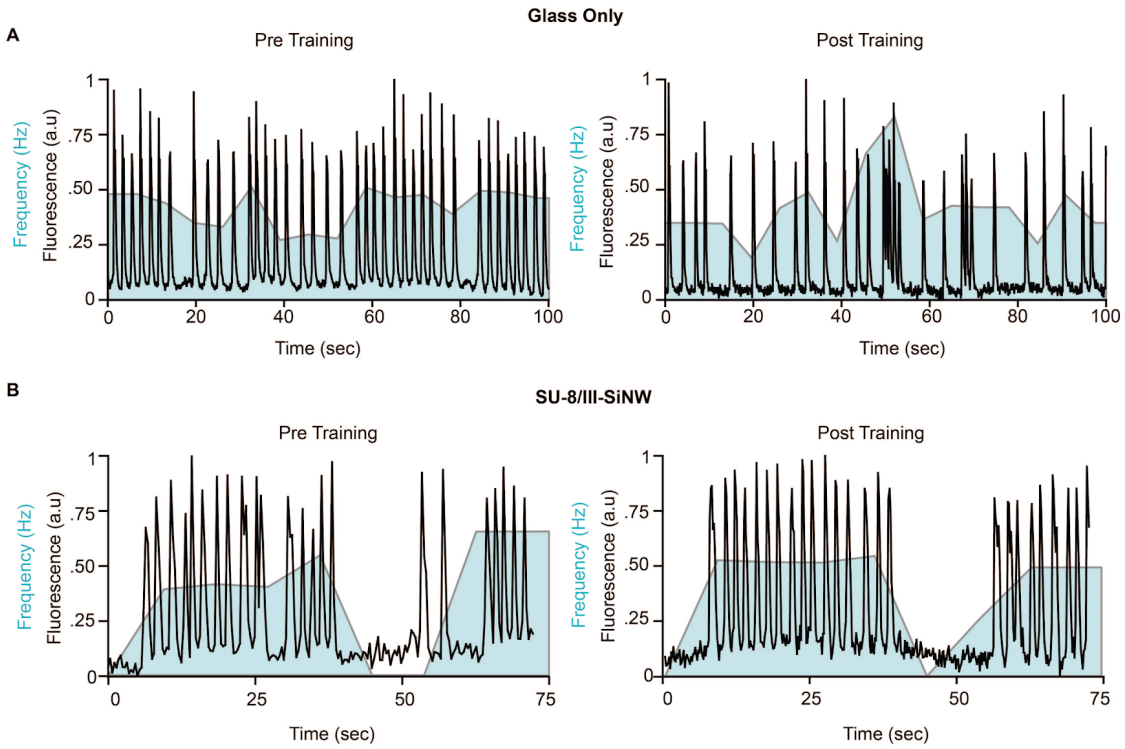

Figure 4.11. Optical stimulation of cardiomyocytes on SU-8 grids, glass, and SU-8/III-SiNW meshes do not result in training. (**A-B**) Fluo-4 calcium imaging traces (black traces) depicting pre- and post- training beating patterns for a single cell from groups of (**A**) 9 and (**B**) 8 cardiomyocytes that were trained to beat at 700 mHz for (**A**) 42.24 min (4 stimulation periods) and (**B**) 42.25 min (4 stimulation periods) of total stimulation time on fibronectin-coated (**A**) glass and (**B**) SU-8/III-SiNW mesh. A running average of frequencies every 18 seconds were plotted behind the black traces to show how consistently the cell was beating before and after the training (blue mountain plot). These are representative traces of 6 different experiments with a total of 65 cells for the glass condition and 5 different experiments with a total of 34 cells for the SU-8/III-SiNW condition.

Control samples that were cultured on either glass or SU-8 grid meshes with intrinsic Si core-shell nanowires (SU-8/III-SiNW) did not display training behavior to a

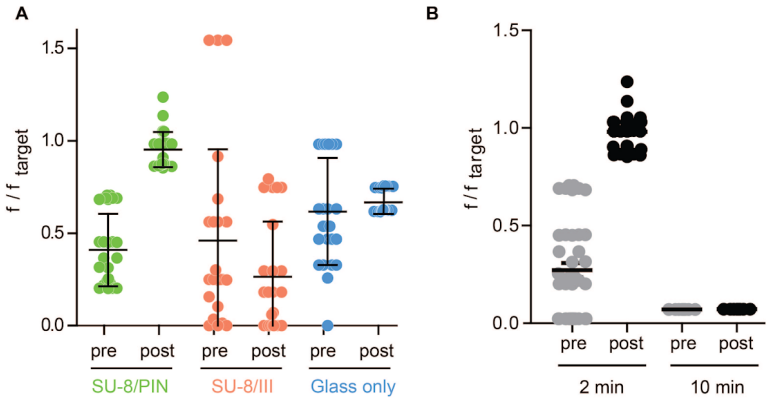

Figure 4.12. Comparison of optical stimulation of cardiomyocytes on various substrates and with various stimulation break times. (**A**) Comparison of optical training efficacy of cardiomyocytes cultured on fibronectin-coated SU-8/PIN-SiNW meshes (green), SU-8/III-SiNW meshes (orange), or glass (blue). Efficacy was determined by plotting the ratio of the beating frequency of individual cells (N=29 for SU-8/PIN-SiNW pre and post; N=23 for SU-8/III-SiNW pre and post; N=25 for glass pre and post) to the target beating frequency before and after optical training (pre and post, respectively). These values were taken from 4 separate stimulation experiments for the SU-8/PIN-SiNW condition in which cells were paced to 500, 700, or 1000 mHz; 3 for SU-8/III-SiNW condition that were all paced to 700 mHz, and 2 for the glass condition that were paced to 700 or 476 mHz. Points with the same values are sometimes overlaid. (**B**) Comparison of optical training efficacy of cardiomyocytes cultured on fibronectin-coated SU-8/PIN-SiNW meshes with different break times between training periods (2 min, 10 min). Efficacy was determined by plotting the ratio of the beating frequency of individual cells (N=45 for 2 min; N=8 for 10 min) to the target beating frequency pre- and post-optical training. These values were taken from 5 stimulation experiments for the 2 min condition in which cells were paced to 500, 700, or 1000 mHz, and 1 for the 10 min condition that was paced to 700 mHz. Points with the same values are sometimes overlaid. Averages and standard error for both graphs are indicated with a black horizontal line and black bars above and below average, respectively.

target frequency (Figs. 4.11-4.12). Non-scanning stimulation (*i.e.*, conventional single point stimulation) from SU-8/PIN-SiNW meshes can train cells towards the target

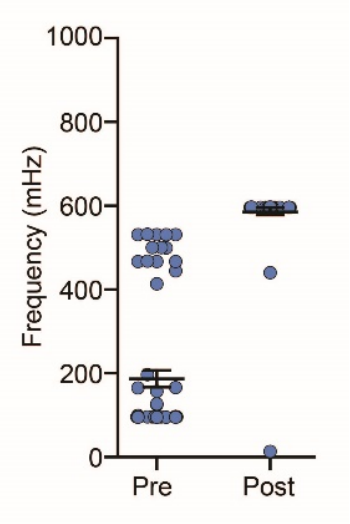

Figure 4.13. Non-scanning optical stimulation yields increase in beating frequency of cardiomyocytes, but not to the exact target frequency. Optical training of cardiomyocytes stained with Fluo-4 calcium dye and cultured on an SU-8/PIN-SiNW mesh. Here, a non-scanning 532 nm (3.33 mW power) laser was pulsed at a target frequency of 1 Hz with a 20% duty cycle. Pre-stimulation beating was recorded for 55.3 sec from cells that were going to be optically trained (N=56 cells) via calcium imaging. All frequencies were determined via Fourier Transform (see Methods). 12 min of optical training was performed and due to cytotoxicity in the stimulated region, post-stimulation beating frequencies were determined from a neighboring region (N=73 cells) via a 124.8 sec calcium imaging recording. Graphs displays pre- and post- stimulation frequencies for each cell. Averages and S.E.M. are indicated with a black horizontal line and black bars above and below average, respectively. Some points are overlaid.

frequency (Fig. 4.13) at a significantly higher radiant exposure (~ 44 mJ/cm^2 per pulse), but at the expense of light-induced cytotoxicity.

We next wanted to further characterize the 'memory' behavior of the cardiomyocytes by altering the break time (*i.e.*, black bars, upper inset of Fig. 4.9D) between stimulation periods. For example, we found that a break time of 10 min did not result in any training, but that the 2 min break time was effective (Fig. 4.9F, Supplementary Fig. 4.12B), which is reminiscent of the persistent increase in synaptic strength in natural[27] or artificial[28] memory formation. We lastly wanted to understand the

duration of the ‘memory’ effect by measuring cardiomyocyte beating long after the end of the optical training period. In a group of cardiomyocytes that were trained to beat at 500 mHz, the cells in and in close proximity (within ~ 300 μm radius) to the stimulated region maintained their trained 500 mHz beating frequency for 40 min after the last optical stimulus (Fig. 4.9G). At 45 min, the cells exhibited a slightly larger spread of frequencies with the average still being maintained near 500 mHz (Fig. 4.9G). These results demonstrate that our training approach is effective in inducing synchronization of cardiomyocyte beating to a target frequency and a cellular ‘memory’ of the learned beating frequency after the optical stimulus is removed. This ‘memory’ effect highlights the potential biomedical benefit of our approach, as other methods such as optogenetics[5] and IR optical stimulation[4] modulate target cells only when the light stimulus is present.

4.4 Optical training of isolated hearts

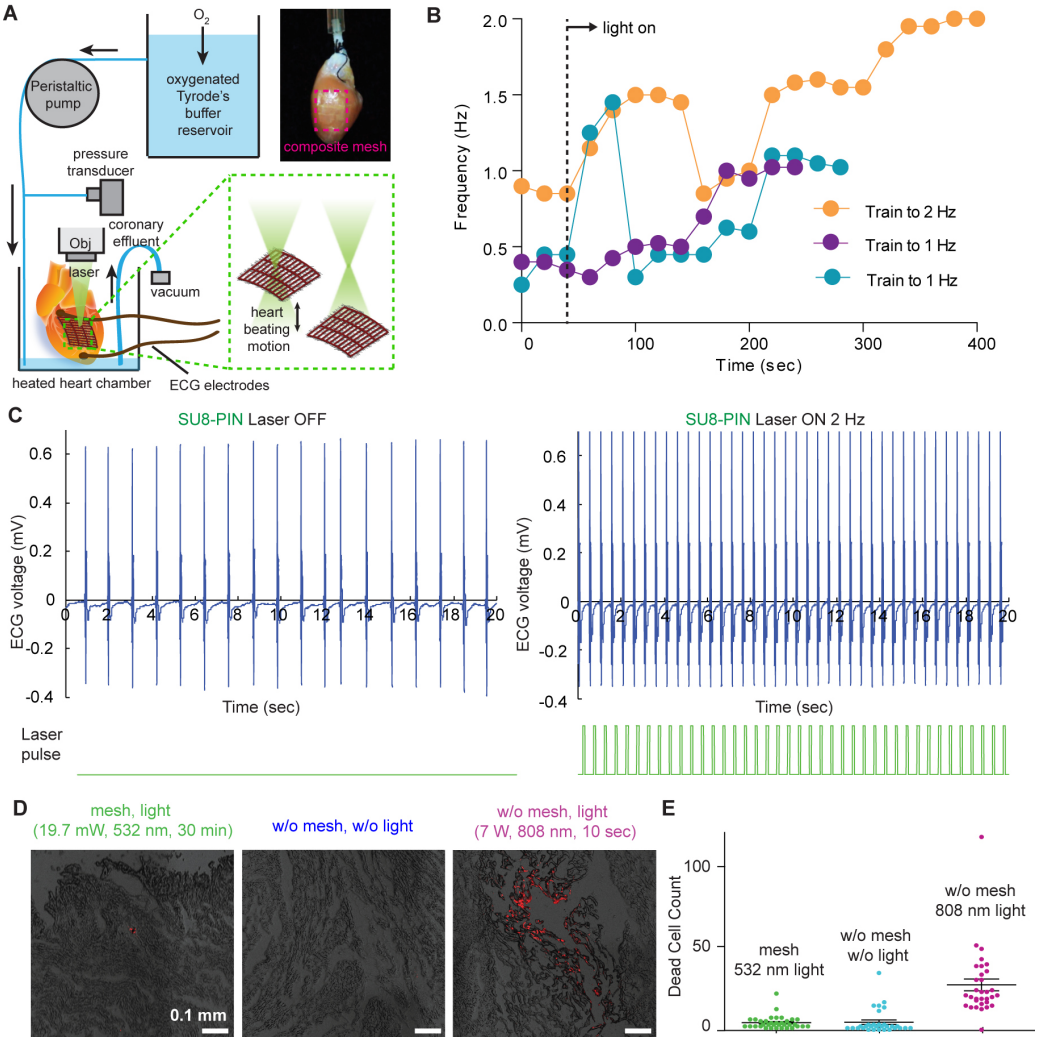

Figure 4.14. Optical training of isolated adult hearts. (**A**) Langendorff set up used to assess optical training of adult rat hearts. Oxygenated Tyrode's buffer reservoir was perfused into the aorta of an adult rat heart a chamber maintained at 37℃ and the perfusion rate of the buffer was controlled by a peristaltic pump. ECG electrodes were placed on the apex and aorta and both the perfusion pressure, which was transduced to a recordable signal through a transducer, and the ECG recordings were connected to an amplifier that was interfaced with a computer. A 532 nm laser was focused through a 5X objective around the SU-8/PIN-SiNW mesh (Red dashed box in the inset) placed onto exposed myocardium on the left ventricle without the use of adhesives or sutures. The movement of heart during beating yielded ~ 0.2 mm location variation of the mesh. (**B**) Beating frequencies of three different adult hearts, 40 seconds prior to being exposed to 532 nm laser light (first 2 points of each trace), and during exposure to 532 nm laser light (all other points in the traces). Dashed line indicates the time when laser

(Figure 4.14 continued) is on. Connections between dots do not represent real data and are just a way to guide the trend. (**C**) Electrocardiogram recordings from an adult heart with a SU-8/PIN-SiNW mesh, prior to (left) and during (right) training with 532 nm laser pulses at 2 Hz on the SU-8/PIN-SiNW mesh. Light pulses are indicated in green under the ECG traces (blue). This is a representative trace from N=5 different hearts and N=5 different experiments. (**D**) Assessment of phototoxic effects of laser stimulation of adult rat hearts. Adult rat hearts with SU-8/PIN-SiNW meshes pulsed with laser for 30 min at 3.5 Hz (19.7 mW, 532 nm), adult rat hearts alone without any optical training, and adult hearts pulsed for 10 sec at 3.5 Hz (7 W, 808 nm) laser to intentionally induce phototoxicity. Dead cells were stained with propidium iodide. Cryosectioning of 5 μm heart slices to a depth of 750 μm was performed and confocal imaging of the slices (DIC) is shown (red: dead cells). These images are representative of 3 different experiments for the mesh, 4 experiments for the heart alone, and 5 experiments for the infrared (IR) laser condition. (**E**) Dead cells were counted using the ImageJ particle counting macro from 2 different heart experiments with 34 slices, 2 different heart experiments with 32 slices, and 2 different heart experiments with 32 slices for the SU-8/PIN-SiNW mesh, heart alone, and IR laser conditions, respectively. Each point on the graph represents 1 dead cell count from 1 slice. Means and standard error are indicated on the graph with a black horizontal line and black bars above and below the average, respectively.

We then tested the uninformed search training approach (Fig. 4.1) in adult rat hearts *ex vivo* using a Langendorff setup (Fig. 4.14A). The epicardia of the hearts were removed in the left ventricle and a SU-8/PIN-SiNW mesh was placed onto the exposed myocardium (Fig. 4.14A). The mesh conformably wraps around and adheres to the wet curved surface of the myocardial tissue via capillary action without the need for sutures

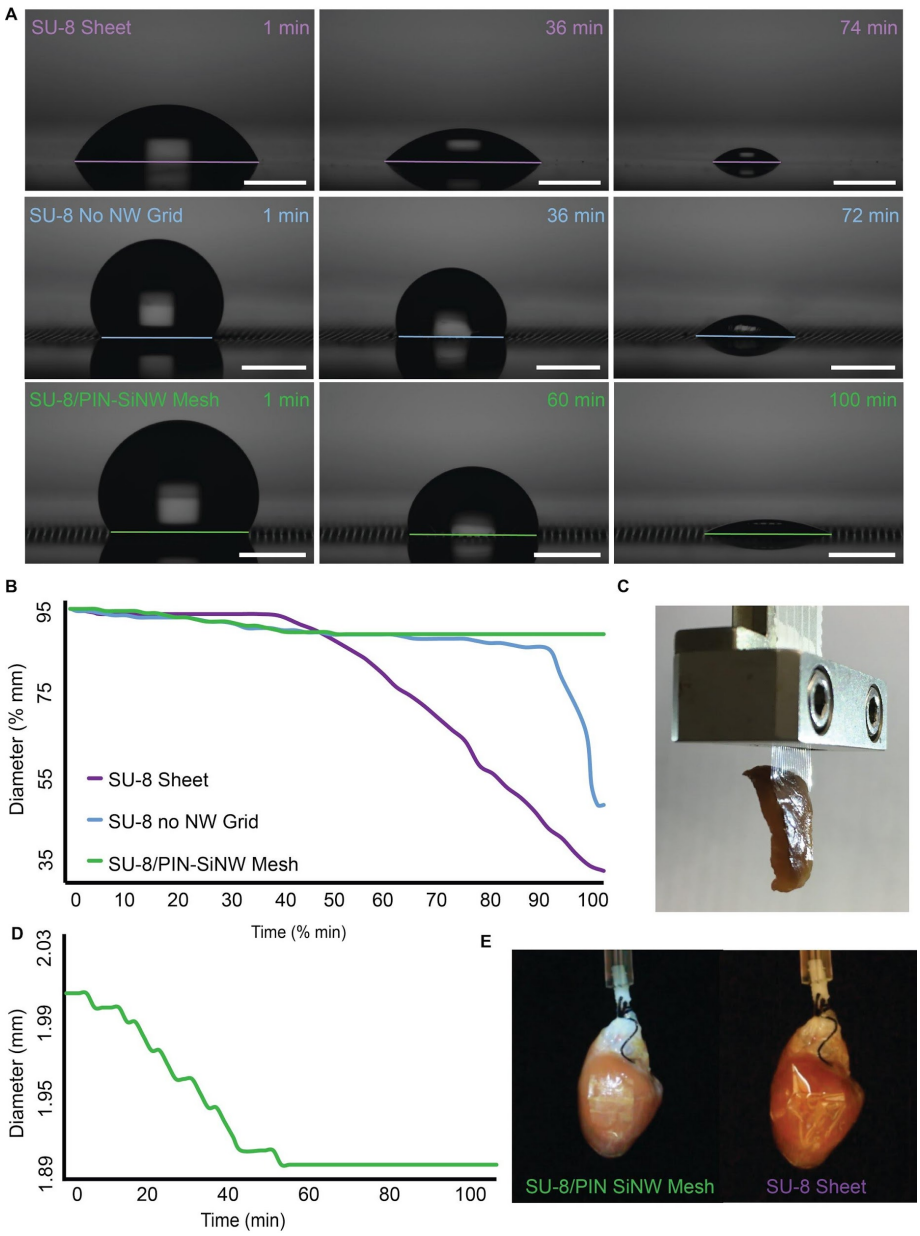

Figure 4.15. Water adhesion to mesh structure directs sutureless tissue adhesion. (**A**) Drying of 2-3 µL droplets of DI water on SU-8 sheet (purple), SU-8 grid (blue) and SU-8/PIN-SiNW mesh (green). Droplets on both the SU-8 grid and SU-8/PIN-SiNW mesh structures have a contact angle of ~120°. Drop diameters are indicated with horizontal lines colored according to the sample type. These images are representative of N=4 samples for each type of SU-8 structure. (Scale bars: 1 mm) (**B**) Droplet diameter during the drying process was plotted for an SU-8 sheet (purple trace), SU-8 grid (blue trace), and SU-8/PIN-SiNW mesh (green trace) as a function of time. Drop diameter and time are scaled by plotting the ratio of diameter/max diameter for each sample and time/max time for each sample. These traces are representative of N=4 samples for each type of SU-8 structure. (**C**) Tissue slice supported by SU-8 mesh structure solely *via* water-assisted adhesion. Wet tissue was brought into contact with

(Figure 4.15 continued) an SU-8/ mesh and was supported by mesh for at least 20 minutes. (**D**) Droplet diameter was plotted as a function of time for an SU-8/PIN-SiNW mesh (green trace), displaying the stepwise nature of droplet diameter change during the drying process due to the grid structure. This stepwise change cannot be seen when plotting the diameter as percentage in (**B**). (**E**) SU-8/PIN-SiNW mesh (green) and non-porous SU-8 sheet (purple) wrapped around an adult rat heart via water-assisted adhesion. The SU-8/PIN-SiNW mesh fully conformed and adhered to the heart surface. The SU-8 sheet showed folding, wrinkling, and slippage on heart surface due to reduced water adhesion properties.

or tissue adhesives (Fig. 4.14A). Contact angle experiments suggest that this observed phenomenon occurs as a result of increased water adhesion to both the SU-8 microstructure and the SiNWs in the mesh (Fig. 4.15).

In isolated hearts, unlike in cultured cells (Figs. 4.6 and 4.9), the fast-moving illumination interface was made possible by constant change of the sample locations due to the mechanical beating motion of hearts. A 532 nm laser (19.7 mW) was focused through a 5X objective onto the SU-8/PIN-SiNW mesh on the heart, and was set to pulse at the target training frequency via a waveform generator with a 20% duty cycle (Fig. 4.9A). The frequency of the beating heart was recorded via ECG electrodes that were placed on the apex and aorta of the heart. The fast variation in the laser spot location and intensity due to the contractile heart beating motion, as well as the intensity modulation from SiNW-enabled waveguiding, yielded an analogous situation to the aforementioned scanning laser stimulus (Figs. 4.6 and 4.9). However, in this case, the 'scanning' occurs due to the focus change, causing variations in optical stimulus intensities and locations hitting the heart (Fig. 4.9A).

We then assessed the efficacy of training hearts through optical stimulation of SU-8/SiNW mesh-covered hearts. We demonstrate training of hearts using SU-8/PIN-SiNW meshes to beat at various target frequencies (Fig 4.9B). We found that the path

to the target frequency was characterized not by a steady increase in frequency over time, but a series of slight rises and falls in frequency. The training ended in the target frequency over the span of ~4-7 min of light exposure (Fig. 4.9B). Representative results show training of one heart from a baseline of 0.9 Hz to the targeted 2 Hz after 5 min of 532 nm pulsed light exposure (Fig 4.9C). When we attempted to train hearts

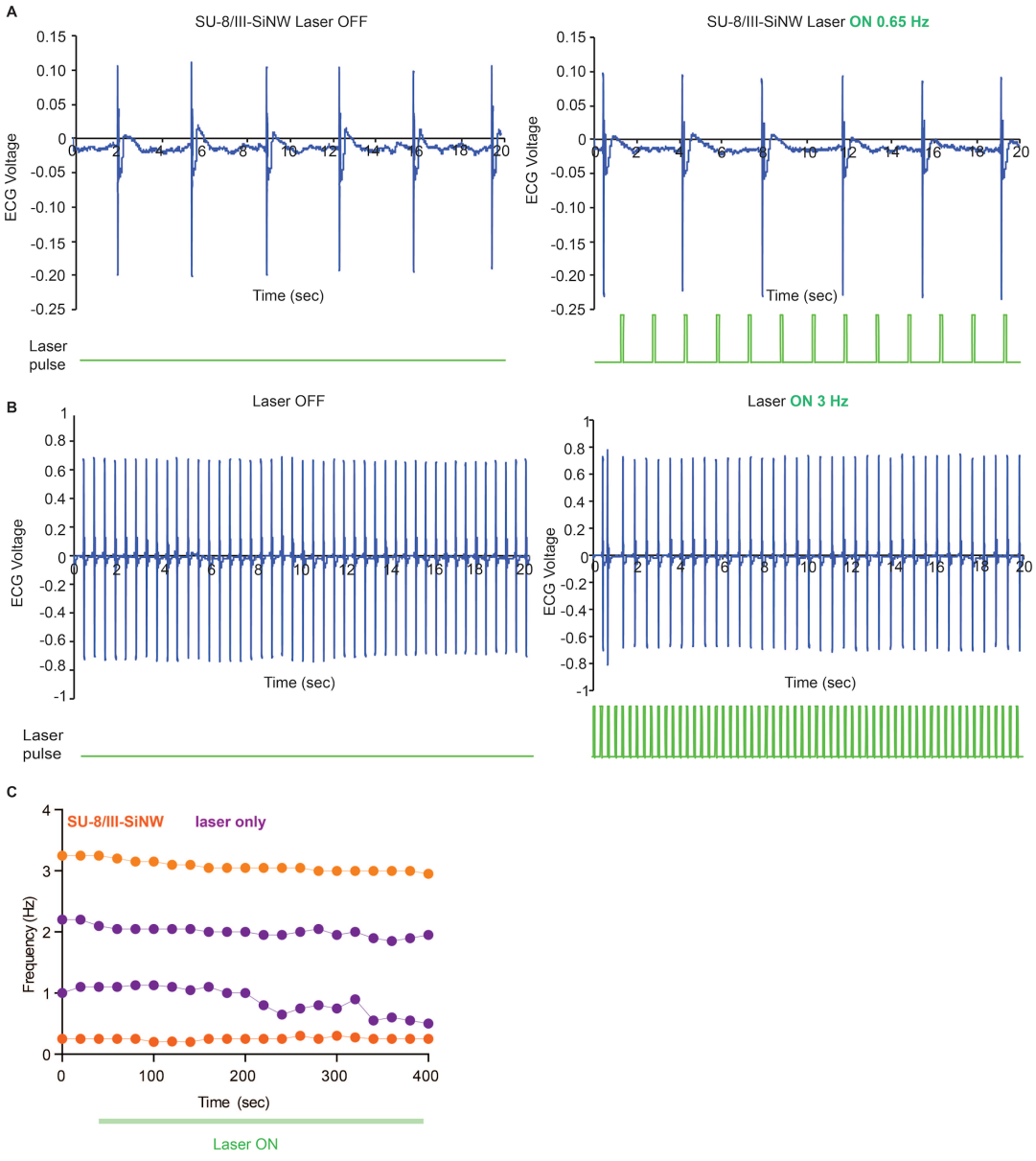

Figure 4.16. SU-8/III-SiNW meshes and light alone cannot induce optical training of adult rat hearts *ex vivo*. (**A**) Electrocardiogram recordings from an adult heart with an SU-8/III-SiNW mesh beating at 0.3 Hz prior to being exposed to 532 nm laser light

(Figure 4.16 continued) pulses (left) and during exposure to 532 nm laser light pulses at 0.65 Hz on the SU-8/PIN-SiNW mesh (right). Light pulses are indicated in green under the ECG traces (blue). These are representative traces of N=2 different hearts and N=3 different experiments. (**B**) Electrocardiogram recordings from an adult heart without any mesh beating at 2 Hz prior to being exposed to 532 nm laser light pulses (left) and during exposure to 532 nm laser light pulses at 3 Hz on the SU-8/PIN-SiNW mesh (right). Light pulses are indicated in green under the ECG traces (blue). These are representative traces of N=6 different hearts and N=6 different experiments (**C**) Beating frequencies of 4 adult hearts with SU-8/III-SiNW meshes (orange) or without any mesh (purple) at times zero and 20 seconds prior to being exposed to 532 nm laser light (first 2 points of each trace) and during exposure to 532 nm laser light (all other points in the traces). SU-8/III-SiNW mesh samples are being trained to 0.7 Hz (lower trace) and 4.5 Hz (upper trace). Light only samples are being paced to 2 Hz (lower trace) and 3 Hz (upper trace). Connections between dots do not represent real data and are just a way to visualize the trend.

using SU-8/III-SiNW meshes or light alone, we observed no successful training to the target frequency within a 6 min span of optical illumination (Fig. 4.16). These results demonstrate an easily implemented optical training method for hearts *ex vivo*, where constant mechanical motion of the contracting heart enables the uninformed search for variable illumination intensities and locations.

Lastly, we wanted to assess cytotoxicity in hearts that had been exposed to the pulsed light stimulus for 30 min using propidium iodide (Fig. 4.16D). We found that SU-8/PIN-SiNW mesh-covered hearts pulsed with 532 nm light at 3.5 Hz had an average of 4.17+/- 0.64 dead cells in a 1 mm^2 area in 34 heart slices in the region exposed to light, as compared to 4.41+/- 1.26 dead cells in a 1 mm^2 area in 32 control slices with no light exposure for 30 minutes. As a positive control for the dye, we exposed hearts to 7 W of 808 nm laser light pulsed at 3.5 Hz for 10 seconds and induced visible tissue death with an average of 26.06 +/-3.4 dead cells in a 0.68 mm^2 area in 32 heart slices in the region exposed to light**.** These results indicate that optical stimulation of the SU-8/PIN-SiNW mesh does not induce significant cytotoxicity in adult rat hearts.

4.5 Conclusions and Outlook

In summary, we have developed a flexible polymer-silicon nanowire mesh and an uninformed search-based optical training approach that together mimic the spatiotemporal multisite inputs in naturally occurring cellular signaling (Fig. 4.1A). This training approach is characterized by fast variation of both the optical stimulation intensity and position, yielding high modulation efficiency and a low radiance requirement. We use this biomimetic approach to optically train both cultured cardiomyocytes and intact hearts to beat at target frequencies, allowing for groups of cardiomyocytes to synchronize, and more importantly, to maintain their beating frequency at the target level long after the optical stimulus is removed – a feature that has not been revealed before. Our findings have implications for both fundamental multi-cell bioelectric studies and photo-responsive cardiac therapeutics in the clinic. Finally, this approach could also be improved by integrating machine learning algorithms, especially in the decision making step (*i.e.*, “Desired state?”, “Yes”, “No, additional training”, in Fig. 4.1B), for more precise and efficient biological modulation.

4.6 Experimental Methods

4.6.1 Nanowire synthesis

Coaxial p-type/intrinsic/n-type silicon nanowires (PIN-SiNWs) were synthesized as previously described by Parameswaran *et al.* using a gold (Au) nanocluster-catalyzed chemical vapor deposition (CVD) process[9]. During the nanowire growth, silane (SiH_4) was used as the Si reactant, diboron (B_2H_6, 100 ppm in H_2) as the p-type dopant, phosphine (PH_3, 1000 ppm in H_2) as the n-type dopant, and hydrogen (H_2) as the carrier gas. For the p-type core nanowire growth, SiH_4, B_2H_6, and H_2 were delivered at flow rates of 2, 10, and 60 standard cubic centimeters per minute (sccm), respectively. For the intrinsic Si shell (i-shell) deposition, SiH_4 and H_2 were delivered at 0.3 and 60 sccm, respectively. Flow of PH_3 gas was then added for the n-type outer shell deposition at a flow rate of 1.5 sccm. The core growth was carried out at 470°C at a pressure of 40 torr for 30 min. Prior to i-shell deposition, growth was paused in a vacuum for 20 minutes until the CVD furnace temperature was stabilized at 750°C in preparation for shell deposition. The shell depositions were performed at 750°C at a pressure of 20 torr for 15 min per shell.

Coaxial intrinsic/intrinsic/intrinsic-SiNWs (III-SiNWs), consisting of intrinsic Si cores and intrinsic Si shells, were synthesized using the same growth process as that of PIN-SiNWs, except with only silane and hydrogen carrier gas, and 30 min growth time for core growth and 30 min for shell deposition.

4.6.2 SU-8/SiNW mesh fabrication

SU-8 structures were fabricated using SU-8 2005 (MicroChem) permanent epoxy negative photoresist via photolithographic patterning. SU-8 precursor was deposited onto IPA and acetone-cleaned glass coverslips via a two-step spin coating (Laurell WS-650 Spin Coater) protocol: (1) 5 sec at 2500 RPM (2) 55 sec at 3500 RPM. Samples were pre-baked at 65°C for 180 sec and 95°C for 180 sec. PIN-SiNWs or III-SiNWs attached to their growth substrate were cleaned in a 10% HF solution for 90 sec, rinsed in DiH20, and dried under N_2 (g) in order remove the oxide layer. SiNWs were subsequently integrated into the pre-baked SU-8 precursor via mechanical translation. During mechanical translation, SiNW wafers were laid atop the SU-8 surface such that the SiNWs and SU-8 precursor were in direct contact and translated with light pressure across the surface. An EVG 620 semi-automatic double side mask aligner was used to photolithographically pattern samples using a quartz mask fabricated at Argonne National Labs with various grid patterns and 365 nm UV light source at a 175 mJ exposure dose. A post-exposure bake of the sample was subsequently performed at 65°C for 180 sec and 95°C for 180 sec. Samples were developed in SU-8 developer solution (MicroChem SU-8 Developer) for 30 sec and rinsed in isopropyl alcohol (IPA) for 15 sec. A final post-bake was then performed at 165°C for 20 min. Quality of 2 samples from each batch was assessed by a profilometer (Bruker Dektak XT-S Profilometer) to check that the height of the resultant SU-8/SiNW mesh was in fact 5 μm and that the mesh sidewalls were intact.

4.6.3 Drop Shape Analysis (DSA)

SU-8/PIN-SiNW meshes, SU-8 meshes, and SU-8 sheets were first lifted off of the glass slides they were fabricated on by wet chemical etching with a 48% Hydrofluoric acid (HF) (Fluka CAS# 7664-39-3) solution for 20 sec at room temperature. SU-8-structures were rinsed 6 times in 3 mL of DI water to remove all of the HF from solution. Samples were deposited onto acrylic scaffolds with a laser cut 6 cm diameter hole. Samples were then positioned above the hole and were loaded onto the drop shape analyzer (Kruss DSA100). Sessile drops of 2-3 µL were formed on the DSA needle above the SU-8 structures. Drops were brought into contact with the samples and the needle was pulled away to leave the drop on the surface of the sample. Contact angles were measured via the sessile drop method. At least 10 samples were measured from different synthesis batches to ensure consistency. Droplet pinning was analyzed by recording a video of the drying process of 2-3 µL sessile drops and tracking the contact angle and drop diameter to identify water pinning during droplet evaporation for each sample.

4.6.4 SU-8/SiNW mesh preparation for cardiomyocyte culture

SU-8/SiNW meshes were adhered to glass bottom petri dishes for cell culture. The glass surfaces were functionalized with (3-Aminopropyl) triethoxysilane (APTES) (Sigma-Aldrich CAS# 919-30-2)[29], followed by chemical crosslinking to the epoxy groups of SU-8[30]. Briefly, glass bottom petri dishes (Cellvis, 35 mm Glass bottom dish with 20 mm micro well #1 cover glass #D35-20-1-N) were plasma cleaned for 2 minutes (100 W). Plasma cleaned glass bottom dishes were coated with 1 mL APTES ((3-Aminopropyl) trimethoxysilane (Sigma Aldrich CAS# 13822-56-5) for 2 min to

functionalize the surface. SU-8/SiNW mesh samples were lifted off via the process described above for DSA measurements and transferred to functionalized dishes with the SiNWs oriented upwards. Chemical crosslinking of SU-8/SiNW meshes to APTES was achieved by heating dishes to 80°C, with a 5.5 g weight pressing the SU-8/SiNW mesh into the glass surface. SU-8 meshes in glass bottom culture dishes were sterilized under UV light for 24 hours and coated with human plasma fibronectin at a concentration of 0.5 mg/mL (ThermoFisher CAS# 33016015) for 2 hours at 37°C before being used for cell culture.

4.6.5 Cell culture protocol

Hearts were excised from P1 neonatal rats into HBSS without Ca^{2+} or Mg^{2+} (Fisher Scientific 14-175-145) on ice and washed 6 times to eliminate red blood cells. Atria were subsequently removed from each heart and remaining ventricles were minced into 3-4 pieces. Ventricles were incubated on a shaker overnight at 4°C in a 0.05 mg/mL trypsin solution (Worthington Biochemical TRL3 LS003708) in HBSS (Gibco 14175-079). They were then transferred to a 37°C water bath and the activity of the trypsin enzyme was inhibited with a 2 mg/mL soybean trypsin inhibitor solution in HBSS. Hearts were then further digested in 1 mg/mL collagenase type II (0.22 μm filtered) (Worthington Biochemical CAS# LS004202) in L15 medium (ThermoFisher 11415064) for 45 min in a 37°C water bath with manual shaking every 5 min. Gentle mechanical trituration of the digested hearts was next performed with a plastic pipette 10 times in a tissue culture hood. The resulting cells were passed through a 70 μm filter and incubated at room temperature for 30 min. Cells were then resuspended into cardiac culture medium (DMEM + 10% FBS + 100 U/mL penicillin + 100 μg/mL streptomycin)

(FBS: Gibco ThermoFisher 10437028; Penicillin-streptomycin: Thermo Fisher Scientific 10378016). Cells were then plated onto 10 cm tissue culture treated petri dishes in a 37°C 5% CO_2 incubator for 2 hours to exclude excess smooth muscle cells and fibroblasts from the cardiomyocyte culture. Cardiomyocytes from the supernatant were then plated at a concentration of 500000 cells/dish onto fibronectin-coated SU-8/PIN-SiNW meshes on glass bottom petri dishes.

4.6.6 Scanning electron microscopy

Cardiomyocytes were cultured onto the fibronectin-coated SU-8/PIN-SiNW meshes for 48 hours, and the media was changed at the 24-hour timepoint after seeding. Cultures were subsequently fixed with 4% paraformaldehyde (Sigma-Aldrich CAS# 30525-89-4) and stained with 1% osmium tetroxide (Sigma CAS# 20816-12-0) for 1 hour at room temperature. The samples were then dehydrated with increasing concentrations of ethanol and subsequently critical point dried before being sputter-coated with 8 nm of Platinum/Palladium metal. Images were taken on a Carl Zeiss Merlin FEI-SEM.

4.6.7 Immunofluorescence

SU-8/PIN-SiNW meshes were made with SU-8 precursor solution containing ~0.1 mg/mL Rhodamine B (Sigma Aldrich CAS# 81-88-9). Cardiomyocytes were cultured onto fibronectin-coated Rhodamine B SU-8/PIN-SiNW meshes on glass bottom petri dishes. After three days of culture, cells were fixed with 4% paraformaldehyde for 10 minutes, permeabilized with 0.2% Triton-X (Fisher Scientific CAS# 9002-93-1) solution for 5 minutes, and blocked for an hour with 3% BSA (Fisher Scientific CAS# 9048-46-8) solution. Samples were then stained with anti-cardiac Troponin I primary antibody

(Abcam ab47003) (1/400 in 3% BSA), and anti-Connexin 43 primary antibody (Millipore Sigma MAB3067) (1/100 in 3% BSA) overnight at 4°C. Cells were subsequently stained for 1 hr with AlexaFluor 594 goat anti-rabbit IgG secondary antibody (Molecular Probes #A11037) and AlexaFluor 488 goat anti-mouse IgG secondary antibody (Molecular Probes #A1101) in the dark for 1 hr at room temperature. Lastly, cells were stained with DAPI (Sigma Aldrich CAS# 28718-90-3) at room temperature for 5 minutes. Samples were visualized (cardiomyocytes on SU-8/PIN-SiNW mesh and neighboring cardiomyocytes on glass) on the Caliber I.D Confocal Scanning microscope using a 20 X (NA 0.5) objective. DAPI signal was recorded by a 405 nm laser, cardiac Troponin I staining by a 640 nm laser, Rhodamine 6G signal by a 561 nm laser, Connexin-43 staining by a 488 nm laser, and SiNWs in scattering mode with the 785 nm laser.

4.6.8 Cell viability assay

Cardiomyocytes cultured on either fibronectin-coated glass bottom petri dishes alone or glass bottom petri dishes with fibronectin-coated SU-8/PIN-SiNW meshes were stained, after 3 days of culture, with a LIVE/DEAD cell viability assay kit (ThermoFisher Scientific #L3224). Cells were imaged after staining for 45 min on the Leica SP5 confocal microscope with a 40X objective. 488 nm laser was used to visualize the live stain and 514 nm laser was used to visualize the dead stain. The numbers of live cells in culture on the mesh or on glass were counted visually. Cardiomyocytes optically trained on the SP5 confocal system for a total of 75 min were also stained for viability on either glass or the SU-8/PIN-SiNW mesh.

4.6.9 Optical training of cardiomyocytes

Cardiomyocytes cultured for 3 or 4 days were trained to beat at a target beating frequency using a Leica SP5 Laser Scanning Confocal Microscope. Cells cultured atop a fibronectin-coated glass bottom petri dish, SU-8/PIN-SiNW mesh, or SU-8/III-SiNW mesh were stained with Fluo-4 AM intracellular calcium dye (Fluo-4, AM, cell permeant Thermo Fisher #F14201) at a concentration of 0.1 μg/μl for 20 min at 37°C. Cells were subsequently washed twice in modified Tyrode's buffer (NaCl 132 mM, KCl 4 mM, $MgCl_2$ 1.2 mM, $CaCl_2$ 1.8 mM, HEPES 10 mM, glucose 5.5 mM, pH 7.4). Cells were then kept in 3 mL of modified Tyrode's buffer at 37°C incubator on the microscope stage for the duration of the experiments. The Argon laser line used for both recording and stimulation (*i.e.*, training) was set to 30% of the maximum power. Pre-stimulation cellular beating frequency was recorded via a 40X objective (NA 1.3) by a 488 nm laser to monitor Fluo-4 calcium flux prior to stimulation. The images were recorded at a frame frequency of 5.6 Hz. Alternatively, differential interference contrast (DIC) imaging can be used to monitor the beating frequency. Once the pre-stimulation frequency was calculated, the target beating frequency was set using the following criteria: (1) if the pre-stimulation beating frequency was consistent, then it must be lower than the target frequency (usually ~30-60% of the target frequency) and (2) if the pre-stimulation beating frequency was inconsistent, then the highest beating frequency in any given time interval must be lower than the target frequency. As an example, the stimulation pattern for optical training of cells to beat at a target frequency of 700 mHz will be described here. The target frequency was achieved via a series of "ON/OFF" cycles (see Figs 4.6-4.7 for the definition of 'ON' and 'OFF'). During stimulation, the 514 nm

laser (Argon ion air cooled continuous wave laser), was rastered at a frequency of 1,000 Hz (line scan rate) over the entire training area (512 x 350 pixels) line by line. The line repeat was set to 2 with unidirectional scanning. The measured power out of the 40X objective of the stimulation laser is 0.615 μW and the optical stimulation radiant exposure for each frame is ~1.3 mJ/cm^2. The stimulation durations in individual training periods ranged from 10-35 minutes. This range of training period durations was determined based upon the initial experiments, which demonstrated that training periods shorter than 7 min were not long enough to produce a noticeable increase in beating frequency and durations longer than 35 min resulted in decrease in cell health (*i.e.*, break times are necessary). After stimulation, a post-stimulation cellular beating frequency was determined by Fluo-4 calcium imaging in the same manner as the pre-stimulation recordings. Samples were then allowed to break for a defined period (*e.g.*, 2 min or 10 min). The full cycle of training (pre-stimulation recording, stimulation, and post-stimulation recording, break) was repeated 4-5 times, resulting in total stimulation times of 57-127 min. Variation in the number of cycles or total stimulation time to reach the target frequency was due to physiological variation in the cardiomyocyte cultures from one isolation to the next. Additionally during a given experiment, the length of each training period duration was determined by assessing the post stimulation beating frequency from the previous training period (*i.e.*, user feedback). For experiments assessing the effects of break time (Fig. 4.9F) between stimulation cycles, cardiomyocytes were not stained with Fluo-4 and instead recorded via DIC imaging.

4.6.10 Analysis of cardiomyocyte beating frequency

For all experiments in which cardiomyocytes were stained with Fluo-4 calcium dye, calcium oscillations, as measured by changes in Fluo-4 fluorescence intensity over a 107.8 sec (600 frames) time period before and after optical training periods (*i.e.*, "pre" and "post" stimulation measurements), from individual cells were normalized and plotted (raw traces). They were further analyzed with a Fast Fourier transform in Python according to the protocol outlined by Uhlen *et al.* in 2004[31]. The resultant frequencies calculated by the Fourier Transform algorithm were plotted as average frequencies over the 107.8 sec pre and post stimulation time periods as in Fig 4.9E-G. Moving Fourier Transforms were performed and displayed as mountain plots (Fig 4.9C) by applying a Fourier transform over a window of 100 points (18 seconds) with the returned frequency value plotted at the center of the window. The Fourier transform window is then shifted 50 points and calculated again resulting in a point plotted every 9 seconds on the mountain plot. All frequencies from each 18 second window for a single cell within a given pre or post stimulation recording period were also plotted as individual points in Fig 4.9D. For all experiments in which cardiomyocyte beating was recorded via DIC imaging, we determined beating frequencies by watching the recorded videos of the beating cells and counting the number of contractions each cell experienced during the duration of the video.

4.6.11 Non-scanning optical stimulation of cardiomyocytes with SU-8/PIN-SiNW mesh

Cardiomyocytes cultured for 3 or 4 days atop a fibronectin-coated SU-8/PIN-SiNW mesh were stained with Fluo-4 AM intracellular calcium dye (Fluo-4, AM, cell permeant

Thermo Fisher #F14201) at a concentration of 0.1 µg/µl for 20 min at 37°C. Cells were subsequently washed twice in modified Tyrode's buffer (NaCl 132 mM, KCl 4 mM, $MgCl_2$ 1.2 mM, $CaCl_2$ 1.8 mM, HEPES 10 mM, glucose 5.5 mM, pH 7.4). Cells were then kept in 3 mL of modified Tyrode's buffer at room temperature on the microscope stage for the duration of the experiments. Beating frequency was measured via a GFP fluorescence filter cube to monitor oscillations in Fluo-4 AM dye fluorescence on an Olympus BX-UCB upright microscope and Hamamatsu EM-CCD digital camera. Cardiomyocytes were trained to beat at a target beating frequency using a 532 nm DPSS laser (LaserGlow), not focused through an objective (spot size: 1.4 mm), at a power of 3.33 mW pulsing at the target beating frequency with a duty cycle of 20%. The radiant exposure of the laser stimulus was ~44 mJ/cm^2 per pulse. In order to assess changes in beating frequency due to the optical stimulus, calcium imaging measurements were taken before and after optical training (*i.e.*, "pre" and "post" stimulation measurements). Cells in various regions within a 4 mm radius were optically trained for total durations of 7 min, 12 min, or 30 min before recording a post-stimulation frequency.

4.6.12 Ex Vivo cardiomyocyte training with SU-8/SiNW mesh

Adult rats were heparinized (1000 IU/kg IP) and anesthetized using open-drop exposure of isoflurane in a bell jar configuration. Hearts were removed, placed in ice cold HBSS buffer, and the aortas cannulated in preparation for use in a Langendorff setup. Oxygenated Hepes-buffered Tyrode's solution (containing, in mM: NaCl 126, KCl 5.4, Glucose 10, Hepes 10, $MgCl_2$ 1, $CaCl_2$ 2, $MgSO_4$ 1.2, NaH_2PO_4 0.39; bubbled with 99.5% O_2; pH titered to 7.3 by 2M NaOH) was perfused through the cannulated aortas.

The perfusion was passed through a heating coil and bubble trap (Radnoti), and the hearts were placed in a water-jacketed beaker (Fisher Scientific) to maintain the temperature at 37°C. The perfusion rate was controlled by a peristaltic pump to obtain perfusion pressures of 80–100 mmHg (~10–15 ml/min), which were monitored using a BP-100 probe (iWorx). For ECG recordings, needle electrodes were positioned on the apex and aorta, and connected to a C-ISO-256 preamplifier (iWorx). Both recordings (ECG and perfusion pressure) were amplified using an IA-400D amplifier (iWorx) and interfaced with a PC using a DigiData 1550 digitizer with pClamp software (Molecular Devices). To lower the heart rate, the atria were removed. To allow for direct interaction of the SU-8/PIN-SiNW or SU-8/III-SiNW with the cardiomyocytes, a small portion (~20mm^2) of the myocardium was exposed by removing the epicardium using a scalpel. SU-8/PIN-SiNW or SU-8/III-SiNW meshes were lifted off glass slides, as previously described, and were deposited onto clean glass slides in a thin film of water with the SiNWs oriented upwards. These glass slides were brought into light contact with the exposed myocardium, allowing for the SU-8 structures to wrap around and stick to the heart via capillary adhesion; this transfer process ensures direct contact between the SiNWs and cardiomyocytes. Hearts were then trained to beat at a target frequency by focusing a 532 nm laser through a 5X/0.10 Olympus UIS 2 MPlanN objective onto the SU-8/SiNW mesh. A waveform generator was used to adjust the frequency of the laser pulses to the intended target frequency with a 20% duty cycle. ECG recordings were used to assess beating frequency of the hearts before and during optical stimulation.

4.6.13 Phototoxicity of heart slices

Adult rat hearts were set up on a Langendorff perfusion system as described above. Hearts with SU-8/PIN-SiNW meshes were optically trained for 30 minutes with a 532 nm laser at 19.7 mW power at a frequency of 3.5 Hz and a 20% duty cycle. Control samples were prepared in the same way (with removed epicardia but no mesh) and were either not exposed to laser light for 30 minutes or exposed to 10 sec of 3.5 Hz (20% duty cycle) pulsed infrared (808 nm) laser light at 7 W to induce visible cell death. All hearts were perfused with 30 μM propidium iodide (PI) solution for 20 min, as in Jenkins et al. 2013[32], to stain for dead cells. Hearts were subsequently washed with Tyrode's buffer for 40 minutes and placed into ice cold Tyrode's buffer. The regions of light exposure on the hearts were excised with scissors and embedded in Tissue-Tek O.C.T. (Sakura Finetek from VWR, cat#25608-930). The embedded tissue was then frozen in a 2-methylbutane dry ice bath, and stored at -80°C. Tissue was cryosectioned in 5 μm sections, collected every 50 (SU-8/PIN-SiNW mesh) or 100 μm (SU-8/PIN-SiNW mesh, control sample, infrared sample) to a total depth of 750 μm. Tissue sections were visualized on a Leica SP8 confocal microscope using a 10x objective (NA 0.4 dry) and a 561 nm laser line. Quantification of cell death was performed in ImageJ with a particle counting macro.

4.6.14 Finite-difference time-domain optical simulations

3D finite-difference time-domain (FDTD) simulations were preformed to calculate intensity profiles of waveguide modes in single and double SiNWs on the SU-8 substrate. The calculation domain and grid size were 16000 x 1200 x 550 nm^3 and 5 nm, respectively. The convolutional perfectly matched layer (cPML) was used as the

absorbing boundary condition. Single or double SiNWs with a diameter of 300 nm and a length of 16000 nm were positioned along the x-axis. The dielectric constant of Si was obtained by fitting the measured refractive index and extinction coefficient of bulk Si. The refractive index of SU-8 was set to 1.62. Then, dipole sources were introduced in the SiNW to excite waveguide modes. For the double SiNWs, the dipole sources were introduced in only 1 SiNW.

4.6.15 Finite-element method optical simulations

The 3D finite-element method (FEM) was used to calculate light absorption in SiNWs. The simulation domain was digitized by 10 x 10 pixels in which 1 pixel had a size of 303 x 303 nm^2. The horizontally-polarized Gaussian beam with a wavelength of 514 nm, a spot size of 520 nm, and an electric field of 1 V/m was incident to the center of a single pixel, and scanned across the domain. The diameter of a SiNW was set to 300 nm and the surrounding area was made to be water (refractive index is 1.33). Then, the absorption distribution was calculated by 1/2 $\mathbf{J}\cdot\mathbf{E}^*$, where **J** and **E** are the polarization current density and electric field, respectively. The refractive index and extinction coefficient of bulk Si at 514 nm were used in the calculation. In addition, by integrating the absorption distribution in each pixel (with a height of 400 nm), we plotted the 6 x 6 absorption matrix (absorption per pixel).

4.7 References

1. A. A. Faisal, L. P. J. Selen, D. M. Wolpert, Noise in the nervous system. *Nature Reviews Neuroscience* **9**, 292-303 (2008).
2. A. Kusumi, T. A. Tsunoyama, K. M. Hirosawa, R. S. Kasai, T. K. Fujiwara, Tracking single molecules at work in living cells. *Nature Chemical Biology* **10**, 524-532 (2014).
3. E. Cingolani, J. I. Goldhaber, E. Marban, Next-generation pacemakers: from small devices to biological pacemakers. *Nature Reviews Cardiology* **15**, 139-150 (2018).
4. M. W. Jenkins *et al.*, Optical pacing of the embryonic heart. *Nature Photonics* **4**, 623-626 (2010).
5. U. Nussinovitch, L. Gepstein, Optogenetics for in vivo cardiac pacing and resynchronization therapies. *Nature Biotechnology* **33**, 750-754 (2015).
6. I. Nitsan, S. Drori, Y. E. Lewis, S. Cohen, S. Tzlil, Mechanical communication in cardiac cell synchronized beating. *Nature Physics* **12**, 472-+ (2016).
7. Y. W. Jiang *et al.*, Heterogeneous silicon rnesostructures for lipid-supported bioelectric interfaces. *Nature Materials* **15**, 1023-1030 (2016).
8. Y. W. Jiang *et al.*, Rational design of silicon structures for optically controlled multiscale biointerfaces. *Nature Biomedical Engineering*, (2018).
9. R. Parameswaran *et al.*, Photoelectrochemical modulation of neuronal activity with free-standing coaxial silicon nanowires. *Nature Nanotechnology* **13**, 260-266 (2018).
10. J. L. Carvalho-de-Souza, B. I. Pinto, D. R. Pepperberg, F. Bezanilla, Optocapacitive Generation of Action Potentials by Microsecond Laser Pulses of Nanojoule Energy. *Biophysical Journal* **114**, 283-288 (2018).
11. T. I. Kim *et al.*, Injectable, Cellular-Scale Optoelectronics with Applications for Wireless Optogenetics. *Science* **340**, 211-216 (2013).
12. I. R. Minev *et al.*, Electronic dura mater for long-term multimodal neural interfaces. *Science* **347**, 159-163 (2015).
13. R. Chen, G. Romero, M. G. Christiansen, A. Mohr, P. Anikeeva, Wireless magnetothermal deep brain stimulation. *Science* **347**, 1477-1480 (2015).
14. S. Chen *et al.*, Near-infrared deep brain stimulation via upconversion nanoparticle-mediated optogenetics. *Science* **359**, 679-683 (2018).
15. K. Mathieson *et al.*, Photovoltaic retinal prosthesis with high pixel density. *Nature Photonics* **6**, 391-397 (2012).
16. N. Li *et al.*, Redundant and diverse intranodal pacemakers and conduction pathways protect the human sinoatrial node from failure. *Science Translational Medicine* **9**, (2017).
17. E. T. Roche *et al.*, Soft robotic sleeve supports heart function. *Science Translational Medicine* **9**, (2017).
18. D. Ghezzi *et al.*, A hybrid bioorganic interface for neuronal photoactivation. *Nature Communications* **2**, (2011).
19. A. Savchenko *et al.*, Graphene biointerfaces for optical stimulation of cells. *Science advances* **4**, eaat0351 (2018).

20. S. Shoham, D. H. O'Connor, D. V. Sarkisov, S. S. H. Wang, Rapid neurotransmitter uncaging in spatially defined patterns. *Nat. Methods* **2**, 837-843 (2005).
21. I. Reutsky-Gefen *et al.*, Holographic optogenetic stimulation of patterned neuronal activity for vision restoration. *Nature Communications* **4**, (2013).
22. A. B. Greytak, C. J. Barrelet, Y. Li, C. M. Lieber, Semiconductor nanowire laser and nanowire waveguide electro-optic modulators. *Applied Physics Letters* **87**, (2005).
23. J. C. Johnson, H. Q. Yan, P. D. Yang, R. J. Saykally, Optical cavity effects in ZnO nanowire lasers and waveguides. *Journal of Physical Chemistry B* **107**, 8816-8828 (2003).
24. H. G. Park *et al.*, A wavelength-selective photonic-crystal waveguide coupled to a nanowire light source. *Nature Photonics* **2**, 622-626 (2008).
25. D. J. Sirbuly *et al.*, Optical routing and sensing with nanowire assemblies. *Proceedings of the National Academy of Sciences of the United States of America* **102**, 7800-7805 (2005).
26. L. C. Katz, M. B. Dalva, Scanning laser photostimulation - a new approach for analyzing brain circuits. *Journal of Neuroscience Methods* **54**, 205-218 (1994).
27. A. J. Silva, Y. Zhou, T. Rogerson, J. Shobe, J. Balaji, Molecular and Cellular Approaches to Memory Allocation in Neural Circuits. *Science* **326**, 391-395 (2009).
28. Y. van de Burgt *et al.*, A non-volatile organic electrochemical device as a low-voltage artificial synapse for neuromorphic computing. *Nature Materials* **16**, 414-418 (2017).
29. Agnihotri, S., S. Mukherji, and S. Mukherji, *Immobilized silver nanoparticles enhance contact killing and show highest efficacy: elucidation of the mechanism of bactericidal action of silver.* Nanoscale, **5**(16), 7328-7340 (2013).
30. Ren, Y., et al., *A Simple and Reliable PDMS and SU-8 Irreversible Bonding Method and Its Application on a Microfluidic-MEA Device for Neuroscience Research.* Micromachines. **6**(12), 465 (2015).
31. Uhlen, P., *Spectral analysis of calcium oscillations.* Sci STKE (258), 15 (2004).
32. Jenkins, M.W., et al., *Optical pacing of the adult rabbit heart.* Biomedical Optics Express, **4**(9), 1626-1635 (2013).

Chapter 5: Optical modulation of T cell activation with PIN-SiNWs

5.1 Introduction

An estimated five to eight percent of the US population suffers from autoimmune diseases[1,2]. Current therapeutics used to treat autoimmune diseases include cytotoxic monoclonal antibodies and other non-specific approaches such as steroids that result in the destruction of the pathogenic target cells, but also healthy cells in the immune system[3]. Thus, it is critical to develop methods that can target only the cells involved in disease pathogenesis. One particular avenue for approaching autoimmune therapeutics involves the chemical inhibition of ion channels for immunosuppression[4-7]. Many of these studies have demonstrated that selective blockage of T cell potassium channels, which are key regulators of membrane voltage in T cells, can ameliorate disease in mouse models of multiple sclerosis, psoriasis, and type-1 diabetes[4-7]. Thus, studies that can help us gain a more complete understanding of how membrane potential can influence the ability of T cells to be activated through the T cell receptor (TCR) can be of great use in not only furthering our understanding of how T cell activation occurs but also potentially advancing current therapeutics for autoimmunity.

T cell activation is initiated by multivalent engagement of the TCR by MHC-peptide (pMHC) complexes presented on the surface of antigen presenting cells (APCs), which induces a highly orchestrated sequence of events at and near the plasma membrane[8,9]. The TCR itself does not possess cytoplasmic signaling domains, but is instead noncovalently associated with the CD3 multisubunit signaling apparatus, consisting of three dimeric units (TCR-CD3 complex)[8]. Upon TCR stimulation, Src family kinases (SFKs) such as Lck phosphorylate immunoreceptor tyrosine based activation

motifs (ITAMs) on CD3 subunits of the TCR-CD3 complex, promoting downstream signaling events such as Zap70 kinase phosphorylation, calcium influx, and ERK1/2 phosphorylation[10].

Previous studies have shown that different subsets of peripheral $CD4^+$ T cell subsets that differ based upon antigen experience exhibit different basal membrane voltages and distinct expression patterns of potassium channels that are known to regulate their membrane voltages[11]. Naïve CD4 T cells have the lowest basal membrane voltage, in comparison to effector memory and central memory T cells, both of which are antigen experienced[11]. Thus, researchers have hypothesized that membrane voltage can affect the ability of a T cell to be activated and that increased depolarization can make the threshold for activation higher, thus making it so that naïve T cells cannot be activated as easily as T cell subsets that have encountered antigen and are protected against activation by weak stimuli[11]. These studies are also correlated with the potassium channel expression in these various T cell subsets.

The two main types of potassium channels that regulate membrane voltage in T cells are Kv1.3 channels and KCa3.1 channels. Kv1.3 channels have been shown to regulate membrane potential and the driving force for Calcium signaling in human T cells and its expression has been shown to be upregulated 4-5 fold in activated effector memory T cells[,4,6,7]. KCa3.1 channels have been shown to be more dominant in human naïve or central memory cells for regulating membrane voltage and Calcium signaling. In the context of autoimmune disease, it was reported that chronically activated encephelitogenic myelin-reactive rat memory T cells upregulated Kv1.3 channels after activation with myelin antigens, while naïve T cells upregulated KCa channels[5].

While chemical inhibitors of potassium channels are promising for use in the clinic, the ability to specifically target T cells and even specific subsets of T cells can be extremely advantageous in the context of autoimmunity. Here, we aim to target PIN-SiNWs specifically to T cells or even specific subsets of T cells and modulate membrane voltage in those cells. We further aim to understand the mechanism of membrane voltage based modulation of T cell activation, specifically teasing out which signaling pathways downstream of the TCR are affected and even how the conformation of the TCR-CD3 complex itself is affected. Work by Dr. Francisco Bezanilla, has demonstrated that changes in the membrane electric field can cause functionally relevant movement of charged transmembrane residues in membrane proteins (*e.g.*, ion channels and GPCRs)[12]. While elucidating the structural organization of the TCR-CD3 complex has been difficult due to the lack of available structural characterization methods for large membrane protein complexes, it has been demonstrated that highly conserved charged residues in the transmembrane helices of the complex as well as basic residues on the CD3 cytoplasmic domains are crucial to complex assembly and signal transduction during T cell activation[8,12-15]. Moreover, Manolios *et al*. developed a core peptide sequence that could specifically disrupt electrostatic interactions between the T cell receptor (TCR) alpha chain and the gamma chain of CD3, and showed that this core peptide could act as an effective immunosuppressant in animal models of rheumatoid arthritis, diabetes mellitus, and other autoimmune diseases[12]. In our studies, we have devised of a method to target PIN-SiNWs specifically to T cells via surface functionalization of the nanowires with antibodies that can bind to T cells. We have developed a method to optically depolarize

populations of T cells and using flow cytometry, understand the effects of nanowire mediated depolarization on T cell activation through the TCR. Lastly, we hope to understand how the conformation of the TCR-CD3 complex itself is affected by membrane depolarization using Forster resonance electron transfer (FRET).

5.2 Labeling of PIN-SiNWs with T cell specific antibodies

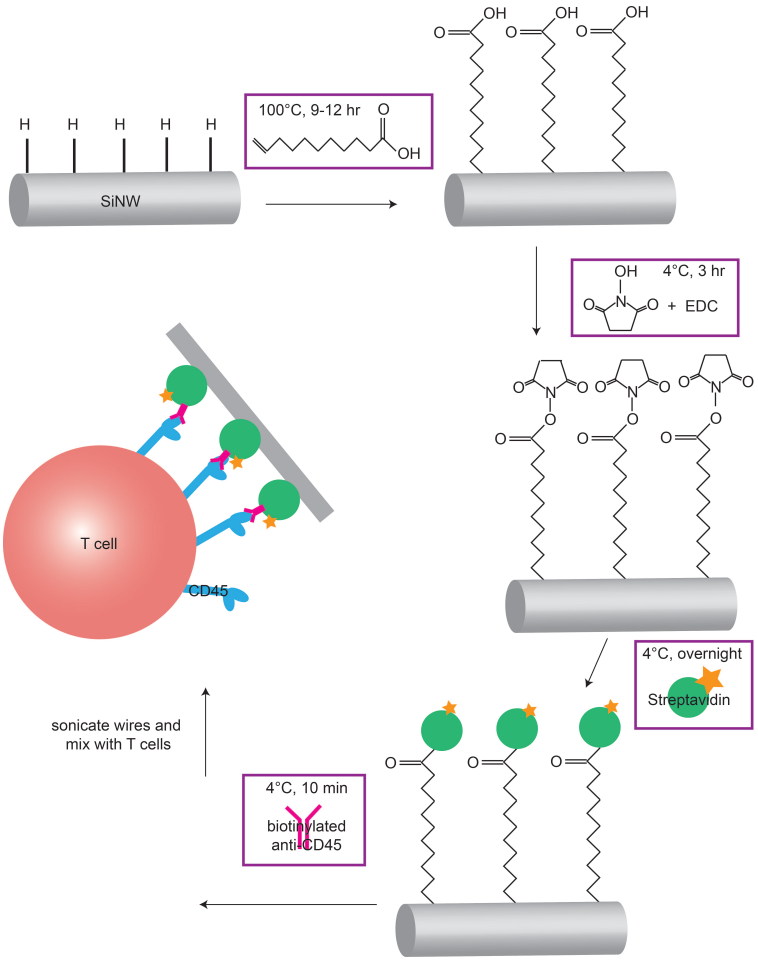

Figure 5.1. PIN-SiNW functionalization with Anti-CD45 antibody. Silicon nanowire surface functionalization scheme. Hydrogen-terminated nanowires (gray rod) undergo hydrosilylation with undecelynic acid at 100°C and then form an amine-reactive ester when incubated with EDC and NHS. Incubation with APC fluorophore-labeled (yellow star) streptavidin (green circle) at 4°C overnight allows for functionalization of the nanowires with Streptavidin-APC protein. Mixing these nanowires with T cells (pink circles) treated with biotinylated anti-CD45 antibody (pink antibody) allows for binding of the nanowires to the T cells via their surface CD45 proteins (blue).

Here, we have devised a surface functionalization scheme that can allow for highly specific binding of PIN-SiNWs to T cells based on work by Boukherroub et al.[16] In this scheme, we remove the native oxide layer from the PIN-SiNWs on their Si wafer substrate by incubating a nanowire wafer piece in 10% HF for 90 seconds and then rinsing in DI water for 10 seconds. We then hydrosilylate the hydrogen-terminated PIN-SiNWs with undecylenic acid under high temperature conditions (Fig. 5.1). Next, we incubate the nanowires with 1-ethyl-3-(3-dimethylaminopropyl) carbodiimide hydrochloride (EDC), which reacts with the carboxylic acid groups on the surface and forms an active and unstable O-acylisorurea intermediate that can form a dry-stable amine-reactive ester N-hydroxysuccinimide (NHS) intermediate with NHS, which is also included in the reaction (Fig. 5.1). Lastly, the nanowires are reacted with APC-labeled Streptavidin (StrA-APC), which has primary amino groups that can form amide bonds with the original carboxylic acid group from undecylenic acid and displace the NHS intermediate via nucleophilic attack (Fig. 5.1). In order to interface these StrA-APC labeled PIN-SiNWs with T cells, we then treat the nanowires with a biotinylated antibody that can bind to T cells, such as a biotinylated anti-CD45 antibody, and mix the T cells with the labeled nanowires (Fig. 5.1). The advantages of this method is that we are able to surface functionalize the nanowires without the need for an oxide layer on the nanowire (as is often needed in APTES surface modification methods), which can be counterproductive for the efficient production of photocurrents. Moreover, because we functionalize the nanowire surfaces with fluorescently labeled streptavidin, it is very easy to use any antibody to target any cell type. Thus, these nanowires are extremely versatile in terms of the cell types they can target. We also have shown that we can

treat the target cells with the biotinylated antibody and conjugate to StrA labeled NWs in that way as well, in case that is preferred for a future application.

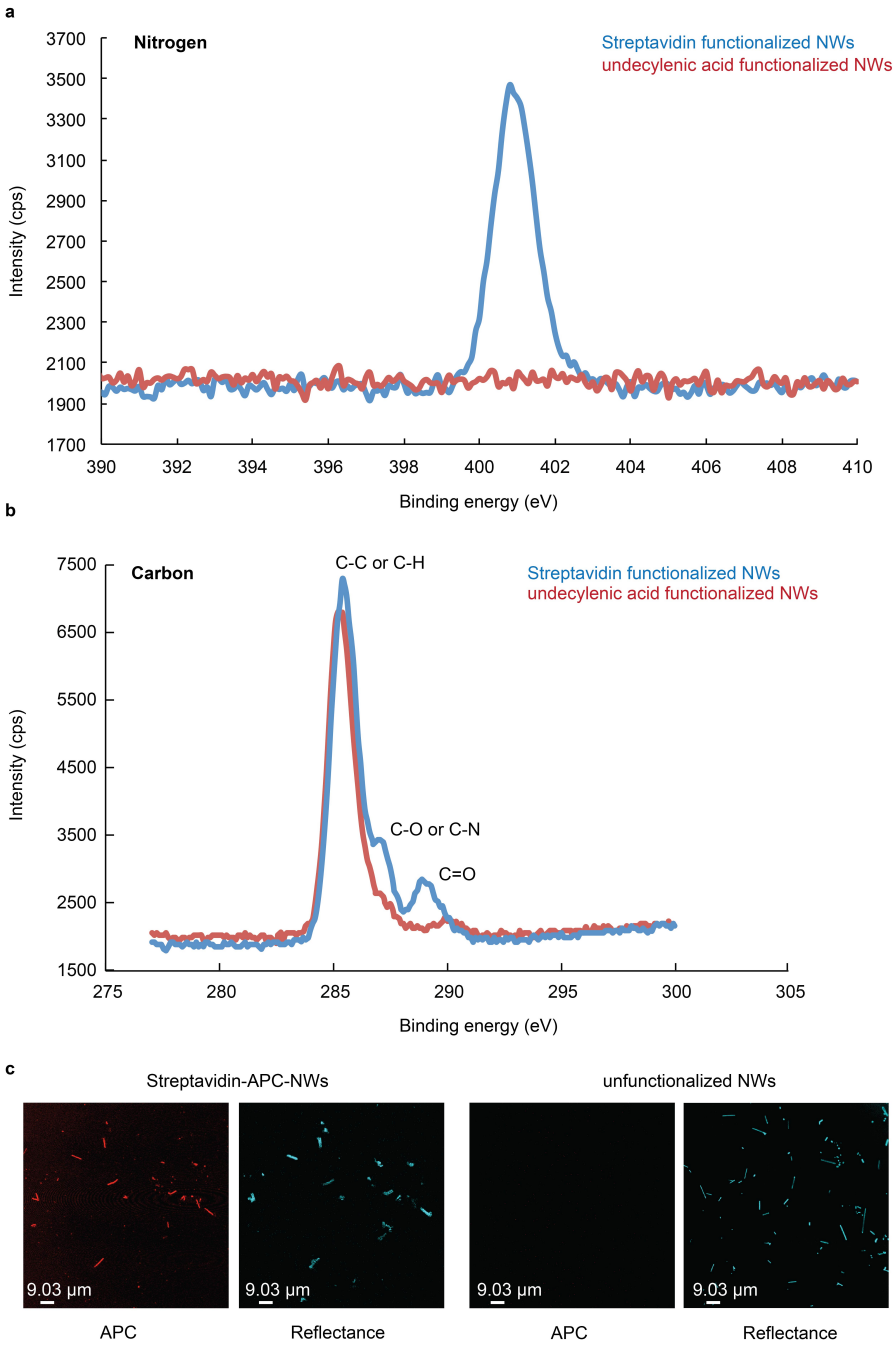

Figure 5.2. XPS and confocal microscopy demonstrate successful surface labeling of PIN-SiNWs with StrA-APC. (a-b) X-ray photoelectron spectroscopy of PIN-SiNWs attached to their Si wafer substrate, labeled with undecylenic acid only (red traces) or Streptavidin-APC (blue traces). Nitrogen **(a)** and carbon **(b)** traces are

(Figure 5.2 continued) displayed. **(c)** Confocal microcopy images of Streptavidin-APC labeled (left) and unfunctionalized (right) PIN-SiNWs. APC fluorescence and reflectance images are displayed, with reflectance showing all nanowires regardless of whether they are fluorescently labeled.

In order to confirm that the surface functionalization scheme was effective, we used X-ray photoelectron spectroscopy to understand the elemental composition of the nanowire surfaces at various stages in the labeling process. We found that a nitrogen peak at approximately 401 eV, which was absent immediately after hydrosilylation, appeared at the last stage of the functionalization scheme when the nanowires were labeled with StrA-APC (Fig. 5.2a). Furthermore, when comparing the carbon peaks at these two stages in the process, we found that all carbon peaks became more pronounced and that a C-O or C-N peak appeared at the StrA-APC stage, consistent with the idea that StrA is a protein and thus would have a more complex carbon profile via XPS (Fig. 5.2b). Furthermore, upon confocal microscopy imaging of unfunctionalized PIN-SiNWs and StrA-APC labeled PIN-SiNWs, we found that 100% of the labeled nanowires imaged positively for APC and that 0% of the unlabeled nanowires imaged positively for APC (Fig. 5.2c).

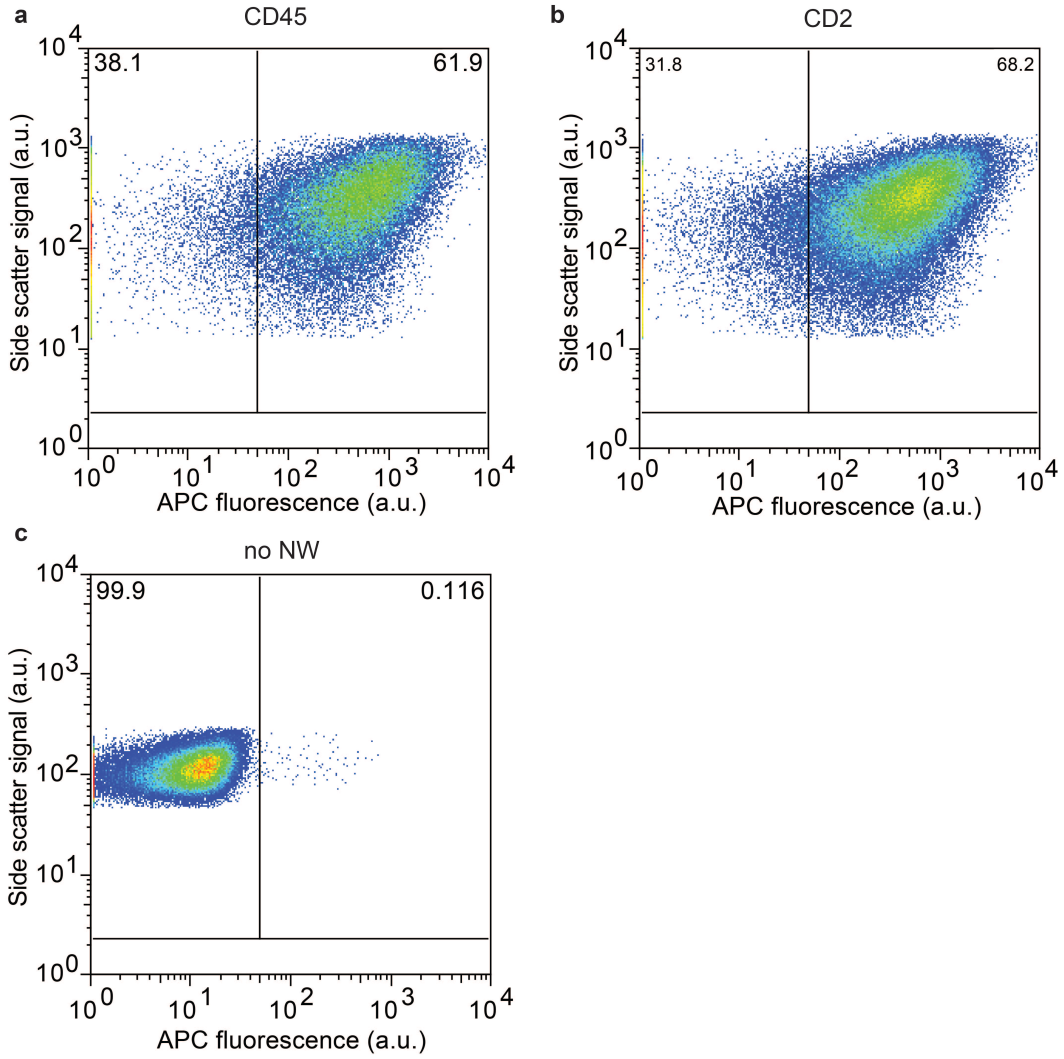

Figure 5.3. Generation of T cell-PIN-SiNW complexes. (a-c) Flow cytometry data displaying APC fluorescence (x axis) versus side scatter (y axis) for live 5cc7 Rag2 -/- mouse splenic T cells incubated with unlabeled nanowires (**a**), biotinylated anti-CD45 treated T cells incubated with a high concentration of Streptavidin-APC labeled nanowires (**b**), and biotinylated anti-CD45 treated T cells incubated with a lower concentration of Streptavidin-APC labeled nanowires (**c**).

We next wanted to show that the labeled nanowires could form complexes with target T cells. Here, we demonstrate that nanowires surface functionalized with APC labeled streptavidin (StrA-APC PIN-SiNWs) and were incubated with a biotinylated anti-CD45 or CD2 antibody can bind to T cells. We started by conjugating T cells with

nanowires via the phosphatase CD45, as it is excluded from the immune synapse, and an adhesion protein CD2, which is in the periphery of the immune synapse. We hypothesized that nanowires binding to T cells through these two proteins would have minimal effects on T cell activation. 99.9% of primary mouse splenic T cells incubated with unlabeled PIN-SiNWs were APC negative, while 61.9% of those T cells treated with anti-CD45 labeled nanowires and 68.2% of incubated with anti-CD2 labeled nanowires were APC positive (Fig.5.3a-c). We found these ratios to be very similar in Jurkat T cells as well (data not shown).

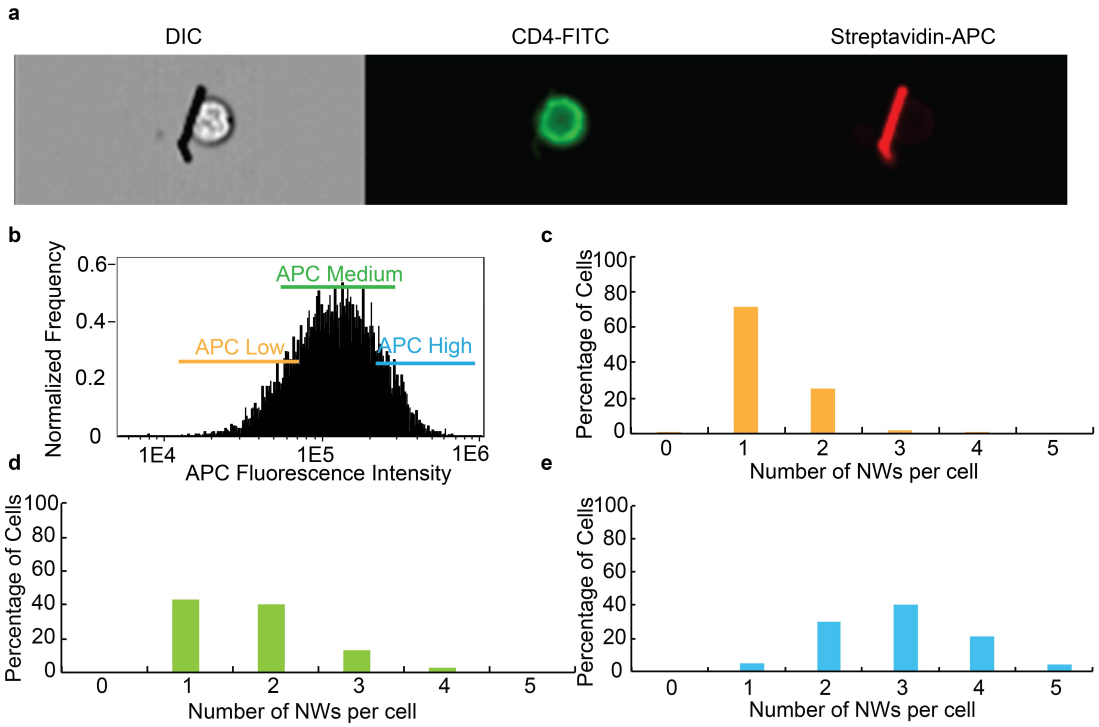

Figure 5.4. Imagestream flow cytometry reveals T cell-PIN-SiNW complexes with varying number of nanowires for each T cell. (a) Imagestream flow cytometry images of a biotinylated anti-CD45 treated Jurkat T cell incubated with Streptavidin-APC labeled PIN-SiNWs in DIC (left), FITC (middle), and APC (right). **(b)** Histogram of APC fluorescence intensity for 5cc7 Rag2 -/- mouse splenic T cells treated with biotinylated anti-CD45 and incubated with Streptavidin-APC labeled PIN-SiNWs split into APC low, APC medium, and APC high gates from the imagestream flow cytometer. **(c-e)** Bar

(Figure 5.4 continued) graphs detailing the percentage of cells attached to 0 to 5 nanowires in the images collected from the imagestream flow cytometer for the APC low gate **(c)**, the APC medium gate **(d)**, and APC high gate **(e)** from 400 cells.

Moreover, we used ImageStream flow cytometry technology to visualize these T cell-nanowire complexes and understand how many PIN-SiNWs were bound to each T cell on average, especially when the spread of the APC was larger. We found that we could easily visualize the nanowires bound to each T cell and that there was an APC fluorescence intensity dependent change in the average number of nanowires bound to each cell (Fig 5.4a-e). For the APC high population, we found that 4.8% of T cells were bound to 1 PIN-SiNW, 29.9% were bound to 2, 40.6% were bound to 3, 20.8% were bound to 4, and 3.9% were bound to 5 (Fig 5.4b-c). In the medium APC population, 43.5% of the T cells were bound to 1 PIN-SiNW, 40.5% were bound to 2, 13% were bound to 3, and 3% were bound to 4 (Fig 5.4b,d). In the low APC population, 0.99% of the T cells were not bound to any PIN-SiNWs, 71.2% were bound to 1, 25.6% were bound to 2, 1.48% were bound to 3, and 0.74% were bound to 4 (Fig 5.4b,e).

We next wanted to understand whether our T cell-NW conjugation system would allow for high specificity targeting of NWs to T cells, and even specific types of T cells, in a mixed population of cells. Thus, we acquired peripheral blood mononuclear cell (PBMC) samples from human patients and treated these cells with PIN-SiNWs labeled with StrA-APC alone, biotinylated anti-CD2, biotinylated anti-CD4, or a biotinylated isotype control. We added two blocking steps to improve binding specificity: (1) blocking with biotin after adding the biotinylated antibody and (2) blocking the PBMCs with

human serum before mixing them with the nanowires. We first assessed the percentage

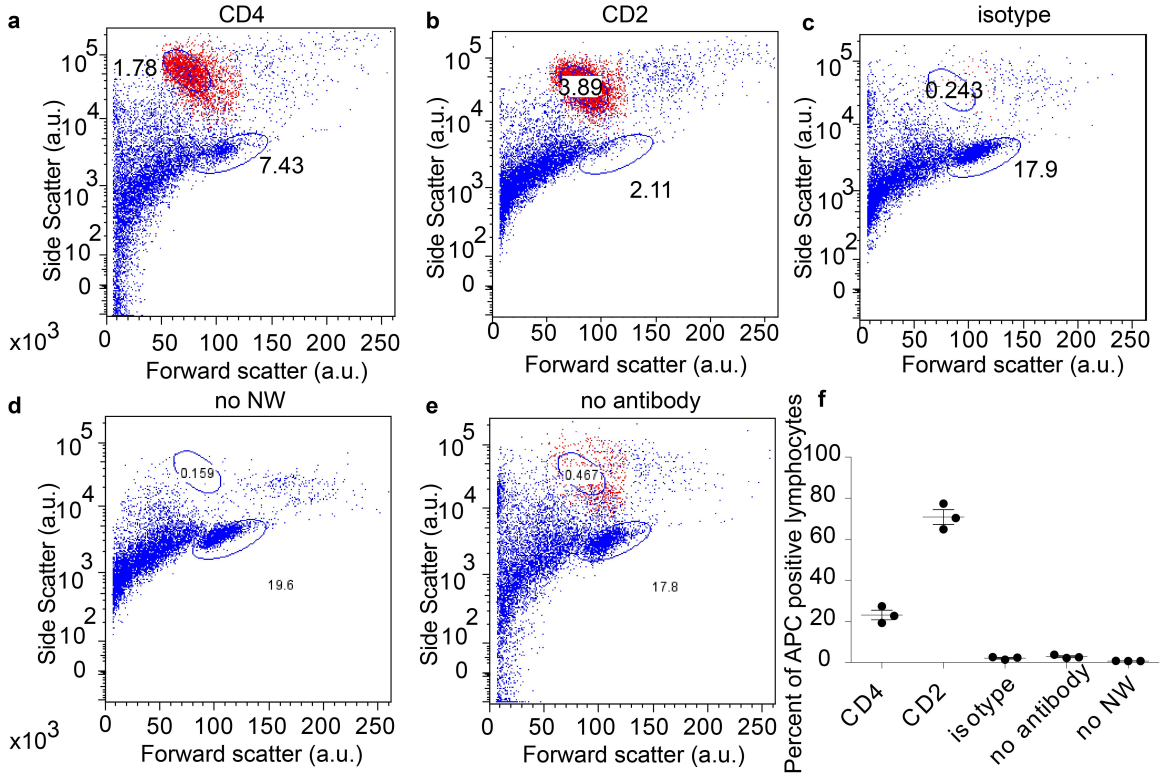

Figure 5.5 Antibodies confer cell type specificity for nanowire binding. Forward vs side scatter flow cytometry plots of PBMCs treated with **(a)** biotinylated anti-CD4 nanowires **(b)** biotinylated anti-CD2 nanowires **(c)** biotinylated isotype control nanowires **(d)** no nanowires **(e)** StrA-APC nanowires, showing APC positive lymphocyte population in red and other lymphocytes circled in blue. **(f)** Graph of the percentage of APC positive lymphocytes for each condition.

of APC positive (i.e. nanowire conjugated) lymphocytes for each condition (Fig. 5.5). We found that for the anti-CD2 (T and NK cell marker) condition, an average of 70.86% of lymphocytes were APC positive, and that for the anti-CD4 (only binds to CD4 T cells) condition, an average of 23.15% of lymphocytes were APC positive (Fig. 5.5a,b,f). These results are consistent with the idea that more lymphocytes are CD2 positive than CD4 positive due to the specificity of the markers. For the isotype control and no antibody (Streptavidin-APC only) conditions, the average percentages were 2.09% and

2.84%, respectively (Fig. 5.5c,e,f). For the no nanowire condition, the average percentage was 0.73% (Fig. 5.5d). These results demonstrate that the antibody conjugated to the nanowire confers cell type specificity. We further

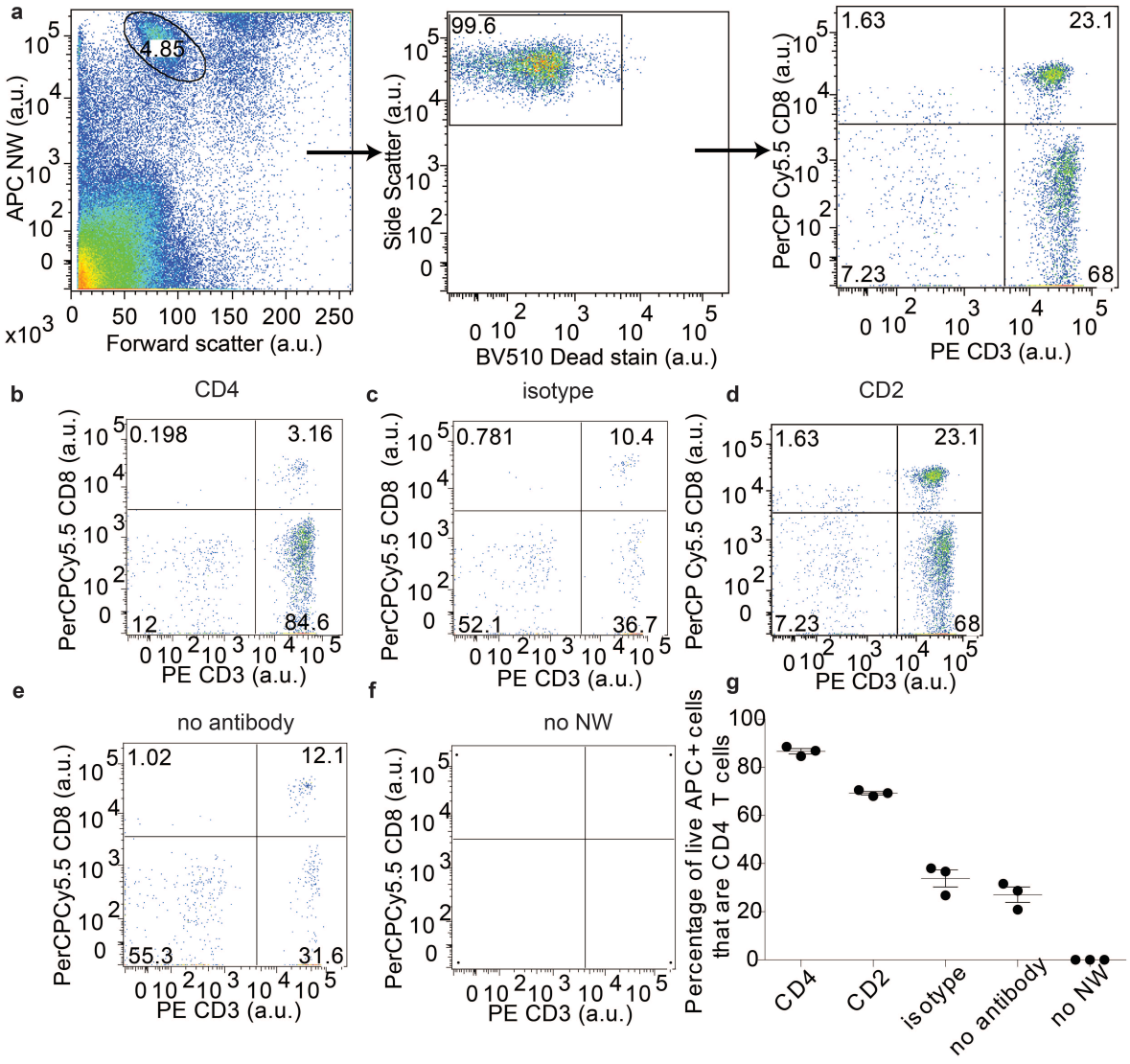

Figure 5.6 Anti-CD4 antibody confers nanowire specificity to CD4 T cells. (a) Flow cytometry gating scheme for studying specificity for CD4 T cells. (left) FSC vs APC fluorescence intensity (NW marker) with APC positive lymphocytes circled; (middle) live cells boxed based on low BV540 dead stain; (right) T cell populations distinguished by PE CD3 fluorescence (pan T cell marker) vs. PercPCy5.5 CD8 fluorescence (CD8+ T cells). CD3 vs. CD8 flow cytometry plots of APC positive live lymphocytes from PBMC samples treated with **(b)** biotinylated anti-CD4 nanowires, **(c)** biotinylated isotype control nanowires, **(d)** biotinylated anti-CD2 nanowires, **(e)** StrA-APC nanowires, or **(f)** no

(Figure 5.6 continued) nanowires. **(g)** Graph of the percentage of APC positive live CD4 T cells for each condition.

explored this specificity by analyzing the percentage of live APC positive cells that were CD4 T cells (Fig. 5.6a). We found that on average 86.67% of the APC positive live cells were CD4 T cells in the biotinylated anti-CD4 nanowire condition (Fig. 5.6b,g) and that 69.27% were CD4 T cells in the biotinylated anti-CD2 nanowire condition (Fig. 5.6d,g). For the isotype control, no antibody, and no nanowire conditions, the average percentages of APC live cells that were CD4 T cells were 33.83%, 27.07%, and 0%, respectively (Fig. 5.6c,e,f,g). These results indicate that there is some non-specific binding by the nanowires but that there is a significant amount of specificity that is conferred by the antibody labeling of the nanowires.

5.3 Optical modulation of T cell activation with PIN-SiNWs

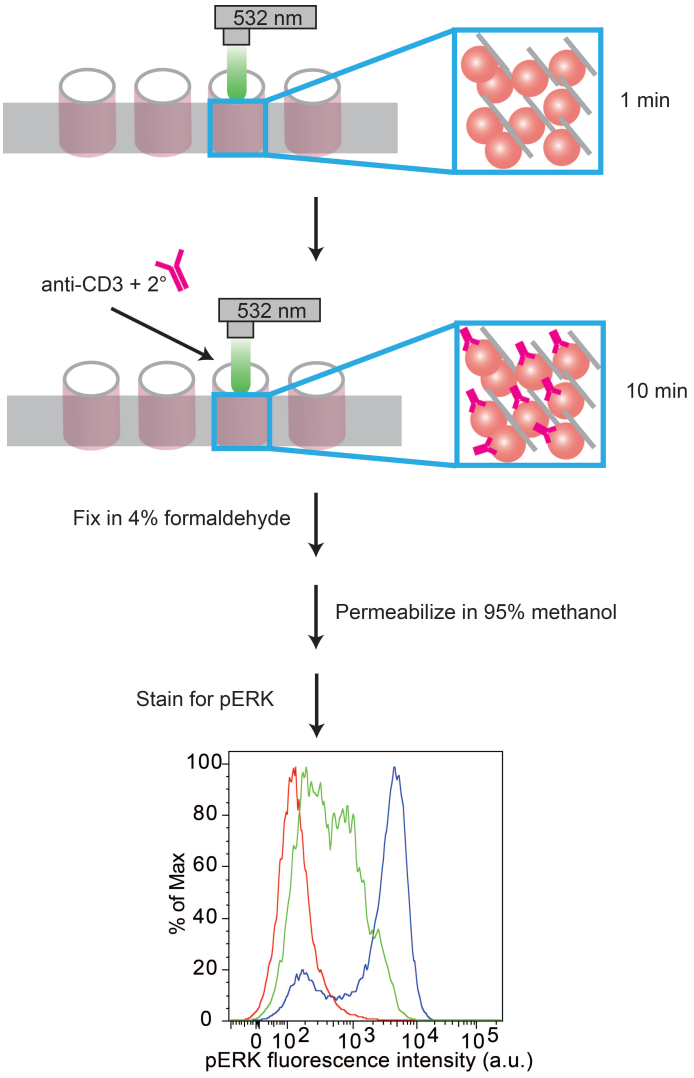

Figure 5.7. Scheme of PIN-SiNW mediated optical depolarization of T cells during T cell activation. Schematic of methodology used to optically depolarize T cells using PIN-SiNWs during T cell activation. T cell-nanowire complexes are plated in a well of a 96 well plate. A 532 nm laser is used to illuminate a single well for 1 min after which an anti-CD3 antibody with a secondary crosslinking antibody are added to the well. The laser is kept on with the stimulating antibodies for 10 min and fixed in formaldehyde to capture ERK1/2 phosphorylation. After permeabilization, the cells are stained with intracellular phosphoflow antibodies for ERK1/2 Thr202/Tyr204 phosphorylation.

Our previous work demonstrated that PIN-SiNWs can produce photoelectrochemical currents that can depolarize cell membranes and consequently,

we wanted to understand the effects of nanowire-mediated membrane depolarization on T cell activation[17]. We devised of a method to optically induce depolarization of populations of T cells complexed with labeled nanowires (Fig 5.7). We plated 100 µl samples of T cell-nanowire complexes in 96 well plates and used a 532 nm laser to illuminate single wells at a time for 1 minute at 40 mW with a power density of 4.26 mW/mm^2 before adding anti-CD3ε and a secondary antibody to the well to stimulate the TCR (Fig 5.7). We then maintain the 532 nm optical stimulus for 10 min or 90 sec in order to capture ERK1/2 phosphorylation events via intracellular phosphoflow cytometry (Fig 5.7). Prior to applying the light stimulus, we wanted to understand whether the

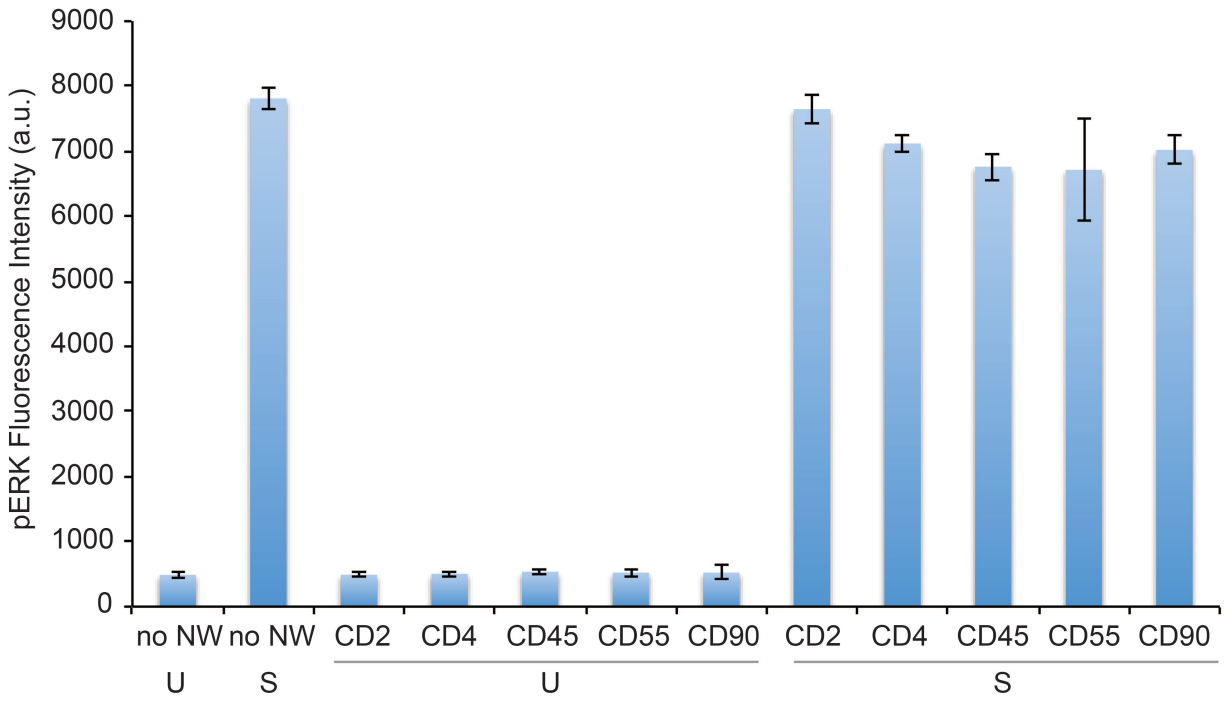

Figure 5.8. ERK1/2 phosphorylation upon TCR activation is not changed significantly by the presence of NWs. Jurkat T cells conjugated to PIN-SiNWs labeled with biotinylated antibodies (or not conjugated in no NW case) were either activated with 10 µg/mL OKT3 anti-CD3 antibody and 5 µg/mL of a goat anti-mouse secondary antibody crosslinker for 10 minutes (S) or left unstimulated (U). Cells were

(Figure 5.8 continued) fixed and permeabilized and stained for intracellular phospho-ERK1/2 to assess T cell activation. All antibodies used are expressed on T cells.

presence of the NWs alone had any effects on ERK1/2 phosphorylation. We found that when we labeled the NWs with a panel of biotinylated antibodies that can bind to T cells, including CD2, CD4, CD45, CD55, and CD90, the ERK1/2 phosphorylation levels in APC positive T cells was the same as in the no NW sample in the unstimulated condition (Fig. 5.8). When cells were stimulated through the TCR, slight variations in pERK levels were observed, but with no statistically significant differences (Fig. 5.8).

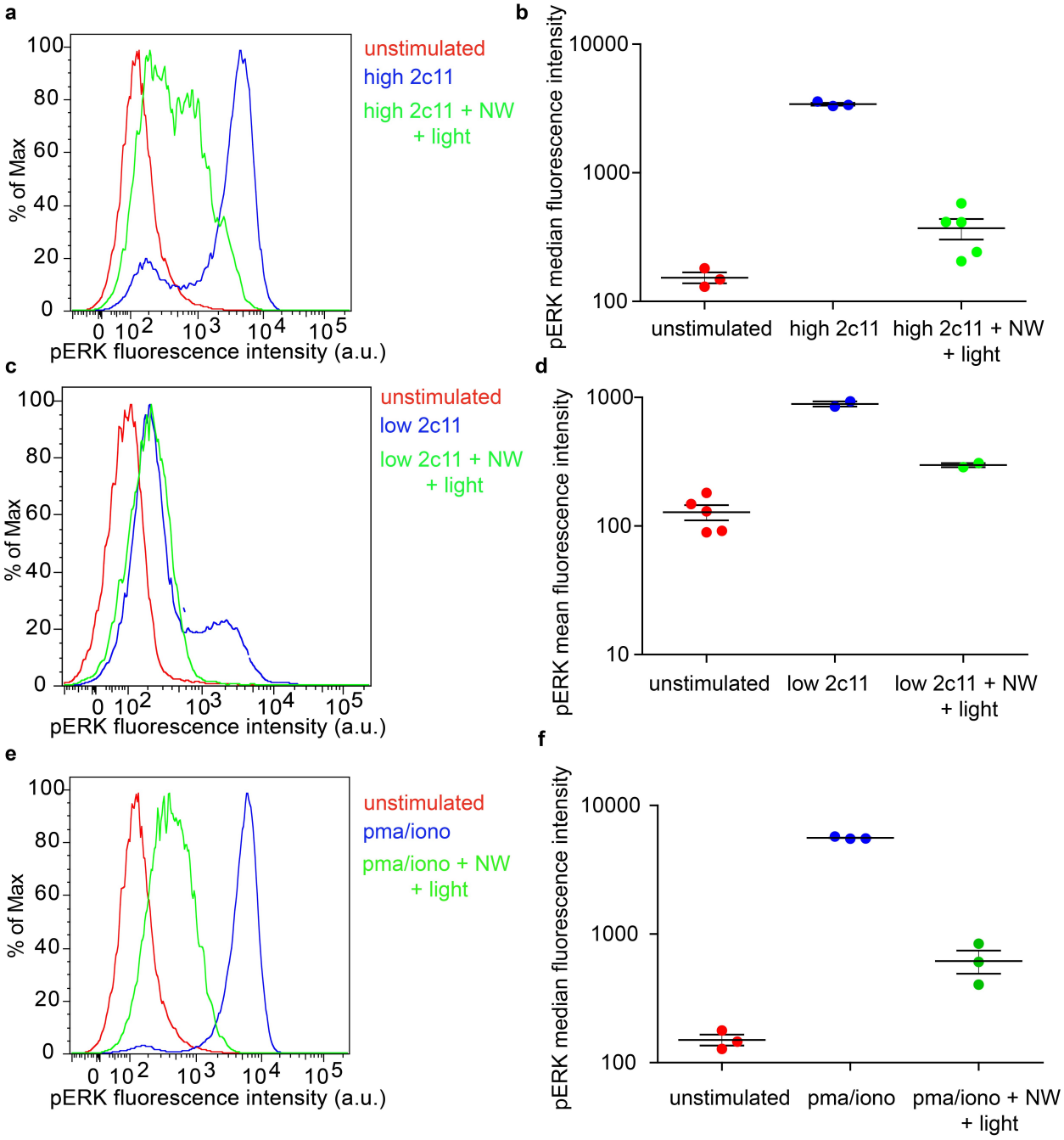

Figure 5.9. TCR activation induced ERK1/2 phosphorylation is dampened upon PIN-SiNW mediated optical depolarization. (a,c,e) Histograms of phospho-ERK1/2 FITC fluorescence intensity for 5cc7 Rag2-/- splenic T cells that were not stimulated (red traces), stimulated with 2c11 anti-CD3 antibody (blue traces) at 10 ug/mL **(a)** or 2.5 ug/mL **(b)**, stimulated with pma and ionomycin (blue trace) **(c)**, or stimulated with either anti-CD3 antibody or pma and ionomycin while being optically depolarized (green trace). **(b,d,f)** Corresponding phospho-ERK1/2 FITC median fluorescence intensity **(b,f)** or mean fluorescence intensity **(d)** of the histogram traces plotted with standard error bars for technical repeats of the experiments.

When measuring ERK1/2 phosphorylation in 5cc7 RAG2-/- mouse splenic T cells that had either been completely unstimulated, stimulated through the TCR with an anti-CD3 antibody (2c11 clone) or TCR stimulated while undergoing optical PIN-SiNW mediated depolarization, we found that ERK phosphorylation was significantly decreased to near unstimulated levels in the depolarizing condition in both high and low 2c11 concentration conditions (Fig. 5.9a-d). In the high 2c11 experiment, the average median fluorescence intensity for unstimulated samples was 153, 3417 for 2c11 stimulated samples, and 370.6 for 2c11 stimulated depolarized samples (Fig. 5.9a-b). In the low 2c11 experiment, the average mean fluorescence intensity for unstimulated samples was 128.02, 890.5 for 2c11 stimulated samples, and 298 for 2c11 stimulated depolarized samples (Fig. 5.9c-d). In order to further tease out whether this effect was completely TCR mediated, we activated T cells using pma and ionomycin, which bypass the TCR to activate PKC theta and induce calcium flux. We found that PIN-SiNWs similarly abrogate ERK1/2 phosphorylation during pma and ionomycin induced activation (Fig. 5.9e-f). In this experiment, the average median fluorescence intensity for unstimulated samples was 153, 5694.7 for 2c11 stimulated samples, and 628 for 2c11 stimulated depolarized samples (Fig. 5.9c-d). Laslty, we wanted to be sure that any effects we were observing were not due to cell death from the laser stimulus. Thus, we performed a LIVE/DEAD assay on samples with or without various types of laser stimuli (Fig. 5.10). We found that percentages of live cells did not vary for optically stimulated samples versus non-optically stimulated samples (Fig. 5.10).

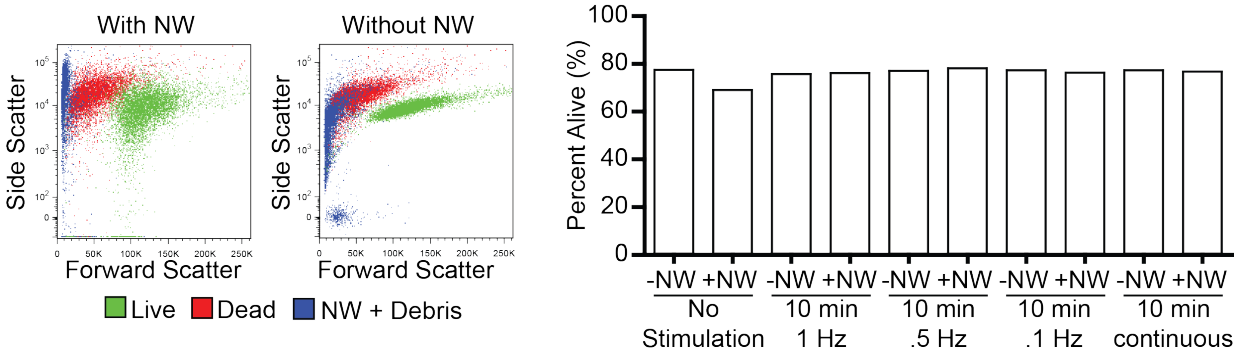

Figure 5.10. Optical stimulation does not affect T cell viability. Jurkat T cells with and without biotinylated anti-CD45 labeled nanowires were stained with a LIVE/DEAD kit after no optical stimulation or being optically stimulated for 10 min either using a continuous laser beam, a 1Hz frequency pulse, a .5 Hz frequency pulse, or a .1 Hz frequency pulse. (left) Sample flow cytometry plots of cells with and without labeled nanowires showing where the live and dead cells exist on the forward and side scatter plot. (right) Bar graph indicating percentage of live cells for each optical condition for cells with and without nanowires.

5.4 Conclusions and Outlook

Taken together, these results show that the generation of free-standing T cell-PIN-SiNW complexes is possible and that T cell depolarization during activation can dampen T cell activation significantly. Further studies elucidating the effects of this depolarization on the activation of T cells with various peptide-MHC stimuli, different T cell subsets, as well as on the conformation of the TCR-CD3 complex need to be conducted.

5.5 Experimental Methods

5.5.1 Nanowire labeling

Add undecenylic acid to a round bottom flask (enough to cover the nanowire chip later ~30 mL) and melt over a hot mineral oil bath at 50°C. Add the nanowire chip to the melted undecylenic acid and place the condenser over it. Add a condenser to the the round bottom flask set up and place the flask under N_2 gas. Next, perform the following freeze, pump, thaw procedure once without the nanowire chip and twice with it. Place the flask and condenser into an acetone/dry ice bath and let cool for a few minutes. Switch the Schlenk line to the vacuum and wait until the undecylenic acid freezes completely. Wait for 5 minutes after it is frozen and then return the flask to the oil bath. Cut a piece of a PIN-SiNW wafer to a desired size. Etch the chip for 90 seconds in 10% HF to remove the oxide layer and wash in DI water for 10 seconds. Dry with nitrogen gas. Place chip into the flask and repeat the Freeze, pump, and thaw procedure twice more. Heat the chip in undecelynic acid in an oil bath at 100°C. Let the undecylenic acid cool and wash the chip twice with acetic acid. Heat the chip in acetic acid in an oil bath to 75°C for 90 minutes with the condenser. Let the flask cool and wash the chip 4-5 times with DI water to ensure that there is no residual acetic acid. Dry the chip under N_2 gas. Place the chip in a solution of 5 mM EDC/10 mM NHS in DI water for 3-5 hours at 4°C. Wash the chip in DI water 2-3 times and add the APC-labeled Streptavidin at 20 µg/mL at 4°C for 12 hours.

5.5.2 Nanowire conjugation to cells

Nanowire chip functionalized with APC labeled streptavidin was removed from the fridge and cut into a size appropriate for the number of samples to be used. The cut chip was

washed with PBS and dried with N2 gas. The chip was then placed in an eppendorf tube and treated with 100 uL of the biotinylated antibody of choice by pipetting a 1:200 dilution of the antibody in PBS into the tube. The tube was wrapped in Aluminum foil and placed in the fridge for 10 minutes. The antibody solution was then removed and the chip was washed with PBS twice. The chip was then treated with 100 uM biotin as a blocking step at room temperature for 15 minutes. The chip was subsequently washed twice with PBS and sonicated in modified Tyrodes buffer until milky (1-2 minutes on highest setting). Cells (T cells or PBMCs) were counted and blocked in 3% human or fetal bovine serum in PBS or human and mouse cells, respectively, for 20 minutes at room temperature. Cells were then centrifuged at 200 g for 5 minutes and washed once with PBS. They were then resuspended in the sonicated nanowire solution and allowed to sit in a cell culture incubator for 10 minutes before use.

5.5.3 Flow cytometry and Imagestream of T cell-NW complexes

For PBMC assays, cells conjugated to nanowires were stained with the BV520 dead stain, anti-CD3 PE, anti-CD8 PercPCy5.5 antibodies for 30 minutes at room temperature in the dark. They were then centrigured at 100 g for 10 minutes and washed once with PBS before being resuspended into 200 uL PBS per sample for flow cytometry. The LSR-II 3-8 and Fortessa HTS were used for all flow experiments. For imagestream assays, cells were resuspended into 50 uL of modified Tyrodes buffer and run on the Amnis ImageStream-XBD Accuri C6 instrument.

5.5.4 T cell activation assays

For T cell activation assays, T cell-NW conjugates were prepared as mentioned above. They were then plated into 96 well plates (100 uL/well) and antibody stimuli were prepared. For Jurkat T cells, OKT3 antibody at 10 ug/mL (high) or 5 ug/mL (low) was used in soluble form and goat anti-mouse secondary antibody (Jackson ImmunoResearch) was used as a crosslinker. For mouse T cells, 2c11 anti-CD3 antibody was used at the same concentrations above and anti-Armenian hamster antibody was used for the secondary crosslinker. For activation, the OKT3 or 2c11 was added and mixed with the cells and the secondary added 20 seconds later and mixed. Cells were then fixed in 4% formaldehyde for 15 minutes at room temperature after ten minutes of stimulation time. Cells were topped with PBS and subsequently centrifuged at 200 g for 5 minutes and resuspended in 200 uL methanol/well that was added dropwise while vortexing. Cells were then stored in methanol at -20°C overnight. The next day, cells were topped with PBS and centrifuged at 200 g for 5 minutes. They were were next incubated with a phospho ERK1/2 antibody (Cell Signaling Technology 197G2) for 1 hour at room temperature. Cells were then washed once with PBS and then resuspended into a secondary FITC antibody (Cell Signaling Technology 4412). Cells were washed once with PBS and resuspended into 200 uL PBS per sample for flow cytometry. For optical depolarization studies, the fiber optic cable of a 532 nm laser was placed into the target well in the 96 well plate and turned on for 1 minute prior to adding the TCR stimulation antibodies. The cable was taken out briefly while the antibodies were added and mixed and then put back in for the rest of the stimulation. The laser was held into place using two metal blocks that were aligned over the target

well with hole sizes that fit the laser into the well without risking the end of the fiber touching the cells.

5.5.5 Live/Dead Assay

T cell-NW conjugates were stained with a LIVE/DEAD assay viability kit (ThermoFisher Scientific) for 45 minutes at room temperature. Cells were washed with PBS and centrigued at 100 g for 10 min (slower for nanowire samples) and resuspended into 200 uL/sample PBS for flow cytometry.

5.6 References

1. Steinman L, Merrill JT, Mcinnes IB, Peakman M. Optimization of current and future therapy for autoimmune diseases. *Nature Medicine.* July 2012; 18(7): 59-65.
2. Autoimmune Diseases Research Plan. US Department of Health and Human Services: NIH NIAID. Dec 2002: 03-5140. http://www.niaid.nih.gov/topics/autoimmune/documents/adccreport.pdf
3. Cooper GS, Stroehla BC. The epidemiology of autoimmune diseases. *Autoimmunity Reviews*. May 2003; 2(3): 119-125. PMID: 2783422
4. Lam J, Wulff H. The Lymphocyte Potassium Channels Kv1.3 and KCa3.1 as Targets for Immunosuppression. *Drug Development Research.* November 2011; 72(7): 573-584.
5. Beeton C et al. Selective blockade of T lymphocyte K^+channels ameliorates experimental autoimmune encephalomyelitis, a model for multiple sclerosis. *Proceedings of the National Academy of Sciences of the United States of America.* November 2011; 98(24): 13942-13947
6. Chandy KG et al. K^+ channels as targets for specific immunomodulation. *Trends in Pharmacological Sciences.* May 2004; 25(5): 280-289.
7. Tarcha EJ et al. Safety and pharmacodynamics of dalazatide, a Kv1.3 channel inhibitor, in the treatment of plaque psoriasis: A randomized phase 1b trial. *PLoS One.* July 2017; 12(7): e0180762.
8. Wucherpfennig KW, Gagnon E, Call MJ, Huseby ES, Call ME. Structural biology of the T-cell receptor: insights into receptor assembly, ligand recognition, and initiation of signaling. *Cold Spring Harb. Perspect. Biol.* 2010; 2(4): a005140. PMCID: PMC2845206
9. Huppa JB, Davis MM. T-cell-antigen recognition and the immunological synapse. *Nat. Rev. Immunol.* 2003; 3(12): 973–83. PMID: 14647479
10. Irvine DJ, Purbhoo M a, Krogsgaard M, Davis MM. Direct observation of ligand recognition by T cells. *Nature*. 2002; 419(6909): 845–9. PMID: 12397360
11. Marek N, Mysliwska J, Raczyńska K, Trzonkowski P. Membrane potential of CD4+ T cells is a subset specific feature that depends on the direct cell-to-cell contacts with monocytes. *Human Immunology.* July 2010; 71(7): 666-675.
12. Bezanilla F. How membrane proteins sense voltage. *Nature Reviews Molecular Biology.* April 2008; 9(4): 323-332. PMCID: 18354422
13. Manolios N, Ali M, Bender V. T-cell antigen receptor (TCR) transmembrane peptides: A new paradigm for treatment of autoimmune diseases. *Cell Adhesion and Migration.* April 2010; 4(2): 273-283. PMCID: 2900625
14. Call ME, Wucherpfennig KW. Common themes in the assembly and architecture of activating immune receptors. *Nature Reviews Immunology*. Nov 2007; 7(11): 841-850. PMCID: 17960150
15. Call ME, Wucherpfennig KW. Molecular mechanisms for the assembly of the TCR-CD3 complex. *Molecular Immunology.* April 2004; 40(18): 1295-1305.

16. Boukherroub K, Wojtyk JTC, Wayner DDM, Lockwood DJ. Thermal hydrosilylation of undecylenic acid with porous silicon. *Journal of the Electrochemical Society.* 2002; 14(2) H59-H63.
17. Parameswaran R *et al.*, Photoelectrochemical modulation of neuronal activity with free-standing coaxial silicon nanowires. *Nature Nanotechnology* **13**, 260-266 (2018).

Chapter 6: Discussion and Outlook

Here, we have characterized the photoelectrical properties of coaxial p-type/i-type/n-type silicon nanowires and illustrated three different applications for these nanowires in optically modulating cellular activity. First, we demonstrated that single free-standing PIN-SiNWs can photoelectrochemically depolarize single neuronal cell membranes and elicit action potential in those target cells via a 532 nm fixed laser stimulus. Second, we showed that we can incorporate PIN-SiNWs into a polymeric grid substrate. We used this composite polymer-silicon nanowire hybrid mesh to optically train cardiomyocytes to beat at a target frequency using a scanning laser stimulus. Lastly, we demonstrated that PIN-SiNWs can be functionalized with antibodies to specifically bind to T cells and generate free-standing T cell-nanowire complexes in solution. We then depolarized these T cells using an unfocused 532 nm laser beam and showed a dampening in T cell activation due to nanowire-mediated depolarization. Taken together, our work represents the first studies of nanowire-based photoelectrochemical optical modulation of cellular excitability and activation in a non-invasive, non-genetic manner.

Our characterization of the PIN-SiNW via XPS and APT, as well as novel method of measuring photocurrents from single nanowires, demonstrated the importance of surface atomic gold in the production of photoelectrochemical currents. This atomic gold acts as a catalyst in the material to reduce the kinetic barrier needed for current generation. Thus, we have created a nanoscale photoelectrochemical cell and used it for the modulation of cellular activity. Further work must be conducted to understand the nature of the photoelectrochemical reactions occurring at the PIN-SiNW-electrolyte

interface via both simulations and experiments that can quantify and identify the types of species being generated at the nanowire surfaces. Electron paramagnetic resonance, mass spectrometry, and fluorescent dyes can be utilized to measure the amount and type of reactive oxygen species, for instance, that are produced at the surface of these nanowires in various electrolyte solutions. Moreover, depositing other types of metals (in both nanoparticle and bulk sputtering forms), such as Pt or Cu or bulk Au, onto the PIN-SiNWs can be attempted to understand the influence of specific catalysts on the efficiency of the photocurrent production seen in our system, as well as the production of various photoelectrochemical species in the surrounding solution. Additionally, the use of sputtered gold versus atomic gold, for example, can allow of more efficient photocurrent production due to combined plasmonic, optocapacitive, and photoelectrochemical effects. Other nanowire structures such as axial p-n nanowires, iii, nnn, or ppp nanowires, as well as modulation of nanowire topography via chemical etching and nanoscale lithography can also be studied to understand the influence of the chemical composition of the surface of the nanowire on photoelectrochemical reactions at the nanowire-electrolyte interface.

In our neuromodulation work, we demonstrated use of PIN-SiNWs for cellular excitability modulation in a drug-like fashion. Looking to the future, we hope to take advantage of the fact that silicon can absorb light in the near infrared (NIR) wavelength regime and study photocurrent production using an optical stimulus in that regime. NIR light can penetrate tissue and so *in vivo* applications of these nanowires will be easier to implement with a NIR optical stimulus. Specific *in vivo* applications that are of interest include photo-responsive therapeutics for blindness and peripheral nerve disorders

such as diabetic peripheral neuropathy. These applications can be achieved most effectively via surface functionalization of the nanowires, as demonstrated in the T cell modulation chapter, with neuron type-specific antibodies. Lastly, due to the high spatial resolution of the single nanowire neuromodulation we demonstrated, there is great potential for use of these single nanowires in specific subcellular neuronal structures such as axons or dendrites. This use of our nanowires can allow us to isolate these compartments and structures and understand their specific roles in neuronal functions and transmitting signals within a single cell or to adjacent cells.

In our cardiac training work, we demonstrated training of cardiomyocytes *in vitro* and hearts *ex vivo* using an x/y or z-directional scanning optical stimulus. In using a moving optical stimulus, as well as a high-density mesh of silicon nanowires that exhibit waveguiding behavior, we were able to mimic normal physiological stimuli to groups of cells by providing spatially non-localized signals to various parts of each cell. Future work includes understanding how our composite material could be used *in vivo* for rescynchronization therapies in the context of cardiac rhythm disorders using near infrared light as the optical stimulus. Moreover, modulating the diameter and geometries of the nanowires incorporated into the SU-8-nanowire meshes and simulating waveguiding behavior of these nanowires would be advantageous for optimizing the mesh structure. Additionally, due to the complexity and heterogeneity of the nanowire positioning in the mesh structures that are fabricated via mechanical transfer, machine learning algorithms can be utilized to promote rational material design of an optical mesh structure for optical training. Using machine learning, we would be able to input the NW position at a given pixel (existence of the NW – Boolean and NW angle -

integer), waveguiding parameters for NWs as a function of length and diameter, wavelength of optical stimulus at that pixel, power of optical stimulus, frequency and dwell time of optical stimulus illuminating that pixel, and receive an output of a pixel grid array with various light intensities that each pixel in the array would experience. This network would be able to provide us with an output light intensity array for many meshes that we fabricate. We could then design another network to take the output information from the aforementioned network in addition to positioning of specific cells on the SU-8-NW mesh with respect to each pixel, and output information about which SU-8-NW mesh configuration would be able to optimally train cardiomyocytes to a desired frequency. This approach could also be more generally used for rational material design of nanoscale materials for modulation of cellular activity.

In the previous chapter, we lastly generated free-standing T cell-nanowire complexes and depolarized membranes of populations of T cells using a defocused 532 nm laser. We set out to both provide a novel avenue for cell-specific photo-responsive autoimmune disease therapeutics as well as answer a fundamental question about how membrane voltage modulates T cell activation. We found that T cell activation is abrogated under nanowire mediated depolarizing conditions. Future work includes further optimization of the depolarization methodology used in our work. Generally, further optimization of nanowire mediated photocurrent production efficiency via studies with different metal catalysts, nanowire topography via chemical etchants, and dopants, can reduce the optical power densities necessary for membrane depolarization, allowing for the use of LEDs rather than lasers for optical stimulation. Another possibility includes engineering the flow cytometer instrument itself to provide the laser optical

stimulus for each cell while it is flowing through the cytometer. Our system can additionally be used as a photo-responsive therapy *in vivo* in mouse models of autoimmunity and cancers. The advantages of our system include the fact that the therapeutic can be applied to specific cell types. For instance, we could inhibit effector T cell activity in the context of autoimmunity and inhibit Treg activity in the context of cancer. However, the challenge that remains is directing the optical stimulus to the specific target site. Verifying use of these materials with NIR wavelength light stimuli will greatly improve our current process for these applications.

Furthermore, we hope to use our system to understand how nanowire mediated depolarization can modulate the conformation of the TCR-CD3 complex. FRET experiments studying interactions between the cytoplasmic domain of CD3ε and the cell membrane as well as the extracellular domain of the TCRα chain and the CD3 transmembrane domains during nanowire mediated cellular depolarization in the presence or absence of T cell activation, can elucidate how membrane voltage affects TCR-CD3 conformation. Moreover, expressing the TCR-CD3 complex in *Xenopus laevis* oocytes can allow us to identify gating currents produced by this protein complex upon changes in membrane voltage via cut open oocyte voltage clamp and even identify specific charged transmembrane residues involved in the production of those gating currents via site-directed fluorimetry. Additionally, understanding whether the mechanical presence of a PIN-SiNW complexed with a T cell changes protein localization in an immune synapse with an APC and moreover, whether membrane depolarization alters the positioning of proteins in the immune synapse.

Another related application of our material in the T cell system would be to provide an efficient T cell activation stimulus using ligand patterning via block copolymer lithography. It has been demonstrated that spatial organization of proteins in the immune synapse are very well defined and important for efficient T cell activation. Additionally, researchers have demonstrated in biomaterial-T cell interfaces that stimulatory ligand positioning is crucial for efficiency of T cell triggering. Block copolymers can be deposited on the surface of our nanowires with clearly defined blocks. Each block can be surface functionalized with different antibodies or chemical moieties to provide consistently spaced stimulatory ligands for T cells, allowing for an improved fundamental understanding of axial positioning of surface ligands for T cell triggering.

Taken together, we have demonstrated a novel methodology for cellular activity modulation that has tremendous potential for both fundamental bioelectric studies as well as for photo-responsive clinical therapeutics.